University of Sussex

The Application of the Capacitive Division Technique to Wide-field Time-resolved Fluorescence Microscopy

Lamar Moore

Submitted for the degree of Doctor of Philosophy

University of Sussex

June 2018

Declaration

I, Lamar Alex Moore, hereby declare that this thesis has not been and will not be, submitted in whole or in part to another University for the award of any other degree.

Signature: .....

Acknowledgements

This thesis is dedicated to my parents and step-parent who, with their unwavering love and support, have made my completion of this document possible. They have always believed in me and continued to back my education even after several delays to the completion of this document.

To my partner Martha, thank you for all your encouragement and positive messages during my write-up. Thank you for also allowing me to use your likeness for my simulations. You also provided a comfortable space for me to work on several occasions and I will always be indebted to you for this.

I would like to extend my sincerest gratitude to my research supervisor Dr Philip Birch. His patience, dedication, timely kind words and occasionally stern words made me believe that I could complete this document even when I was plagued with self-doubt. Thank you, Phil. I would also like to thank Dr Roger Philips for his guidance in the areas of life science and jointly Xaiofei Li for the preparation of biological samples used to investigate the effectiveness of the C-DIR device for time-resolved fluorescence measurements.

I am extremely grateful to Photek Limited for providing the opportunity and funding for this PhD, and providing safety training and test equipment for the duration of this study. I would also like to acknowledge my current employers at the Science and Technology Facilities Council of the UK Research and Innovation for allowing me time off on several occasions to finish the write-up of my thesis.

Finally, to all my friends who provided words of encouragement or emotional and recreational outlets, even when you were unaware, I would like to say thanks.

Abstract

Capacitive division and other charge-sharing techniques have become ubiquitous within modern technology. Almost all touchscreen devices depend on some form of charge sharing mechanism. The Capacitive-Division Imaging Readout, C-DIR, scheme developed for space/astronomy applications, is a proven concept which has benefited from widespread publication and several iterations of prototyping. In this study, we borrowed this idea and assessed its application in the field of life sciences, specifically, fluorescence lifetime imaging microscopy (FLIM).

Firstly, the composite C-DIR camera system was developed using a prototype anode developed by Lapington et al in combination with advanced photomultiplier tube technology developed by Photek Limited, and ultra-fast NINO ASIC and high performance time-to-digital converter, HPTDC, readout electronics developed by CERN. Several issues like signal noise, timing jitter and image distortion required special attention to successfully tune the C-DIR system for obtaining FLIM measurements. The C-DIR was characterized in the context of current detector technologies used for time-resolved applications. The maximum achievable global event rate was determined to be a USB 2.0 hard limit of about 1MHz. The spatial resolution and timing performance were identified as 0.5 line-pairs/mm and 200ps FWHM, respectively, which was comparable to other wide-field fluorescence lifetime cameras. These results provided the basis for using the system in a real situation. Before this was possible, however, it was necessary to engineer a bespoke software platform for data acquisition which could cope with the data rates and reduce raw data emerging from the C-DIR system, producing a format compatible with widely used fitting software.

The final stage of the project involved using the C-DIR for real science by reproducing real world experiments which allow for a fitness test of the system in the field. The first experiment involved a calcium calibration where the C-DIR system was calibrated using FLIM on a series of calcium buffers of known concentrations. This C-DIR was able accurately recover the lifetime values from the calcium buffers. The second shorter experiment involved using the calibrated system for the quantification of calcium within living tissue samples using fluorescence lifetime imaging. Results were consistent with those published in the literature which solidified the position of the C-DIR as a viable option for time-resolved fluorescence microscopy.

Keywords: Fluorescence Lifetime Imaging Microscopy-FLIM, FRET, SPIM, time-correlated single-photon counting, photo-multipliers, SiPM, SPAD, charge sharing, capactive division, C-DIR, NINO, HPTDC.

Contents

List of Tables

List of Figures

List of Publications

[1] Lapington, J.S., Leach, S.A., Conneely, T., and Moore, L., *"The capacitive division image readout; a novel imaging device for microchannel plate detectors",* Proc. SPIE Vol. 8859, (2013).

[2] Li, X., Moore, L., Conneely, T., Birch, P. and Phillips, R. (2014) *Calcium-sensitive fluorescent lifetime imaging using wide field time-resolved detection of emission from optical sections excited by light sheet illumination.* In: Microscience Microscope Conference, 30th June -3 July 2014, Manchester.

[3] Birch, P. M., Moore, L., Li, X., Phillips, R., Young, R. and Chatwin, C. (2016) *A wide field fluorescence lifetime imaging system using a light sheet microscope.* Published in: Popp, Jürgen, Tuchin, Valery V, Matthews, Dennis L and Pavone, Francesco S, (eds.) Proceedings of SPIE 2016 on Biophotonics: Photonic Solutions for Better Health Care; Brussels, Belgium; 4th-7th April 2016. 9887 Society of Photo Optical Instrumentation Engineers ISBN 9781510601321

[4] Li, X., Moore, L., Phillips, R., Birch, P. and Connely, T. (2016) *A capacitive division imaging readout detector for light-sheet FLIM.* In: 3rd Light Sheet Fluorescence Microscopy International Conference, 31 Aug - 3 Sep 2016, Sheffield.

[5] Birch, P, Moore, L, Li, X, Phillips, R and Conneely, T (2016) *A wide field time resolved fluorescent lifetime imaging microscope.* In: Photon 16, 5-8 September 2016, Leeds, UK.

[6] Moore, L., Birch, P., Li, X, Phillips, R. and Conneely, T. *Fluorescence lifetime imaging using the capacitive division technique* (in preparation).

List of Acronyms

1-D: One Dimensional

2-D: Two Dimensional

3-D: Three Dimensional

ADC: Analog to Digital Converter

API: Applications Programming Interface

ASIC: Application-Specific Integration Circuit

CCD: Charge-Coupled Device

C-DIR: Capacitive Division Imaging Readout

CFD: Constant-Fraction Discriminator

CMOS: Complimentary Metal-Oxide Semiconductor

CPU: Central Processing Unit

CSV: Comma-Separated Variables

DAC: Digital to Analog Converter

EMCCD: Electron-Multiplying Charge-Coupled Device

EMI: Electromagnetic Interference

FIFO: First-in-First-Out

FLIM: Fluorescence Lifetime Imaging Microscopy

FLI-SPIM: Fluorescence Lifetime Imaging Single Plane Illumination Microscope

FPGA: Field Programmable Gate Array

FRAP: Fluorescence Recovery After Photo-bleaching

FRET: Förster Resonance Energy Transfer

FWHM: Full Width at Half Maximum

GFP: Green Fluorescent Protein

GUI: Graphical User Interface

HPTDC: High-Performance Time-to-Digital Converter

ICCD: Intensified Charge Coupled Device

IPD: Imaging Photon Detector

IRF: Instrument Response Function

MCP: Micro-channel Plate

MHV: Miniature High Voltage

MTF: Modulation Transfer Function

OGB1: Oregon-Green Bapta-1

pbFRET: Photo-bleaching Förster Resonance Energy Transfer

PCA: Principle Component Analysis

PCB: Printed Circuit Board

PMT: Photomultiplier Tube

PSF: Point Spread Function

RFI: Radio Frequency Interference

SHV: Safe Hight Voltage

SiPM: Silicone Photomultiplier

SMA: Sub-Miniature Version A

SMB: Sub-Miniature Version B

SNR: Signal-to-Noise Ratio

SPAD: Single Photon Avalanche Diode

SPIM: Single Plane Illumination Microscope

STL: C++ Standard Library

TAC: Time-to-Analog Converter

TCSPC: Time-Correlated Single-Photon Counting

TDC: Time-to-Digital Converter

TOT: Time Over Threshold

TSS: Transit Time Spread

USB: Universal Serial Bus

WSA: Wedge-and-Strip Anode

XDL: Cross Delay Line

XS: Cross-Strip Anode

1 Background

1.1 Basics of Fluorescence and Time-Resolved Fluorescence

1.1.1 Overview

This chapter provides an introduction into the field of time-resolved fluorescence microscopy. The proceeding section briefly describes the fluorescence phenomenon, why it is important and basic approaches to measuring fluorescence intensity and fluorescence lifetime, including techniques for fitting data. This is followed by focussing on the current trends in technology surrounding the acquisition of time-domain fluorescence data taking an in-depth look at photon-counting detector technologies. This sets the scene for discussing the concept of capacitive division as a new approach to widefield photon-counting, the capacitive-division imaging readout, C-DIR, technology which has been developed by Lapington et al [1] and how this can be adapted to fit into a FLIM context. Finally, the conclusion summarises the aspects of the C-DIR technology which make it a good fit for time-resolved fluorescence microscopy as a motivation for carrying out this study.

1.1.2 Fluorescence

Fluorescence is best described with the use of a Jablonski Diagram Figure 1.1-1. Fluorescence occurs when an electron, in its stable ground state, absorbs a photon of energy hv_A. The electron is then elevated from its ground state S_0 to a more unstable, excited singlet state denoted by S_2. In this state the electron may lose energy through some non-radiative pathways and fall into a lower, yet still unstable, state denoted by S_1. Due to the unstable nature of the S_1 state and the strong pairing with the ground state, the electron randomly returns to the ground state by emitting a

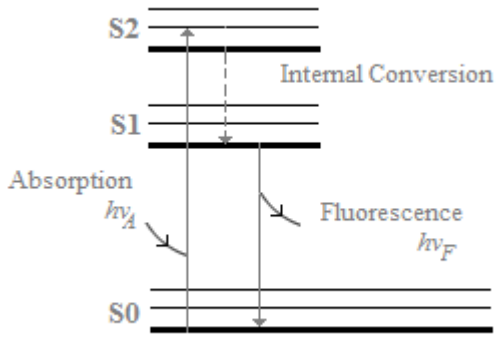

Figure 1.1-1 Jablonski Diagram which shows how fluorescence occurs. An electron in the ground state $S0$, absorbs a photon of energy hv_A and ascends to a higher energy state $S2$. Energy lost, in other non-radiative pathways, causes the fluorophore to descend to a lower energy state $S1$. The electron then randomly returns to the ground state by emitting a photon of energy with a different wavelength from the absorbed energy hv_F.

photon of energy hv_F [2]. This emitted photon of energy represents fluorescence and is of a different wavelength than the excitation energy. Energy differences make the excitation and emitted photons distinguishable for measurement purposes. This phenomenon typically occurs over very short time-scales and usually lasts on the order of nanoseconds between excitation and emission [2]. The typical set-up for observing fluorescence is shown in Figure 1.1-2. Typically, a microscope system

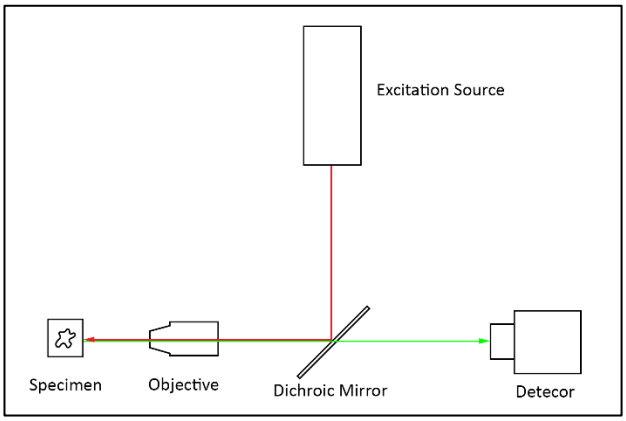

Figure 1.1-2 Basic Fluorescence Microscope Setup. The excitation source emits photons at the absorption wavelength of the sample, shown in red, which is reflected by a dichroic and directed onto the sample by an objective lens. The green ray shows the emitted radiation which passes through the dichroic for detection.

consists of an excitation source, usually a laser which emits at a wavelength matching the absorption profile of the sample, a dichroic mirror which separates the

excitation radiation from the emitted radiation for detection purposes, an objective for focusing radiation onto the sample, and some form of detection system for observing the fluorescence. In this set-up, the fluorescence intensity can be directly imaged using a conventional camera system where the signal is bright enough. This type of fluorescence is referred to as steady-state fluorescence imaging as there is no investigation of the time over which the fluorescence occurs [2].

1.1.3 Fluorescence Lifetime

The intensity of a fluorescence signal, i.e. the number of emitted photon produces within a fixed period, is not the only interesting feature of fluorescence. Knowledge of the exact time over which a single electron is excited and returns to the ground state could also reveal some interesting characteristics about a sample. Fluorescence can be expressed mathematically as an exponential decay shown below:

$$\boldsymbol{I(t) = I_0 e^{-t/\tau}} \qquad \textbf{1.1-1}$$

where $I(t)$ is the fluorescence intensity as a function of time t, I_0 is the initial intensity and τ is the fluorescence decay constant also known as the fluorescence lifetime.

1.1.4 Fluorescence Intensity Imaging

Fluorescence intensity imaging, also referred to as steady state fluorescence, involves the collection and display of two-dimensional histograms of the photons emitted when excited electrons return to the ground state within a sample. Each pixel value stores the number of photons collected in that area of a sample. Photon events are typically measured using photo-sensitive, charge accumulating devices like CCD, Charge Couple Device, or CMOS, Complementary Metal-Oxide Semiconductor cameras [3]. These sensors store these events as accumulated

charges/voltages where the magnitude of the charge is directly related to the intensity of the emitted radiation. These systems are suitable for bright field fluorescence, where fluorophores emit many photons in response to the excitation source but offer very poor signal to noise characteristics for low light level emissions, fewer than 100 photons per shortest integration period, as they are unable to distinguish individual photons from the noise floor of the sensor. Single-photon sensitive detectors like photomultiplier tubes, PMTs, or electron multiplying CCDs, EMCCDs, are sensitive to samples which emit very small amounts of photons, on the order of tens or hundreds of photons per excitation cycle and offer a good solution for imaging in these low light level conditions. Both regimes can produce image acquisition rates at or above video rate, 25Hz. Steady state fluorescence imaging techniques like FRAP [4] [5], Fluorescence Recovery After Photo-bleaching, FRET [6], Förster Resonance Energy Transfer and pbFRET [7], photo-bleaching FRET, have been useful for making intra-cellular proximity measurements, quantifying molecular interactions, tracking processes at the molecular level and even observing/examining cellular structure with molecular resolution.

In the basic fluorescence setup displayed in Figure 1.1-2, the entire sample is illuminated with the excitation radiation and all the emitted light is then collected by the detector. In many cases, only a small section of the sample is interesting. One of the major drawbacks of wide-field fluorescence imaging is the stray light which arises from fluorescence of all areas of the sample and reduces the contrast of an image within the focal plane of interest. Optical sectioning techniques have been developed which allow focusing at a single point in the sample such as confocal microscopy [8] and multi-photon [9] [10] fluorescence microscopy, or thin planes

of excitation light through the sample, light sheet microscopy [11]. These optical sectioning methods enhance image contrast by completely rejecting light outside of the focal plane under investigation. Experiments conducted as a part of this study made use of light sheet microscopy as an approach to optical sectioning. Light sheet microscopy, also known as selective-plane illumination microscopy, SPIM [12], is a wide-field optical sectioning technique achieved by illuminating a sample with a thin sheet of excitation light. Weber et al detail the procedure and various optical arrangements to produce thin light sheets [13]. Detection of fluorescence then occurs orthogonal to the excitation axis. This results in the excitation of only a thin section of the sample thus reducing the effects of scattering from other parts of the sample. This technique has also been shown to result in minimal phototoxicity and photobleaching since only narrow sections of the sample are illuminated at any one time [12] [13]. Either the sample or the sheet can be scanned to image different sections within the sample [13]. These sections can then be recombined using tomographic reconstruction to produce 3D visualizations of the sample. The principle of SPIM is illustrated in Figure 1.1-3. The Open-SPIM project [14] by Pitrone et al represents an open-source hardware and software standard for bringing SPIM to the masses. The standard describes a detailed template for building a SPIM microscope and was the basis for the microscopy used in this study. Light sheet microscopy has been demonstrated for the in-vivo imaging and 3D reconstruction of entire organisms and organ systems even at cellular resolution [15] [16].

Fluorescence imaging has benefited from several years of research and improvements to the techniques and technologies surrounding the field. The importance of fluorescence imaging can be seen in its wide range of applications including the diagnosis of skin conditions like common nevi [17] and malignant

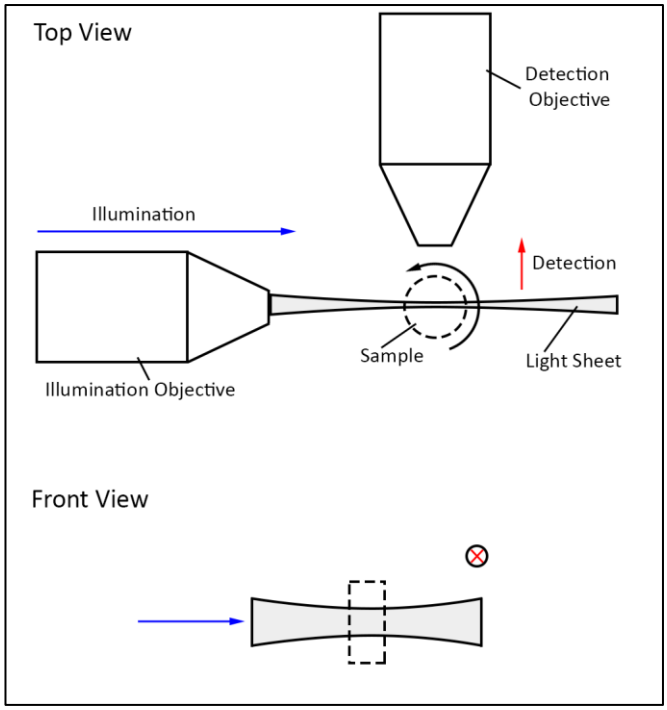

Figure 1.1-3 Principle of selective plane illumination microscopy. A thin light sheet produced by the illumination objective, excites a thin section of the sample. Detection is orthogonal to the illumination axis. The sample can be rotated in the light sheet to obtain 3-D with tomographic reconstruction.

melanoma [18], and investigation of topical drug delivery [19]. Cancer research has also benefited greatly from advances in fluorescence microscopy, particularly in tracking the behaviour and progression of cancer cells [20] [21].

1.1.5 Time-Resolved Fluorescence

Time-resolved fluorescence microscopy is concerned with the characteristics of the decay between excitation and emission. The fluorescence lifetime, τ, shown in equation 1.1-1 is now the interesting feature. Basic half-life mathematical analysis, $\tau = -t_{\frac{1}{2}}/\ln(2)$, shows that the fluorescence lifetime is independent of the initial intensity and is therefore more robust in providing information about the fluorescence under investigation. Fluorescence lifetime measurements offer many distinct advantages over conventional intensity imaging. Lifetimes contain a wealth

of information about the environment, orientation, energy content and conformation of proteins and other macromolecules [2]. Lifetime decays are sensitive to the pH, oxygen concentration, polarity and cation concentration [22] within cells. Two fluorophores emitting photons with the same wavelength could potentially be indistinguishable in a steady state intensity measurement. However, the decay constants of the two species could be vastly dissimilar thus revealing more information about the biochemical environment under investigation [2]. Therefore an abundance of information stored within the temporal content of the fluorescence lifetime might be lost when making steady state measurements alone [2] [22]. Fluorescence lifetime measurements can be obtained in either the time domain or the frequency domain. This study utilizes a very common time-domain technique known as time-correlated single-photon counting, TCSPC [23] [24] [25]. Figure 1.1-4 illustrates the basic idea behind this technique. In TCSPC, every photon emitted from the sample is counted and its arrival time recorded relative to some initial clock pulse, usually from a pulsed laser source [23] [25] [26]. The photon arrival times are added to time bins within a histogram which has a maximum time corresponding to the duration of the sample period. Over time, the histogram will represent the actual fluorescence decay of the sample, Figure 1.1-4.

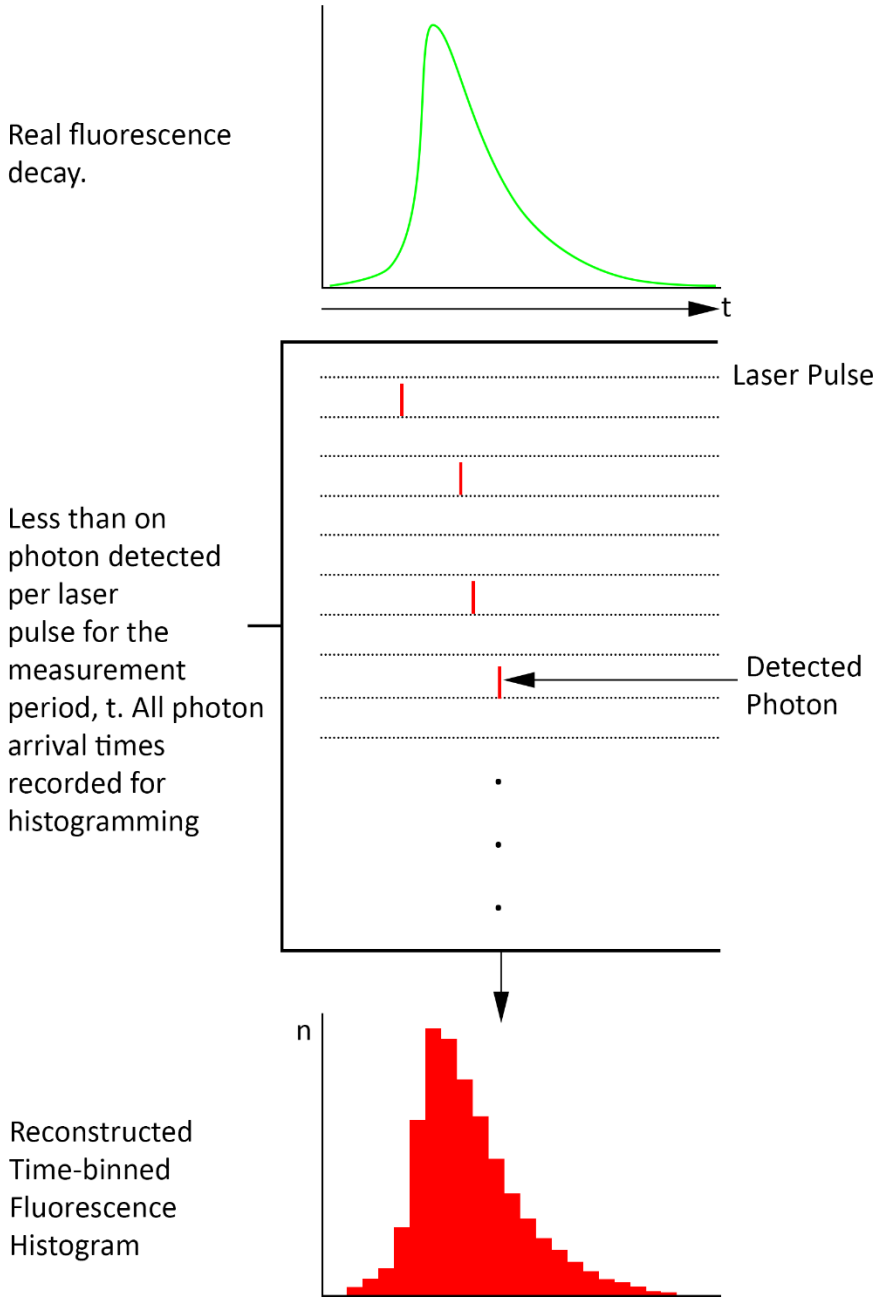

Figure 1.1-4 An illustration of Time Correlated Single Photon Counting. The arrival time of each detected photon is recorded in a histogram of fixed time bins over the measurement period, t. This produces a histogram of the arrival time distribution which represents the fluorescence decay of the sample.

1.2 Measuring Fluorescence Lifetime

1.2.1 Basics of Photon Detection

The first stage in time-resolved fluorescence measurements is the ability to record the arrival time of a photon with high accuracy. PMTs are standard devices used for single-photon measurements due to their sensitivity, low noise, and high timing accuracy, particularly with microchannel plate, MCP, photomultipliers [2]. The structure of an MCP-PMT [27] is shown in Figure 1.2-1. A photon incident on

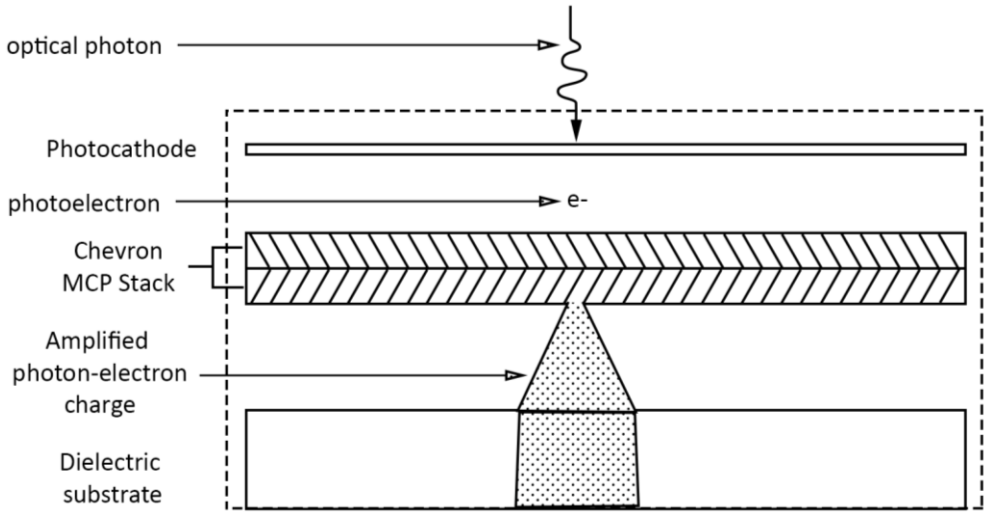

Figure 1.2-1 Basic Structure of an MCP PMT used in this project. Photons enter the input window of and are converted into photoelectrons by the photocathode. A large potential difference across the photocathode and MCP stack accelerate the photons toward the stack which multiply, by 10^6 in many implementations, the photoelectron due to the secondary electron emissive nature of the stack. This produces a cloud of photoelectrons in this multiplicative (or gain) phase. These photoelectrons, accelerated towards the anode from the MCP stack, produce a detectable electric signal which either interacts with a phosphor to produce an image or sensed using analog-to-digital readout electronics.

the photocathode results in the release of a photo-electron by the photoelectric effect. Large biased voltages between the photo-cathode and the MCP stack accelerate the electron towards the secondary-electron emissive MCPs which act as a gain stage for electron multiplication [28]. This generates an electron cloud emerging from the MCP stack which is accelerated towards the rear anode of the tube. The variation of MCP-PMT used as a part of this study is referred to as the

resistive sea PMT [29] which contains a rear anode composed of a di-electric substrate. This allows charge to be localised in the substrate. Capacitive coupling with an external read-out anode is possible therefore allowing the use of anodes which need not be manufactured into the vacuum.

Another approach to single-photon detection involves the use of solid-state technology known as single-photon avalanche diodes, SPADs, or silicon photomultipliers, SiPMs [30] [31]. These devices consist of reverse-biased, photosensitive p-n junction diodes operated above the breakdown voltage [32]. An avalanche current is triggered when a photon interacts with the diode producing a measurable current signal.

1.2.2 TCSPC Architecture

Figure 1.2-2 illustrates the basic setup for time-correlated single-photon counting. The pulsed laser source provides excitation for some fluorescent sample. A photon emitted by the sample is picked up by the PMT. In this setup, the pulsed laser

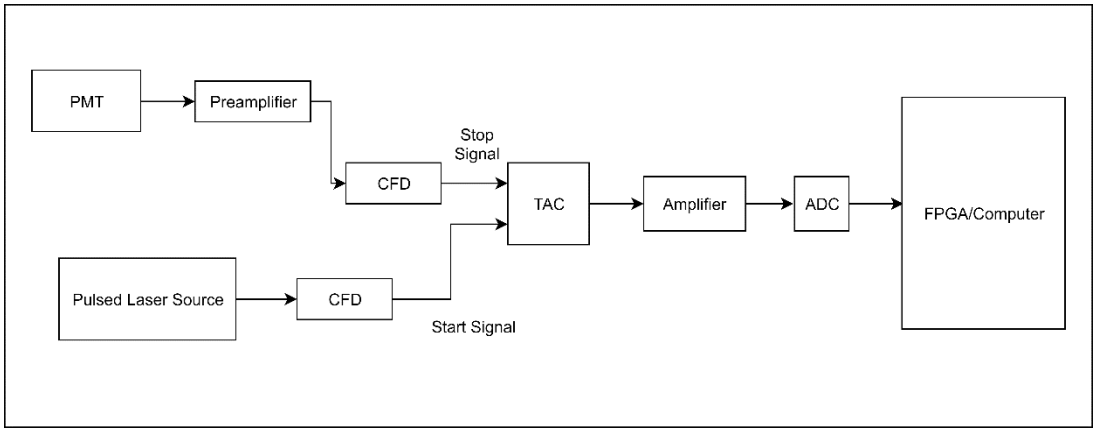

Figure 1.2-2 Basic set-up for TCSPC. The output signal of the pulsed source acts as the start time signal for a TAC. The PMT signal acts as the stop signal. The TAC produces a signal whose magnitude is proportional to the duration between the start and stop signals which is the time interval between excitation and emission. This signal is amplified, fed through an ADC and is ultimately stored in a time channel in FPGA/computer memory. Building up a histogram in these time channels reproduces the fluorescence decay.

output acts as the start signal for a time-to-amplitude converter, TAC, and the PMT signal, which corresponds to the detected photon, acts as the stop signal. The TAC works by charging a capacitor when the start signal is high and stopping when low, the stored charge is proportional to the time interval between the laser pulse and the detected photon arrival. Constant-fraction discriminators, CFDs, are used to reduce noise on the outputs of both the PMT and pulsed source [23]. The TAC output signal is amplified and then digitised by an analog-to-digital converter, ADC, whose output corresponds to the arrival time of the photon.

TCSPC can also be achieved using the setup shown in Figure 1.2-3.

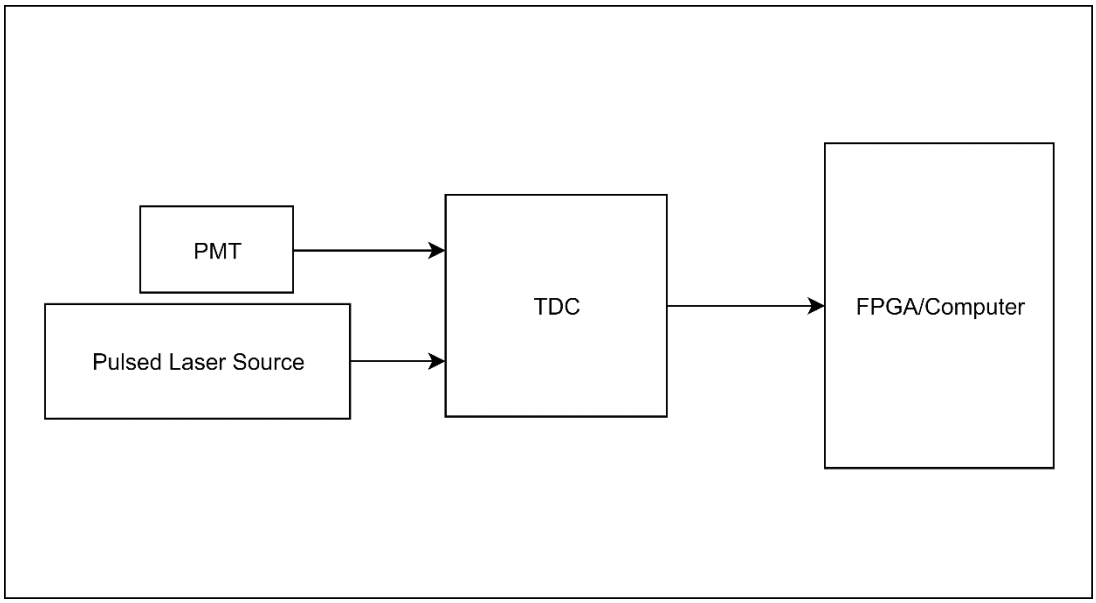

Figure 1.2-3 TCSPC setup using a TDC which consolidates the functionality of the TAC and ADC shown in Figure 1.2-2.

The action of the TAC and ADC combination is replaced with a time-to-digital converter, TDC. The TDC records the time interval between the excitation and emission with high precision, typically on the order of nanoseconds [33]. Instead of using the TAC mechanism of converting time to an amplitude signal, however, timings are measured with respect to the TDC clock as shown in Figure 1.2-4.

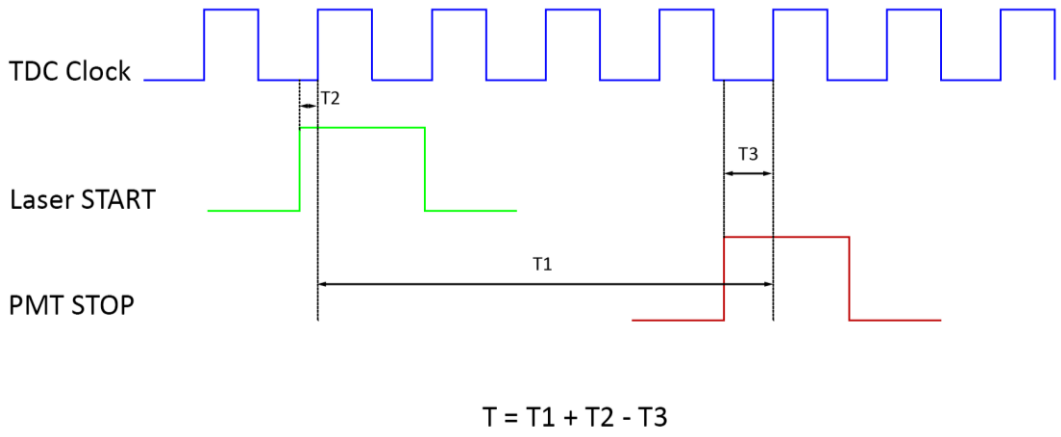

Figure 1.2-4 TDC timing is internally calculated with respect to the TDC clock as shown above. The TDC clock is continuously triggering the device, the excition pulse from the laser acts as the START of a timing measurement and the emission pulse from the PMT signals the end of a timing measurement.

The continuously running TDC clock acts as a reference for all timing measurements. The arrival of an excitation pulse signals the start of a timing measurement by setting START high. The PMT emission pulse sets STOP high thus signalling the end of a measurement. The time interval between the rising edge of the excitation pulse and the following TDC clock rising edge is recorded as T2. Similarly, the interval between the rising edge of the PMT pulse and the TDC rising edge which follows is recorded as T3. Finally, the time difference between the two recorded TDC clock rising edges is recorded T1. The time, T, between excitation and emission is then calculated as $T = T1 + T2 - T3$ [33]. The digitised arrival time is output to a memory register either on an FPGA or a computer and stored in a histogram of the arrival time of each emitting photon with respect to the laser pulse. The general rule of thumb for TCSPC is to attenuate the laser signal such that the probability of detecting a photon per excitation cycle is low. The idea is that the detection rate should be 1% the laser pulse rate. This ensures there are no ‘pile-up’ effects [23]. There are two main mechanisms for pile-up which distort TCSPC measurements. Classic pile-up occurs where several photons are detected per laser

signal period. Higher rep rate sources have reduced this problem since, at even 1% of the excitation frequency, the detection rates can be in the MHz region [2] [23]. Inter-pulse pile-up occurs where the probability of detection of a photon within a sync period is decreased due to the overlapping dead-time of electronics within this period [23]. Pile up will be discussed in more detail in 1.5.8.

1.2.3 Extracting Fluorescence Lifetime

The next logical stage after successfully collecting the fluorescence lifetime data using TCSPC is to use a model, like that presented in 1.1, which fits the data to recover the lifetime τ. In practice however, a model this simple is seldom used. Many samples exhibit two or more exponential components, for example, OGB-1 produces a bi-exponential decay due to the presence of bound and free Ca^{2+} [2] [34]. Additionally, simply fitting exponential decays in many instances is not sufficient. The fluorescence signal is usually a convolution of the impulse response of the measurement system and the fluorescence decay from the sample. Therefore, our simple model in equation 1.1-1 becomes far more complex as shown below:

$$\boldsymbol{I = IRF * \left(Z + \sum_{i=0}^{n} I_i e^{-t/\tau_i}\right)} \qquad \textbf{1.2-1}$$

where IRF is the instrument response function or impulse response, Z is a function or constant which represents the background, n is the number of exponentials required for the fit, I_i represents the initial fluorescence amplitude for each decay component and τ_i is the fluorescence lifetime component. This is a far more all-encompassing model. Section 2.6.1 provides more detail on how this model could be applied on a dataset.

TCSPC data is collected by building up histograms of binned photon counts, as such, these experiments typically make use of Poisson, or counting, statistics [2].

This allows for a simple approximation of the error in the data as the square root of the photon counts for each time bin, i.e. $\sigma_m = \sqrt{N_m}$ where σ_m is the standard deviation, error, of the measured time and $N_m$is the number of counts collected in that time bin. This relationship therefore shows that as the number of photons increases, the relative uncertainty in the data decreases [2]. However, the main assumption here is that there are no sources of systematic error in the data.

Once an appropriate model for the data has been selected and systematic errors have been reduced or eliminated, it is time to use some type of fitting software to recover the fluorescence lifetime(s) from the data. For TCSPC data, it is typical to make use of the Levenberg-Marquardt algorithm [2]. The reduced chi-square, X_v^2, is used as a measure of the goodness-of-fit. X_v^2 is described as:

$$\boldsymbol{\chi_v^2 = \sum_{i=0}^{N} \frac{\left(y_i - f(x_i)\right)^2}{\sigma_i^2}} \qquad \textbf{1.2-2}$$

where N is the number of observations, y_i is the observation, $f(x_i)$ is the expected value which is represented by our model in equation 1.2-1 and σ_i is the variance, or error, in our measurement. The general rule of thumb is that $\chi_v^2 \simeq 1$ means there is good agreement between the data and the selected model. $\chi_v^2 > 1$ suggests that the error has been under-estimated. Most fitting software display both the resulting χ_v^2 along with a plot of the residuals $y_i - f(x_i)$ which assist in the determination of whether the model should be accepted. Analyses of this kind require high statistics on the order of 1K photons for a single exponential and >>1K photons for multiple exponential components [23] [35] [26].

1.3 Time-Resolved Fluorescence in 2-Dimensions

1.3.1 Fluorescence Lifetime Imaging Microscopy

So far, the idea of measuring fluorescence lifetime in a single dimension has been discussed. The use of standard photomultiplier tubes, or SPAD detectors allows quantitative detection of fluorescence but loses the spatial information allowed by intensity measurements using CCD/CMOS camera systems. Extending the measurement of fluorescence lifetime in 2D using TCSPC has been demonstrated using a range of techniques including laser scanning [36] [37], single-photon CMOS/SPAD arrays [38] [39] and position sensitive read-out anodes for photomultipliers [40] [41] [42] [35]. These approaches have led to high contrast images based on fluorescence lifetime an example of which is shown in

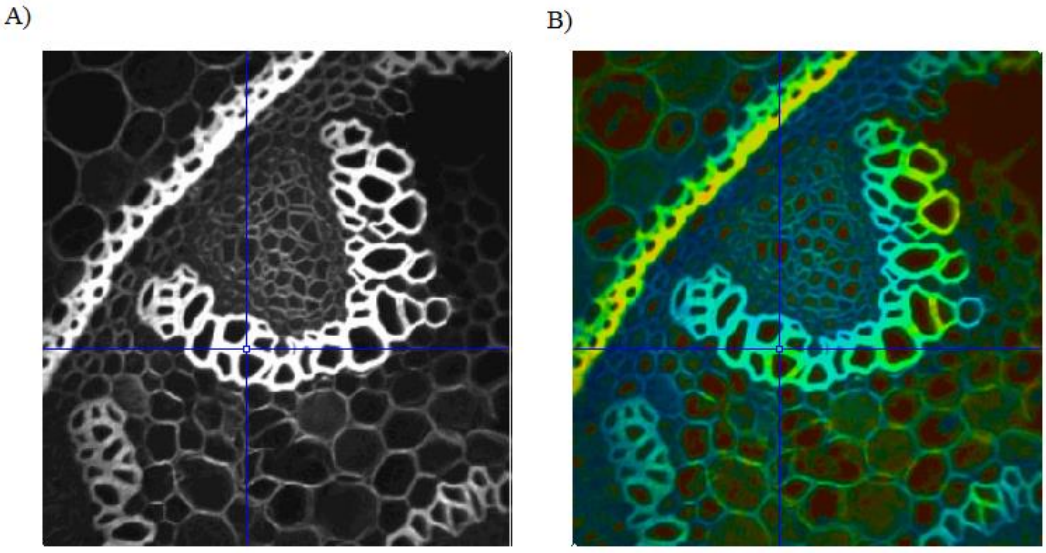

Figure 1.3-1 Becker and Hickl SPCImage image collected from convallaria sample showing A) Intensity and B) High contrast fluorescence lifetime images [23]

Figure 1.3-1. It is easy to see there is more contrast information provided in image B), due to the variation in fluorescence lifetime, than the intensity measurement alone in A). This additional contrast can provide information on the biochemical

environment of a sample in addition to structural information. Fluorescence lifetime imaging microscopy, FLIM, has been beneficial in providing further insights into cell metabolism [43] and biochemistry [44], protein/DNA kinetics [45] and a host of other fields within and outside of the life sciences.

1.3.2 Important Considerations

Section 1.1 briefly alluded to count rates as an important characteristic for time-resolved fluorescence. 1.2 described the basic idea behind taking time-resolved measurements and some of the requirements for fitting. Any system used for FLIM must satisfy a few basic requirements to provide useful, accurate results. In the context of TCSPC, systems must provide large enough counts, per area of interest, to allow accurate fitting and recovery of the fluorescence lifetime mentioned at the end of 1.2.3. Acquisition times for these photons can be limited by the dead-time of read-out electronics, quantum efficiency of the detection system and the emission signal intensity from the sample. In the scanning case, dwell times can be exceedingly long, in some cases on the order of minutes, for weakly emitting samples. This raises issues of photo-bleaching and photo-toxicity for live samples since they are subjected to high levels of radiation over long periods. Specific techniques like two-photon microscopy [46] in combination with improvements in microscope technology [47] have realised video rate fluorescence lifetime imaging whilst reducing photodamage and photobleaching. However, these scanning systems tend to be highly complex and expensive. Wide-field approaches typically use a time-gated mechanism [48], with an intensified camera, for measuring the decay with respect to the excitation pulse. Solid-state approaches like that presented by Li et al [49] allow video-rate FLIM however do not provide resolutions above 32x32 pixels.

The ideal FLIM system would maximise both position resolution and timing performance. The H33D detector developed by Michalet et al [35] manages to deliver a fast, high spatial resolution system for FLIM. This makes use of a photomultiplier based architecture with a cross-delay line, XDL [42] [50], position sensitive anode and fast timing electronics. The data acquisition employs position sensitive TCSPC to build up a 2-D histogram of photon arrival times without the need for scanning. This device will be discussed in more detail in section 1.5.

Frequency domain measurements are obtained using a phase-modulation method [22] [51]. A sinusoidally modulated light source is used to excite the sample; due to the lifetime of the sample excitation, the emitted energy, although modulated at the same frequency as the source, is delayed (phase shifted) and demodulated with respect to the excitation energy [51] [26]. The phase shift and demodulation encodes the lifetime of the sample [22] [26]. These measurements do not require the use of photon counting equipment since data is not collected on an event by event basis. Although frequency domain FLIM can result in frame acquisition rates of around 29Hz [51], frequency-domain FLIM is less intuitive and therefore less widely used than time-domain FLIM.

1.3.3 Quantitatively Describing FLIM Systems

In the previous section it was mentioned that spatial resolution and timing performance are two major considerations in the design of microscope and detector systems for FLIM. The question which may be lurking in the reader's mind is, how is this all quantified?

The spatial resolution of a detector in this context refers to a measure of the sharpness of the image produced by the device which goes beyond just the sensor

pixel count, which on its own is a potentially meaningless value [3]. Basic spatial resolution measurements are taken using a standardized resolution mask, for example the US Air Force Resolution Chart shown in Figure 1.3-2. The spatial resolution is then given in line pairs per millimetre, lppm, which describes the

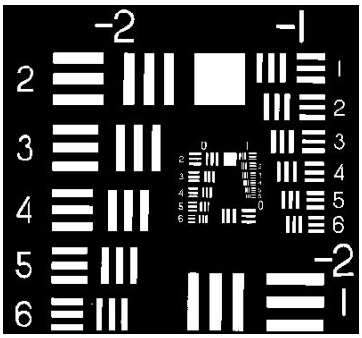

Figure 1.3-2 USAF Resolution Chart. This chart produces a "by-eye" estimate of the resolving power of an imaging system. The chart is usually read groups at a time, for example, group -2 has elements 1-6. The smallest resolvable group determines the limiting resolution of the system in line-pairs-per-millimetre.

number of resolvable line pairs in one millimetre of an image [52]. One line pair comprises one solid black line and one solid white line of the same width. A second simple measurement is the point spread function of the detector, i.e. how the detector responds to a point source [35]. Figure 1.3-3 graphically illustrates the point spread function (PSF) in the centre of the image. This resolution is stated in μm full width at half maximum (FWHM) of the PSF [35] [41] [42] [53]. The true physical measure of sensor resolution is the Modulation Transfer Function, MTF [3] [54]. This can be obtained by taking the magnitude of the Fourier transform of the PSF in two dimensions. [54].

The temporal resolution of a detector system is determined by the transit time spread (TTS) and/or the instrument response function (IRF) [23]. The TTS

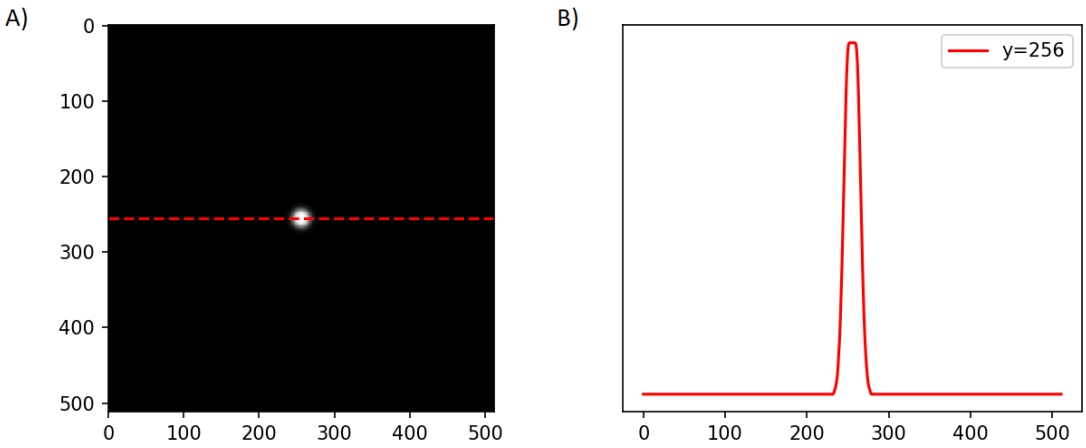

Figure 1.3-3 A) Image of sensor illuminated with point source of infinitesimally small width. B) Corresponding point spread function in x direction of intensity against position based on the line profile in A which is located at y=256. The full width at half maximum of this PSF is a measure of the resolving power of the imaging system.

describes the variation in the timing between absorption of a photon at the photocathode and the measured output pulse [2] [23]. This property is the limiting timing resolution of the detector for TCSPC [23]. The IRF can be described as the pulse shape measured by a FLIM system for an infinitely short lifetime [23]. In practical situations, the width of the IRF (FWHM) gives you the limitation on the timing performance of the entire system, microscope optics included, as opposed to the TTS which describes the detector alone. In a FLIM setup, the IRF can be measured using a dye sample with a very short lifetime which are shorter than or comparable to the TTS of the system [35].

An ideal FLIM system would combine high spatial and temporal resolution, high photon efficiency, and would support large count rates [23] [55]. Essentially, a wide-field, imaging, photon-counting detector is required [55]. From the material presented in the preceding paragraphs, this detector would have both a narrow PSF

and TTS. The remainder of this section will present the advances in micro-channel plate imaging anode technology and the resolution achieved by these detectors.

1.4 Current Position-Sensitive Anode Readout Schemes

The focus of this study was on the development of a photomultiplier-based technology for the FLIM which made use of a position-sensitive readout anode. Therefore, it is important to understand the current approaches to position-sensitive anodes in this context. Their strengths and limitations and how they compare to the proposed system under consideration.

1.4.1 Resistive Anode

The resistive anode [56] has been commercialized as part of the IPD (Imaging Photon Detector) Camera manufactured by Photek Ltd [57] [58] [59]. The anode consists of a shaped resistive sheet with four corner electrodes which collect charge incident on the anode Figure 1.4-1 [58]. The anode signals are pre-amplified to improve SNR and are then passed on to a pulse-shaping filter before digitization in an analog-to-digital converter (ADC) [59]. The position encoding is achieved by using a simple position centroiding algorithm based on the magnitudes of the charge collected at each anode as shown in below:

$$\boldsymbol{x} = \frac{(\boldsymbol{Q_A}+\boldsymbol{Q_B})-(\boldsymbol{Q_C}-\boldsymbol{Q_D})}{\boldsymbol{Q_A}+\boldsymbol{Q_B}+\boldsymbol{Q_C}+\boldsymbol{Q_D}} \quad \textbf{1.4-1}$$

$$\boldsymbol{y} = \frac{(\boldsymbol{Q_A}+\boldsymbol{Q_D})-(\boldsymbol{Q_B}-\boldsymbol{Q_C})}{\boldsymbol{Q_A}+\boldsymbol{Q_B}+\boldsymbol{Q_C}+\boldsymbol{Q_D}} \quad \textbf{1.4-2}$$

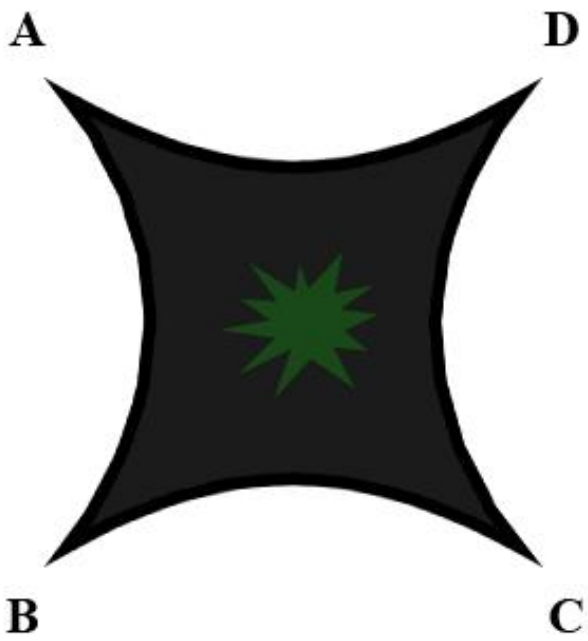

Figure 1.4-1 Shaped resistive sheet anode with 4 read-out nodes labelled A-D with an incident charge.

where Q_i refers to the magnitude of the charge at each of the read-out anodes and (x, y) is the calculated charge centroid. Milnes et al. [59] have reported the resistive anode with its associated read-out electronics can achieve a position resolution better than 30μm FWHM and timing resolution of ~4ns FWHM.

1.4.2 Wedge and Strip Anode

The wedge-and-strip anode (WSA) [60] is an alternative charge dividing imaging anode; unlike the resistive anode which is simply comprised of a resistive sheet, the WSA consists of three or four electrodes arranged as wedges and strips as illustrated in Figure 1.4-2 [60] [61] [62]. Early studies have demonstrated the position resolution of the WSA to be ~50μm FWHM [60]. Lapington et al. have improved on the design of the WSA in the form of the Tetra Wedge Anode (TWA) and have achieved a position resolution of ~15μm FWHM [29].

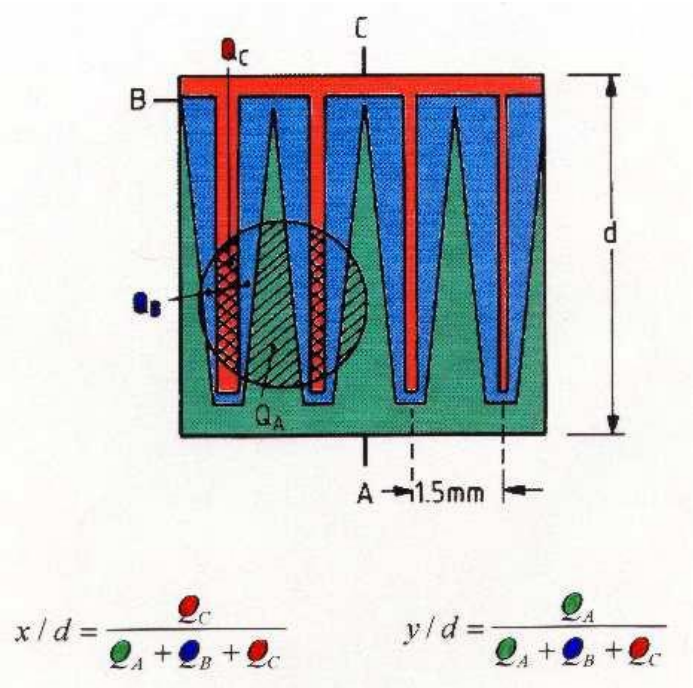

Figure 1.4-2 Operation of the Wedge and Strip Anode [61]

1.4.3 Cross Delay Line Anode

The cross-delay line anode was originally developed for space applications as a part of 12 experiments conducted aboard the SOHO mission platform [50]. The structure and operation of the cross-delay line anode in combination with a photomultiplier is shown in Figure 1.4-3. The anode itself is composed of two overlapping electrical transmission lines which are mounted behind the MCP in the path of an inbound electron cloud inside the sealed PMT [35] [50] [42]. Other designs have been reported with the anode mounted outside of the sealed vacuum tube [41] [63]. These wires are used to determine the X, and Y coordinates of an incoming electron cloud. The absolute photon arrival time relative to the laser pulse is taken from the pulse arrival time at the back MCP plate [35] [41]. The timing of each incoming electrical signal which has been induced in both wires is measured at both ends of each wire. The time taken for the pulse to arrive at the terminals determines its point of origin along the transmission line. This time difference is then used to calculate the X and

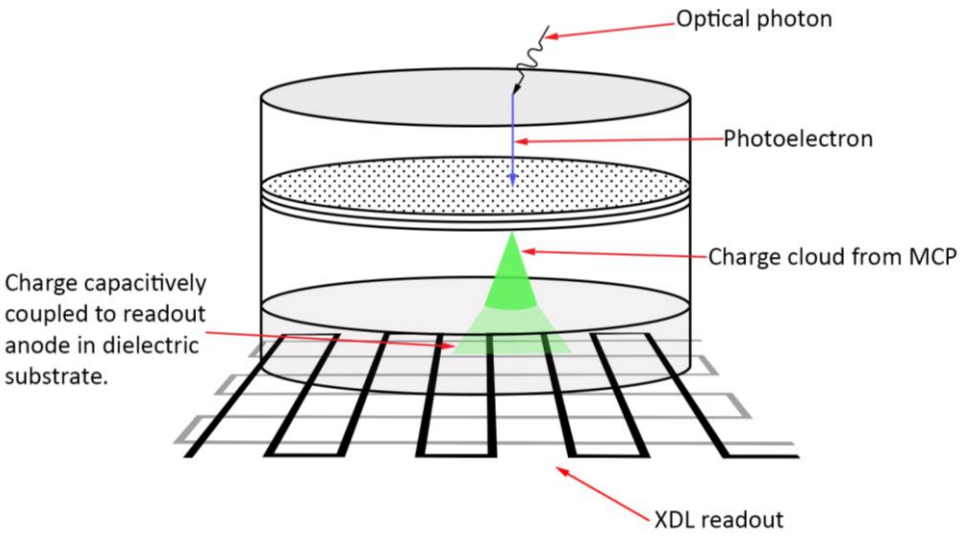

Figure 1.4-3 Cross delay line anode coupled with a PMT for position sensitive read-out.

Y positions of the incident photon [35]. The read out electronics for the delay line consist of fast amplifiers and constant-fraction discriminators (CFDs) coupled to Time-to-digital Converters (TDCs) for fast sub nanosecond read-out [41] [50] [42]. Benchmark tests conducted by Michalet et al. rate the detector with timing resolution of 100ps FWHM TTS and spatial resolution of 100µm FWHM with a detector gain of $9x10^6$ supporting local count rates 2-10KHz [35]. Jagutzki et al. reported position resolution of ~87µm FWHM with the external XDL anode coupled to a resistive screen PMT [41].

The XDL anode has been demonstrated as a useful device for fast acquisition of multi-dimensional FLIM data [55]. Colyer et al. employed the XDL anode in their H33D Gen I prototype and using phasor analysis with phasor ratio imaging as described above, were able to obtain FLIM map images with integration times as short as 10ms [55] [35].

1.4.4 Cross Strip Anode

The cross strip (XS) anode is similar in design to the XDL anode discussed above [53] [64]. The electrode is made up of orthogonally placed electrode strips as illustrated in Figure 1.4-4. The electrode pitch is coarse (~0.5mm) and charge is directly sensed and read out from each individual electrode [53] [65] [64]. Figure 1.4-5 demonstrates the operation and structure of the XS anode. The electronic read-out configuration for the XS anode is far more complex than the XDL anode described in the previous section. Each electrode contains local

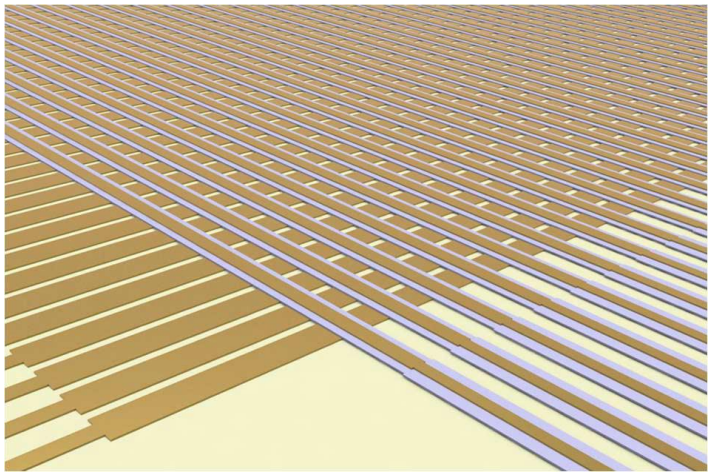

Figure 1.4-4 Structure of the CS anode [66]

preamplifiers at either terminal, these act to increase the SNR before the signal is amplified [53] [64] [65]. The amplified signals are then digitized in parallel using ADCs and are fed into an FPGA which processes position centroiding and timing [64]. Coarse position encoding for X and Y coordinates is achieved by locating the strips with peak charge output [53]. The centroid of the four highest neighbouring strip signals is then used to locate the electron cloud centre (fine position) [53].

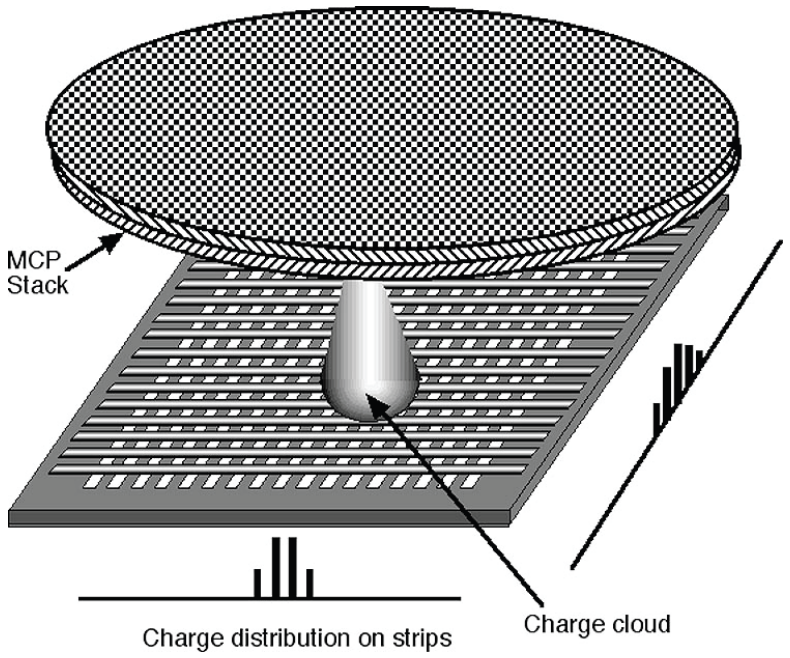

Figure 1.4-5 CS anode operation [65]

Siegmund et al. and Tremsin et al. have demonstrated that the XS anode can achieve ultra-high spatial resolution (<10 microns) even at very low gain [53] [64] [67]. The timing accuracy of the XS anode is similar to that of the XDL anode at ~100ps FWHM [68].

1.4.5 Alternative Read-out Schemes

All of the anodes described thus far employed charge-sharing techniques where event positioning was determined using the ratio of charges collected at several read-out nodes [56] [60] [69] [50] [53]. Another approach to obtaining charge position information would be to pixelate the anode surface itself into discrete read-out pads much like the pixelated sensors of CCDs and CMOS chips. Lapington et al. have demonstrated this with the HiContent [70] and IRPICS [71] detectors which contain an 8x8 and 32x32 array, respectively, of discrete anodes for high-speed, parallelized charge read-out where imaging is a consequence of the pixelated anode design.

Another approach to the segmented anode design is the quadrant anode [72]. This anode is disc-shaped and comprises four electrodes, arranged like equally sized slices of a pie chart, which are electrically insulated from one another [72]. The amount of charge collected at each electrode depends on the position of the incoming charge cloud and can thus be used to generate a charge centroid. This anode represents one of the simplest implementations of multi-anode architectures which have been demonstrated for wide-field TCSPC fluorescence lifetime imaging applications [73] [74] [75].

1.5 Motivation: Capacitive Division Imaging Read-out

1.5.1 Aim

The aim of this research study is to apply the capacitive division technique to time-resolved fluorescence microscopy. The capacitive division anode for photon-counting applications has already been demonstrated by Lapington et al [1]. The detector used in this project comprises three major components: the segmented, charge sharing anode, fast NINO ASIC read-out amplifiers, and 25ps resolution HPTDC. The motivation for using the C-DIR is the promise of high spatial resolution, MCP-limited timing resolution and high global and local count rates [1]. In the class of photomultiplier-based fluorescence cameras, the C-DIR has the potential to outperform the XDL anode and establish itself as a leading system and technique for FLIM. Table 1.5-1 shows how the C-DIR compares with other systems used for time-resolved single-photon applications. The C-DIR promises higher global count-rates than any other photomultiplier-based system. The timing resolution will be MCP-limited and comparable if not better than the cross-delay line based H33D system.

Table 1.5-1 Comparison of the C-DIR with other techniques used for time-resolved photon counting applications.

Technique	Advantages	Clear Disadvantages
Resistive Anode	• High spatial resolution 30µm FWHM.	• Low timing resolution of 4ns FWHM.
Wedge and Strip	• High spatial resolution ~15µm with tetra-wedge.	• No examples in time-resolved experiments.
Cross-Delay Line	• Good spatial resolution ~87µm FWHM. • High timing resolution ~100ps FMHM. • High local and global count-rates 2-10KHz and 500KHz respectively.	• No clear disadvantages beyond the system bulk due to CFD electronics and XDL anode which is complex to manufacture and expensive [41] [42] [35].
CMOS (SPAD)	• Video rate (25fps) FLIM in a 32x16 array achievable [49].	• Low spatial resolution 32x32 physical pixels [49]. • Lower quantum efficiency due to lower active area due to timing electronics combined in pixel active area [49]. • Low global count-rate 100KHz [49].
C-DIR	• High global count-rate 1MHz. • Reasonable spatial resolution ~150 µm FWHM based on prototype results. [1] • MCP-limited timing resolution [1] of ~100ps FWHM [80] • Compact due to the simple NINO interface to C-DIR anode and HPTDC electronics compared to other systems [1].	• Possible susceptibility to noise due to TOT discriminator electronics.

This section will examine the features of the C-DIR technology and concept which justify its use in fluorescence lifetime imaging microscopy.

1.5.2 Principle of Capacitive Division

The capacitive division concept is like the charge sharing techniques described in the previous section. However, instead of actively collecting charge using electrodes and measuring the analogue signal, capacitive division utilizes a planar resistive

anode to passively collect and localize the charge event as illustrated in Figure 1.5-1.

A simple schematic of the anode structure is shown in

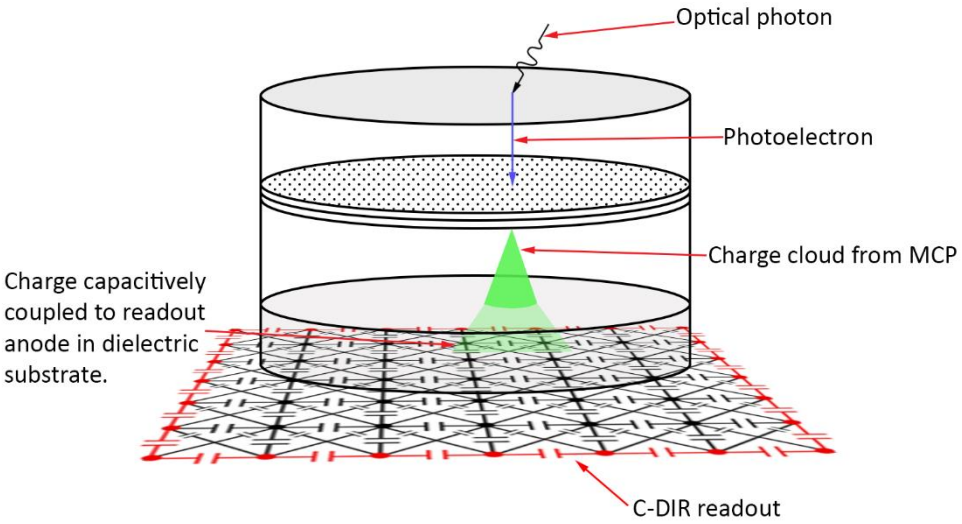

Figure 1.5-1 Operational principle of the capacitive division anode coupled with the a resistive-sea MCP-PMT [1].

Figure 1.5-2. Charge propagates through the anode capacitively towards the corner

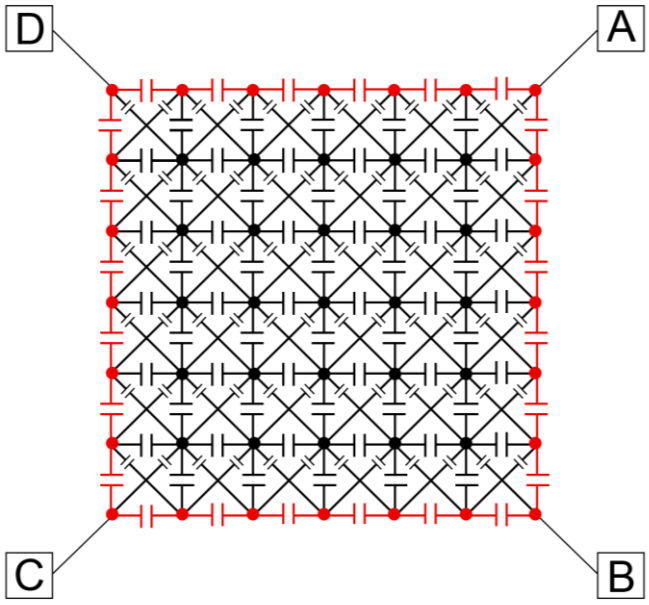

Figure 1.5-2 Schematic of C-DIR anode showing discrete, electrically isolated electrodes (black circles) which are capacitively coupled to their neighbours. The nearest neighbour capacitances on the perimeter (red) are 10-100 times greater than the internal nearest neighbour capacitances [1].

electrodes where the charge is read out. This scheme utilizes a simple algorithm for the calculation of the charge cloud centroid, which is expressed as [1]:

$$\boldsymbol{x = \frac{Q_a+Q_b}{Q_a+Q_b+Q_c+Q_d}} \quad \textbf{1.5-1}$$

$$\boldsymbol{y = \frac{Q_a+Q_d}{Q_a+Q_b+Q_c+Q_d}} \quad \textbf{1.5-2}$$

where Q_i is the magnitude of the charge at each anode and (x, y) is the position of the charge centroid. This algorithm bears a striking resemblance to that utilized for the resistive anode. The sections to follow will detail the respective components which constitute the C-DIR detector; the Resistive-Sea MCP PMT [29], the ultra-fast NINO ASIC [76] and the High Performance TDC [77].

1.5.3 Resistive sea MCP PMT

The front-end sealed photomultiplier tube used in conjunction with the C-DIR detector is the resistive sea MCP PMT which is manufactured commercially by Photek Ltd [29] [1], previously described in 1.2.1. This device utilizes a standard MCP PMT design with a photocathode proximity focused to a pair of chevron stacked MCPs [29]. A charge cloud emerging from the MCP is localized on a planar resistive sheet which induces a signal through a dielectric substrate onto which the sheet is deposited [29]. This localization occurs on the timescale of electronic measurement of the signal [29]. The C-DIR detector employs this technique to capacitively induce a localized signal on the anode surface, which is then spread to the 4 read-out anodes via capacitive charge sharing [1].

1.5.4 NINO ASIC

The NINO ASIC, developed at CERN, is an 8-channel, high speed, front-end amplification/discrimination analogue device which is used as the first stage of

output electronics for directly sensing charge emerging from the C-DIR anode [76] [1] [40].The NINO comprises a preamplifier, pulse shaper and time-over-threshold, ToT, discriminator, with a timing resolution of 10-20ps depending on the input charge and subject to time walk correction [40] [76]. The broad dynamic range of the NINO ASIC ($1.25x10^5$ – $1.25x10^7$electrons) makes it suitable for sensing the output range (Pulse Height Distribution – PHD) of photomultiplier tubes [40]. The charge is measured by exploiting the time walk characteristics of the ToT discriminator, illustrated in Figure 1.5-3, producing an LVDS, Low-Voltage Differential Signalling, signal whose leading and trailing edges correspond to the shaped analogue pulse [40]. These leading and trailing times are then digitized using a HPTDC.

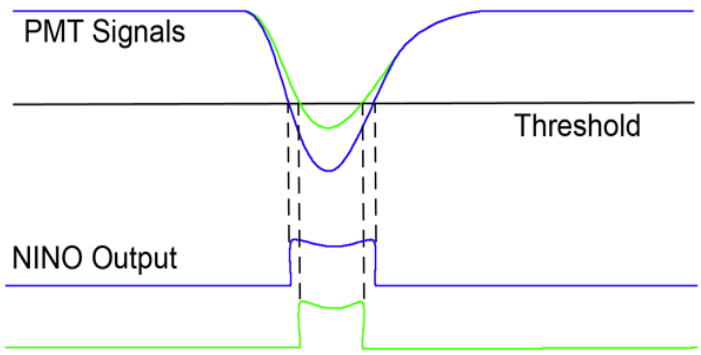

Figure 1.5-3 Time over threshold measurement. As the amplitude of the pulse increases so does the NINO output pulse width. The measured leading-edge of the pulse, and pulse width, vary with input charge amplitude in a phenomenon known as time walk. This is exploited to recover the magnitude of the incident charge.

1.5.5 HPTDC

The high performance general purpose TDC (HPTDC) [77] ASIC is a 32 channel TDC which can be used in a very high resolution mode offering eight channels with 25ps timing precision [77] [40]. The TDC input matches the NINO LVDS output and offers the option of measuring both leading and trailing edge times emerging

from the ToT charge measurement [40]. These time stamps can ultimately be used to recover the magnitude of the detector charge. The TDC is used in triggered mode [77] where the device employs a “trigger window matching” approach which accepts events that have occurred within a predefined offset relative to the trigger input [40]. The timing data is then stored in an FPGA memory buffer as a series of unsigned 32-bit integers with the format outlined in Figure 1.5-4.

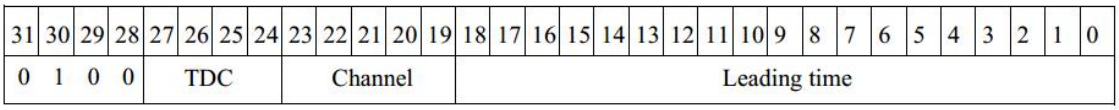

Figure 1.5-4 Structure of 32-bit TDC data packet. The 19 most significant bits store the timing data. The TDC channel is stored in the next 5 bits (19-23). For applications where multiple TDCs are daisy-chained together, bits 24-27 store the unique TDC identifier. Finally, the last 4 bits store the packet identifier.

The TDC buffer can be queried using a software API developed at Photek Ltd to obtain a user defined block, usually a multiple of 512 bytes, of TDC packets via a USB 2.0 interface.

1.5.6 C-DIR Charge Measurement Operation

The charge cloud emerging from the rear MCP plate within the resistive sea PMT capacitively induces a charge on the C-DIR surface via the dielectric substrate. The charge then spreads to neighbouring capacitors until it reaches the four read out anodes. The analogue charge is read by the NINO using the ToT technique which produces a leading edge and trailing edge pulse. These leading and trailing edge pulses are time stamped and digitized by the HPTDC ASIC. Digitized timing values are then read into computer memory via USB, where timing is extracted from the TDC packets. The pulse width is calculated, and charge obtained using a pulse width to charge look up table to obtain the charge incident on each imaging channel. The charge centroid is then calculated using the equations in section 1.5.2.

1.5.7 Calibration and Distortion Correction

The previous section describes a lookup table which must be accessed to recover the charge incident on an imaging channel given the pulse width. This lookup table is generated by calibrating the NINO's response to an input charge. Injecting a known charge into the NINO channels and measuring the resulting pulse width using the HPTDC electronics produces a calibration curve as shown in Figure 1.5-5.

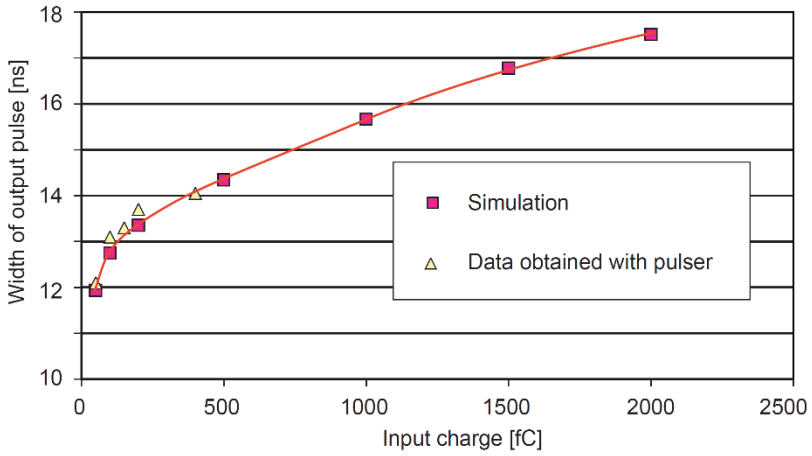

Figure 1.5-5 Example of NINO non-linear response to input charge recorded by Anghinolfi et al. [76].

Interpolation of data points can be used to generate a lookup table to determine charge and hence calculate the centroid of the charge incident on the detector surface.

One of the major sources of noise, or distortion to timing data, when measuring photon arrival times using the ToT technique, is time walk [40]. This phenomenon is illustrated in Figure 1.5-3 where variations in the magnitude of the analog charge pulse results in a shift in the measurement of the arrival time due to the fixed threshold [40]. This variation clearly affects the accuracy of the timing measurement. Time walk correction must be employed to fully exploit the benefits of very high timing resolution with the NINO/HPTDC combination.

The C-DIR anode may produce spatial distortions because of the non-linear response of the anode to incident charge footprints at different locations on the anode surface [78]. This non-linearity could result in barrel and/or pin cushion image distortion as demonstrated by Conneely [78] in simulations of the anode surface response. These distortions must be corrected for the C-DIR detector to be viable as part of an imaging system for use in fluorescence applications.

1.5.8 Theoretical Count Rate Maximum

A good estimate of the final local count rates for the C-DIR device can be found by searching for the limiting count rate, or the dead times, within individual components of the system. The first critical stage of the C-DIR, in terms of timing, involves the electron multiplication within the MCP of the photomultiplier. The dead time of individual pores has been determined to be around 10^{-2}s [79]. However, individual microchannel pores essentially act independently of each other. If the likelihood of a photo-electron exciting a pore within its dead time can be reduced, MCPs can realise much reduced dead times of ~10^{-6}s which translates to a 1MHz count rate [79]. The C-DIR anode itself was designed to have very low impact on the detector bandwidth and should not be a limiting factor on rates [1]. The NINO ASIC in combination with the HPTDC were designed to be ultra-fast. Each NINO channel can operate at a sustained rate of 10MHz [76]. The HPTDC has a programmable dead-time as low as 5ns and can be operated at a maximum rate of 16MHz [77]. Avoiding pile-up effects requires detection rate which is 10% the rep-rate of the excitation source as an upper bound, usually 1% is preferred [2] [23]. For fluorescence lifetimes which last 25ns this translates to a 40MHz laser rep-rate and 4MHz global count rate. In principle, the faster the lifetime under investigation, the

higher the allowed rep-rate. However, inter-pulse pile-up effects must be accounted for to find the true count-rate limitations. Figure 1.5-6 illustrates the conditions for

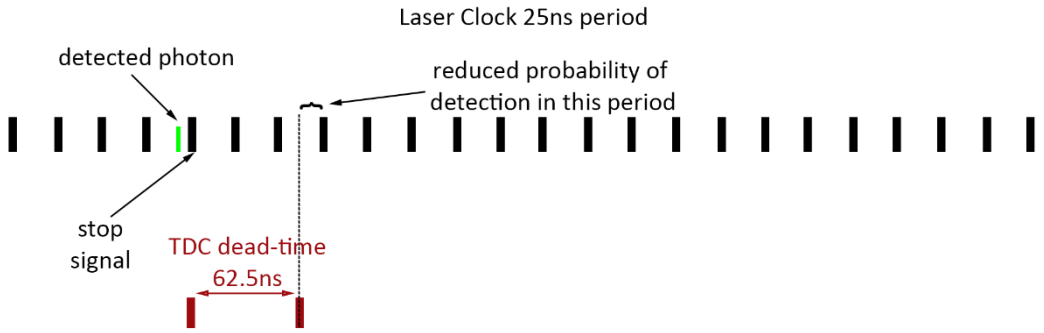

Figure 1.5-6 Full dead-time for the detection of a single is limited by the TDC dead-time. Inter-pulse pile-up occurs where the probability of detection of a photon is reduced within a laser period due to the over-lapping dead-time for recording the photon event. Over time, this distorts the lifetime signal. At least 75ns must elapse after the stop signal is received before a new event can be measured to avoid this pile-up. This translates to a theoretical 13MHz detection rate.

inter-pulse pile-up with the HPTDC read-out electronics assuming a 40MHz excitation source. Inter-pulse pile-up is a counting loss effect which occurs in high rep-rate experiments [23]. This occurs when the dead-time of the read-out electronics overlaps with a laser clock period during which a photon event could legitimately be detected. The probability of detection is reduced within the period since the electronics are blind for a part of it. This has the effect of distorting the fluorescence. The diagram shows that at least 75ns after the stop signal must elapse before the next photon can be measured. This limiting period represents a global maximum count rate of 13MHz which is 32.5% the 25ns rep-rate. Therefore, the system is MCP-limited for global count rates. It should therefore be possible to achieve a global count-rate of at least 1MHz which is twice that stated for the H33D XDL detector of ~500KHz [35] [55].

1.6 Conclusion

The C-DIR anode has the potential to be a high throughput, high time resolution, spatially resolved detector for fluorescence lifetime applications. Conneely et al. [40] have already demonstrated timing resolution <100ps using the NINO/TDC combination as read-out electronics for an MCP-PMT based multi-anode architecture. These high-speed electronics could theoretically produce global MCP-limited count-rates of ~1MHz outperforming other measurement systems in its class. The basis of this research project is to apply the capacitive division technique, by way of the C-DIR anode, to time-resolved fluorescence microscopy. The first major step is the characterization of the whole system (including NINO and HPTDC); determining the position resolution and timing resolution and finding necessary methods to improve the current design to maximize performance. The next stage involves careful identification and correction/elimination of sources of image non-linearity. The final stage of the project will be incorporating the system into a series of real experiments for data acquisition and fitting of time-resolved fluorescence data in 2D. This will prove the C-DIR system as a suitable system architecture for FLIM applications.

2 Simulation

2.1 Introduction

In preparation for receiving the hardware components which make up the C-DIR, a simulated version of the C-DIR detector was produced to facilitate development and testing of the final control software. This was a three-step process which firstly involved creating a large data set in the format expected from the TDC device. Secondly, a software interface between the data and the control software was developed which replicated the real hardware API. Finally, the development of a software framework which could manage the data acquisition, reduction and visualisation of this unique data format. High level software requirements included robustness, high acquisition speed and ability to cope with data streams on the order of 40MB/s. This chapter describes the development of the hardware simulation and the associated control software development.

2.2 HPTDC Output Data Format

Before attempting to create the "fake" data stream it was necessary to understand the NINO/HPTDC output in more detail. Figure 2.2-1 shows two defining characteristics of the NINO as a time-over-threshold (ToT) discriminator. The width of the digitized NINO pulse, or ToT, is sensitive to the magnitude of the input charge, especially for smaller charges. This relationship allows for imaging since the magnitude of the charge will vary at each read-out anode thus allowing a centroid to be determined. The sensitivity to the magnitude of the input pulse also affects the time resolution of the NINO. The leading-edge measurement shifts producing time walk, or amplitude walk, which must be corrected in order to realise the full timing

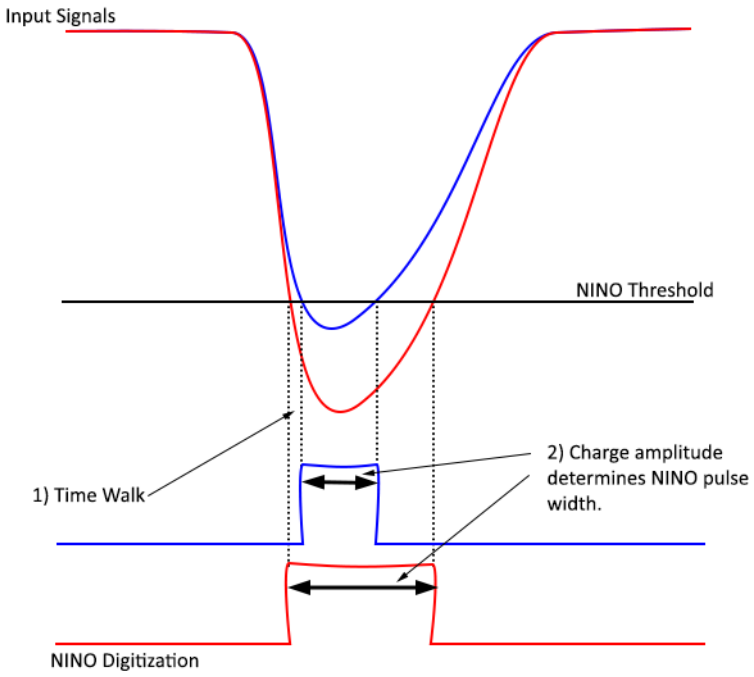

Figure 2.2-1 Principle of operation of the NINO as a TOT discriminator. Two characteristics of this type of detector are highlighted: 1) Increasing signal amplitude introduces a time walk effect despite constant rise time irrespective of amplitude. 2) The NINO pulse width (time over threshold) increases with increasing signal amplitude.

precision of the device. This implementation of the NINO ASIC digitizes charge on each of four input channels which are directly interfaced to the 4 corner readout anodes on the C-DIR. The charge is converted to a logic pulse whose width indicates the magnitude of the input charge. These four charges correspond to the four corner read-out nodes of the C-DIR anode. The leading and trailing edges of the logic pulse are time-stamped by the TDC separately. The resulting TDC output is a 32-bit (word) encoding of this timing information. Each of the four channels generate two words for leading and trailing time data for a single event. These eight packets are then enclosed by two additional header and trailer words. These represent events within a single TDC trigger window and indicates a group of words which belong to a single photon event. The data structure is as shown in Figure 2.2-2. The TDC event packet would have a total of 10 words, or 40 bytes, per event.

The theoretical throughput of the TDC is 40MB/s over USB 2.0 which corresponds to just over a 1 MHz event rate.

TDC Event Header

31	30	29	28	27	26	25	24	23	22	21	20	19	18	17	16	15	14	13	12	11	10	9	8	7	6	5	4	3	2	1	0
0	0	0	0	TDC				Event ID												Bunch ID											

Digitised Leading Edge of NINO Pulse

31	30	29	28	27	26	25	24	23	22	21	20	19	18	17	16	15	14	13	12	11	10	9	8	7	6	5	4	3	2	1	0
0	1	0	0	TDC				Channel			Inter.		Leading Edge Time																		

Digitised Trailing Edge of NINO Pulse

31	30	29	28	27	26	25	24	23	22	21	20	19	18	17	16	15	14	13	12	11	10	9	8	7	6	5	4	3	2	1	0
0	1	0	1	TDC				Channel			Inter.		Trailing Edge Time																		

TDC Event Trailer

31	30	29	28	27	26	25	24	23	22	21	20	19	18	17	16	15	14	13	12	11	10	9	8	7	6	5	4	3	2	1	0
0	0	0	1	TDC				Event ID												Word Count											

Figure 2.2-2 TDC 32 Bit Packet Formats for the event header/trailer and the leading/trailing edge measurements when using the TDC in very high resolution (25ps) resolution mode. The four most significant bits represent the packet type, the next four bits are a TDC identifier for situations where multiple TDCs are coupled together. For the timing packets, the 21 least significant bits represent the timing data.

Once TDC data is successfully generated by the photon counting electronics, the data must be decoded to determine the incident charge on the C-DIR anode. Probing the NINO response to an input charge and characterizing the relationship between charge and ToT, or pulse width, gives rise to two approaches which could be used to determine the incident charge from the calculated NINO pulse width. Figure 2.2-3 provides an example of this relationship for each of the four NINO channels.

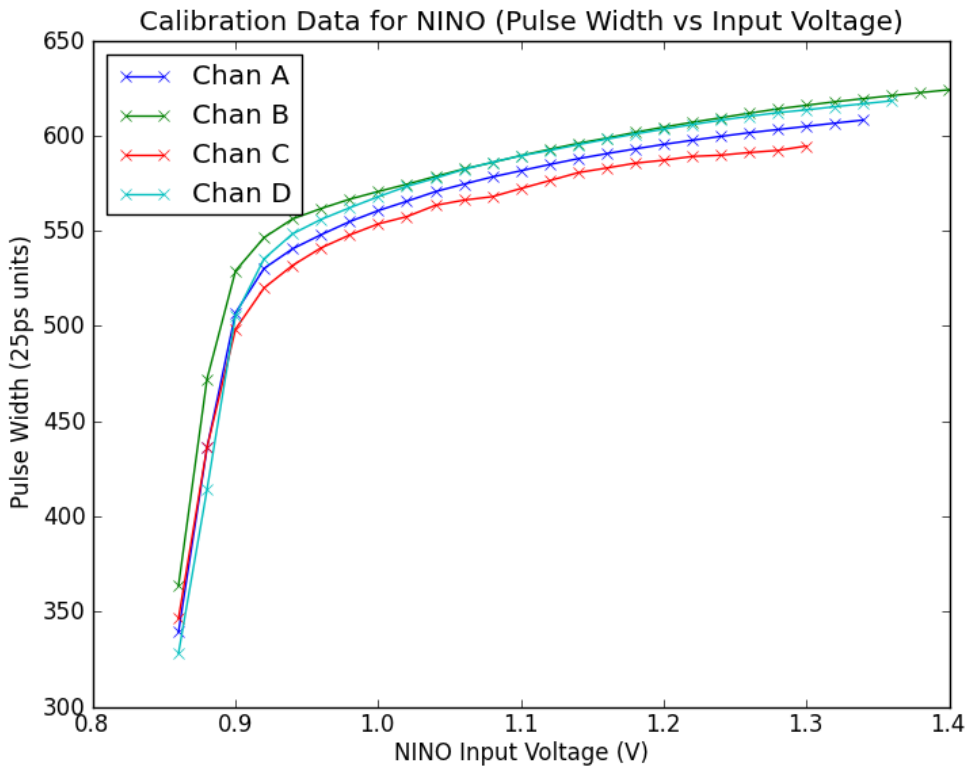

Figure 2.2-3 Sample ToT response to input charge measured using the 4-channel NINO ASIC used in this study.

The first approach involves generating a mathematical expression by performing a fit on the data for each channel. Although this could, in principle, yield a very accurate representation of the behaviour, performing a complex calculation on an event-by-event basis would be computationally expensive. The second, more attractive approach would be to interpolate the collected data and generate look up tables of ToT vs input charge. Storing this lookup table in memory would allow for very fast C-array type access which would free up processing time for other areas of the software. For the purposes of the TDC hardware simulation, a simple mathematical expression was used to describe the ToT charge relationship. In the final software implementation, lookup tables were employed since they were mapped to a more realistic charge space which comfortably fit within memory. The remainder of this chapter focuses on generating a realistic dataset which simulates

the TDC output, developing a hardware simulator which acts as an interface between this data and the control software, and the development of the control software.

2.3 Detector Modelling and Simulated Data

There were two choices for the programming language to use for the generation of this data-set namely python and C++. The C++ programming language was ultimately chosen due to the speed in generating large datasets using complex mathematical expressions.

2.3.1 Pulse Width (TOT) vs Charge Relationship

For this exercise, an arbitrary pulse width to charge relationship was defined using the following polynomial:

$$\boldsymbol{p_i = \sqrt{Q_i} \quad i \in \{1, 2, 3, 4\}} \qquad \textbf{2.3-1}$$

Where p_i is the pulse width and Q_i is the incident charge at each of the corner anodes.

2.3.2 Fluorescence Decay

The leading time portion of the timing data was generated using an exponential distribution which mimics a fluorescent species with a single decay component taking the form shown in equation 1.1-1. Time is assumed to be in units of nanoseconds with τ taken to be 2.6ns. A delay of 5 ns was added to this exponential distribution in the form of a normal distribution with a σ 25ps which corresponds to the leading-edge jitter on the NINO ASIC. The C++ STL random library was used for the generation of this distribution which produced pseudo-random lead time information as shown in Figure 2.3-1

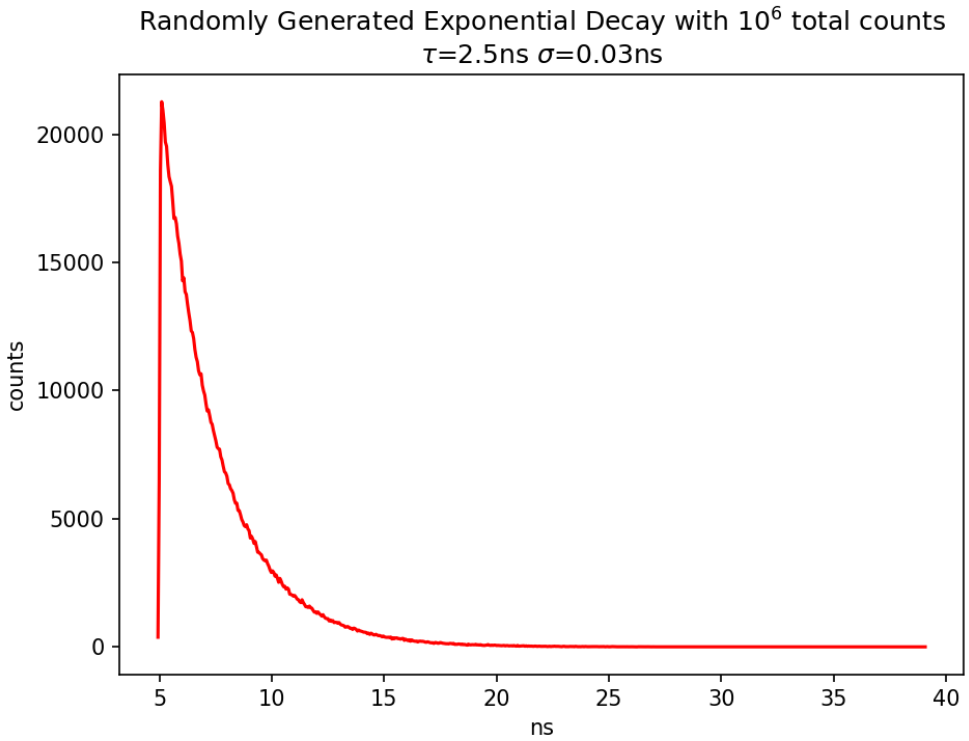

Figure 2.3-1 Randomly generated lifetime decay using the C++ STL random library. The lifetime τ was set to 2.5ns with an error σ of 0.03ns. This represents the leading/trailing edge data for the sample dataset.

2.3.3 Photomultiplier response

The pulse height distribution of the photomultiplier was generated using a normal distribution. Although the actual charge response of a PMT is not perfectly Gaussian this distribution sufficed as a reasonable substitute for the purposes of this simulation. The charge distribution was centred on 10e6 arbitrary units reflecting the 10e6 gain characteristics of the MCP PMT with dual microchannel plates. A dark

noise offset of 5000 was also defined. The result is shown in Figure 2.3-2

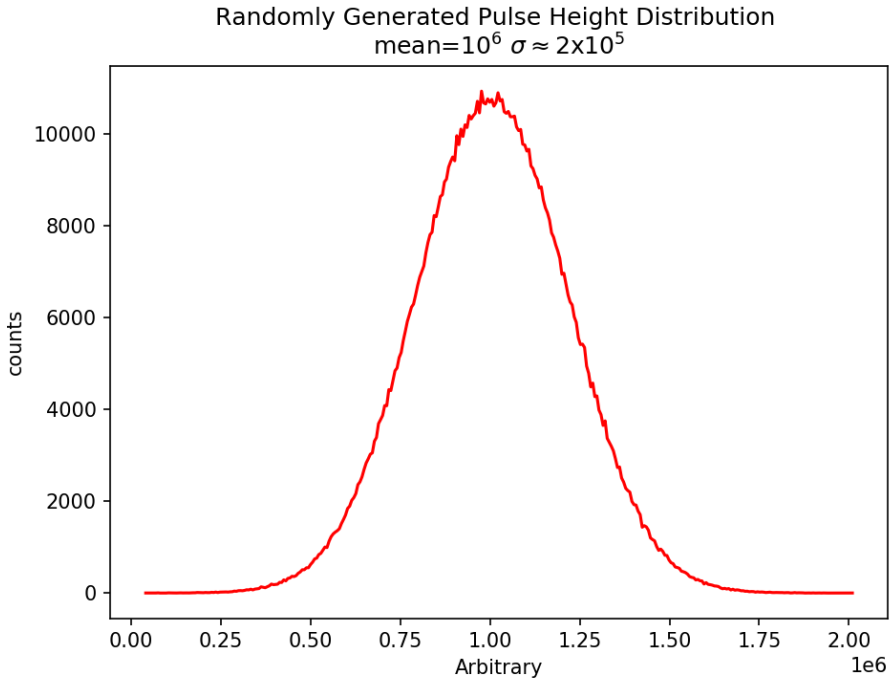

Figure 2.3-2 Randomly generated PHD which represents the total incident charge on the C-DIR detector. This was used in the generation of the fake dataset.

2.3.4 Pixel Coordinates (Charge position)

Position coordinates were calculated using digital bitmap images. 8-bit grayscale bitmap files were a convenient choice because each pixel value corresponds to a luminance value. Figure 2.3-3 shows the image used for the

Figure 2.3-3 8-bit grayscale bitmap image used for the generation of the fake detector data.

generation of the test dataset.

The monochrome luminance values were used to create a 2-dimensional probability distribution which was randomly sampled to produce image coordinates. This was achieved by loading the bitmap data and summing all the pixel values. The image was then normalised with respect to intensity thus producing a 2-dimensional probability distribution. This was then randomly sampled to produce a user-defined number of (x, y) coordinates used to spawn the dataset. This was achieved by randomly selecting a location (x, y) and a random value p which represented the probability of a photon count at that location. If the probability at that location from or normalised 2-D vector was greater than or equal to p, an event was generated for that location. This is illustrated in the code snippet Figure 2.3-4.

```
for (int i = 0; i < numEvents;) {
  x = (int)(width * randValue());
  y = (int)(height * randValue());
  p = max * randValue();

  if (norm[(y * width) + x] >= p) {
    r = getBrownConradyR(x, width / 2, y, height / 2);
    distx = distortX(x, y, r);
    disty = distortY(y, x, r);
    outputEvents(distx, disty);
    i++;
  }
  count++;
}
```

Figure 2.3-4 Code snippet which demonstrates the random sampling of position coordinates when generating the test data-set. A grayscale bitmap image is normalised and represents the probability distribution of photon counts at each pixel location. (x, y) and p are randomly selected. If the probability at (x, y) is greater than or equal to p a photon event at this location is generated.

In the above snippet, $numEvents$ is a user-defined variable which represents the total number of photons to be written to the data file. It is important to note here that for each coordinate pair a new charge and lead time are randomly generated for each of the four channels. This will be expanded on later.

2.3.5 Distortion

After each coordinate was generated, distortion was applied to the coordinate. Distortion of some form, whether radial or tangential, is a feature of most imaging systems which needs to be accounted for. The Brown-Conrady distortion model was chosen due to its simple formulation and the presence of both radial and tangential coefficients. Limiting the infinite series to two terms for each distortion type produced:

$$\boldsymbol{r = \sqrt{(x_d - x_c)^2 + (y_d - y_c)^2}} \quad \textbf{2.3-2}$$

$$\boldsymbol{x_u = x_d + (x_d - x_c)(K_1 r^2 + K_2 r^4 + \cdots) + (P_1(r^2 + 2(x_d - x_c)^2) + 2P_2(x_d - x_c)(y_d - y_c))(1 + P_3 r^2 + \cdots)} \quad \textbf{2.3-3}$$

$$\boldsymbol{y_u = y_d + (y_d - y_c)(K_1 r^2 + K_2 r^4 + \cdots) + (2P_1(x_d - x_c)(y_d - y_c)\, P_2(r^2 + 2(y_d - y_c)^2))(1 + P_3 r^2 + \cdots)} \quad \textbf{2.3-4}$$

Where (x_u, y_u) are the undistorted centroid position coordinates, (x_c, y_c) are the distortion centre, here assumed to be the geometric centre of the anode, (x_d, y_d) are the resulting distorted coordinates, r is the distance between the distortion centre and the charge position, and K_i and P_i are the radial and tangential distortion coefficients respectively.

2.3.6 Generating the Dataset

Once the charge, position and lead time were determined, the TDC packet data could be constructed. The anode geometry, Figure 1.5-2, and position centroid calculations, 1.5.1 – 1.5.2, were defined in the previous chapter. By randomly selecting the total charge Q and the charge on one anode Q_A, for example, we get

$$\boldsymbol{Q = Q_A + Q_B + Q_C + Q_D} \quad \textbf{2.3-5}$$

Where Q is the total incident charge. This gives:

$$Q_C = Q - Q_A - Q_B - Q_D \quad \textbf{2.3-6}$$

So that the other charges can be determined using:

$$Q_B = xQ - Q_A \quad \textbf{2.3-7}$$

$$Q_D = yQ - Q_A \quad \textbf{2.3-8}$$

where x and y are taken from equations 1.5-1 and 1.5-2 respectively. Substituting each charge in equation 2.3-1 gives rise to pulse width values for each anode which can then be used to calculate the fake TDC data packets. A test data file was created which contained ~1.5×10^8 events. The resulting file was 5.46 gigabytes in size which provided a suitable dataset for the design of a dummy HPTDC device. This corresponded to approximately 2.5 minutes of data at the maximum theoretical throughput.

2.3.7 Qualitative Verification

A python script was developed to provide a quick method for qualitatively verifying the dataset. The script loaded a user-defined limited subset of the data file and produced a 2D histogram of the events in addition to histograms of the timing and pulse height distribution. The decoder operates under the assumption that the first 32-bit word in the file is a packet header based on the format described in Figure 2.2-2. Data is consumed from file ten 32-bit words at a time and unpacked used the python struct library.

The position, time and charge were extracted on an event-by-event basis and used to construct three histograms. Figure 2.3-5 shows the original image compared to the reconstructed image with 1000, 10,000 and 10,000,000 counts.

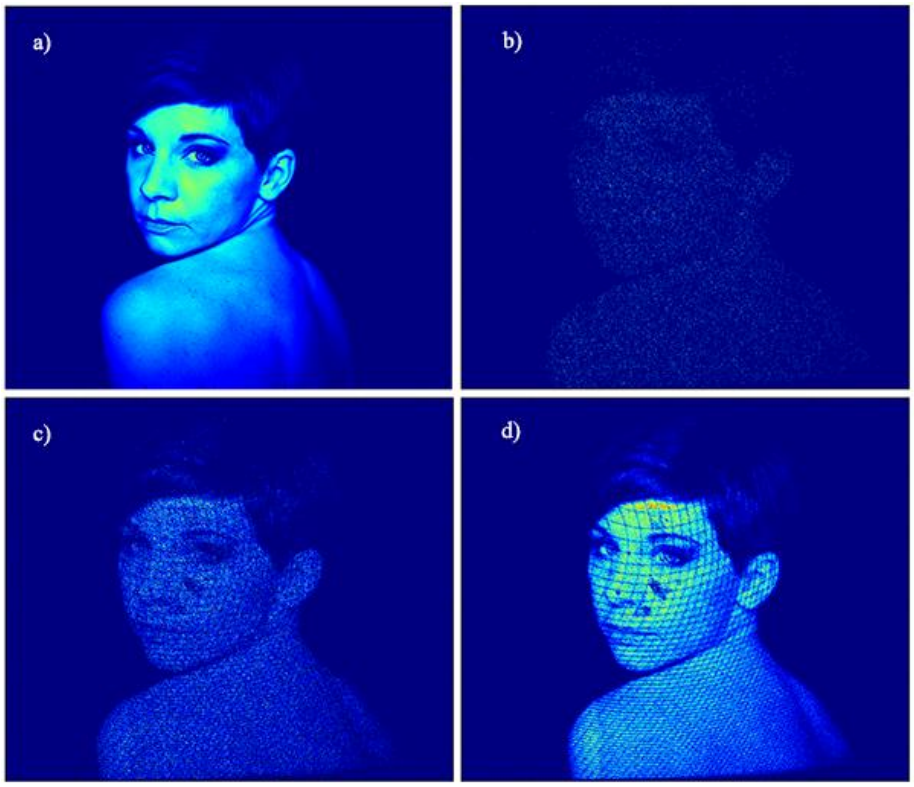

Figure 2.3-5 a) Original image b) Reconstructed image with 1000 counts. c) Reconstructed image with 10000 counts d) Reconstructed image with 10,000,000 counts. Notice noise and distortion present compared to the original image due to the noise added to the charge and timing, as well as the Brown-Conrady distortion model.

construct three histograms. Figure 2.3-5 shows the original image compared to the reconstructed image with 1000, 10,000 and 10,000,000 counts. Figure 2.3-6 shows the reconstructed time-of-flight and pulse height distribution of the simulated events.

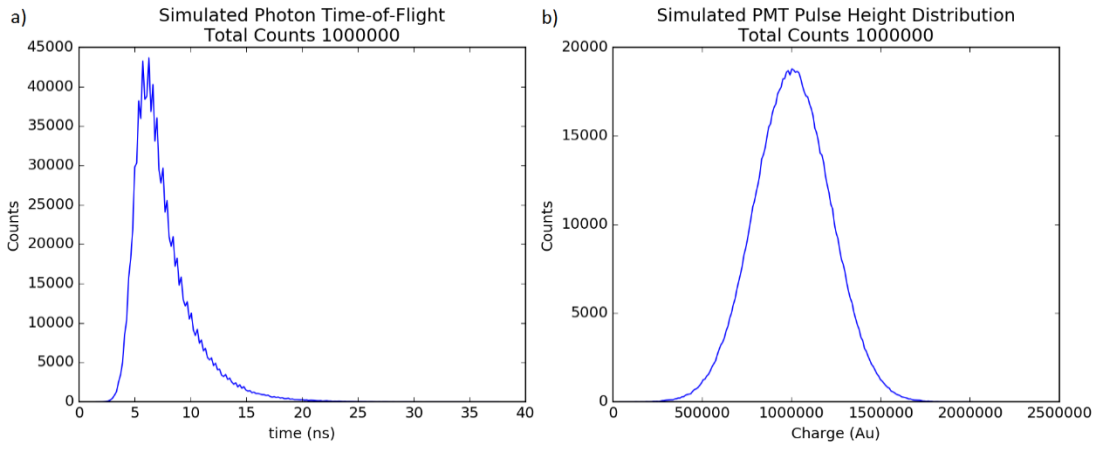

Figure 2.3-6 a) Time-of-flight b) Pulse height distribution

The dataset contained sensible data which could then be used for the development and testing of a data reduction platform for handling the processing of this data format.

2.4 Hardware Interface Simulation

A dummy HPTDC device layer called *HPTDCSim* was created. This served as an interface to the large dataset produced in the previous section. This facilitated further development of the final graphical user interface without the need for the actual hardware to be present. The major benefit being reduced dependency on delicate photon counting equipment. This library interface was written to deliberately mimic the real hardware interface of the HPTDC API developed by Thomas Conneely as a basis for the development of the control software. The hardware simulation interface for the HPTDC is shown in Figure 2.4-1. The fake device provided a configurable data rate between 5 and 40 MB/s in steps of

```
class DLL HPTDCSim {
public:
  enum DataRate {
    DataRate_40 = 25,
    DataRate_35 = 25,
    DataRate_30 = 25,
    DataRate_25 = 25,
    DataRate_20 = 20,
    DataRate_15 = 15,
    DataRate_10 = 10,
    DateRate_5 = 5
  };

  explicit HPTDCSim(const std::string &filename);
  ~HPTDCSim();

  void connect();
  void disconnect();
  bool isConnected();
  void getData(char *userData, size_t size);
  void setDataRate(DataRate dataRate);

protected:
  HPTDCSim(const HPTDCSim &) = delete;

private:
  void kill();
  void _execThread();

private:
  bool run;
  bool connected;
  std::queue<char> buffer;
  const unsigned int bufferSize;
  DataRate m_rate;
  std::thread m_thread;
  const std::string m_filename;
  std::mutex dataLock;
  bool eof;
};
```

Figure 2.4-1 The class design/interface for the HPTDC hardware simulation. This was designed to mimic the C++ interface for the actual HPTDC device with a few additions for controlling data-rates. The hardware simulation allowed for throttling the input data rate from 5MB/s up to the theoretical maximum of 40MB/s.

5MB/s consistent with the maximum theoretical USB 2.0 data rate. Data acquisition from file was controlled using a single read thread which also owned a handle to the data. The action of this thread is shown in Figure 2.4-2. Data was loaded into a variable size FIFO memory buffer with maximum size around 1GB. Mutually

```
while (run && !eof) {
    if (buffer.size() < bufferSize) {
      dataLock.lock();
      // Copy 1MB and pause to satisfy data rate
      for (int i = 0; !dataFile.eof() && (i < 1048576) &&
                      (buffer.size() < bufferSize);
           i++) {
        dataFile.read(&byte, 1);
        buffer.push(byte);
      }
      dataLock.unlock();
      std::this_thread::sleep_for(
          std::chrono::milliseconds(1000 / static_cast<int>(m_rate)));
      eof = dataFile.eof();
    } else {
      // Sleep for 50ms
      setBufferOverflowSignal();
      std::this_thread::sleep_for(std::chrono::milliseconds(50));
    }
  }
```

Figure 2.4-2 The read thread source snippet which shows the copying and buffering of data in 1MB chunks for each loop iteration. The thread was throttled used a simple sleeping mechanism to produce the desired data rate.

exclusive (mutex) locks were used to synchronize memory access in this multi-threaded environment and prevent data races when accessing the memory buffer which stored the TDC Data. Client software could then remove data from the buffer for further processing using the *HPTDCSim::getData* method. Monitoring the FIFO buffer provided information on whether data was being loaded at the correct rate. The buffer limit of 1GB was never reached, and there were never any buffer overflow signals when used in conjunction with the client code processing which shows that the data rate was not exceeded for the test system.

2.5 Control Software

2.5.1 Requirements

The high-level performance requirements for the control software were mentioned in the beginning of this chapter. There were also other commercially-driven requirements which fed into the overall software design process. The

software requirements for this project can be split into three categories; performance, graphical user interface (GUI) and functional requirements. Table 2.5-1 provides an overview of the software requirements for this project.

Table 2.5-1 Overview of C-DIR Software Requirements

Category	Requirement
User Interface	The user must be able to easily connect/disconnect to HPTDC hardware.
	The user must have the option to configure the TDC device.
	The user must be able to toggle a live histogram of intensity (total counts).
	The user must be able to set an integration period for photon events.
	The update rate of the GUI should be configurable.
	The user must be able to toggle a live histogram of timing data for each channel.
	The user must be able to toggle a live pulse height distribution for each channel.
	The user must be presented with full system diagnostics for each channel (count rate, buffer levels, etc.)
	The user must have a mechanism for saving experiment data.
Performance	The software must be able to cope with a USB 2.0 40MB/s maximum theoretical data rate.
	The software must maintain data integrity. No data should be lost.
	The software must prioritise the saving of experimental data over visualization.
	The software should be robust and reliable.
	The software should employ a variable size buffer to cope with hitches in system performance.
Functional	The software should log all activities with varying levels of detail (notice, information, debug, error).
	The software should alert the user of any hardware failure (TDC drop-out, PMT overbright, dead channels on the NINO).
	The software should gracefully shutdown when fail conditions arise.

2.5.2 Data Storage Format

The output data format was chosen to be in event mode. This sparse format consisted of recording the position (x, y) and time, t of an event sequentially as they were processed from the raw TDC packets. This approach was chosen since it allows for a more compact and storage-efficient representation of the data compared to storing large numbers of sparsely populated images which would have resulted in rapidly exhausting storage media with very little benefit. Immediate histogramming of timing and intensity data was also an option. Although this could further reduce storage, it meant sacrificing individual photon event information before any kind of analysis could be performed. Histogramming would also require complex data structures and additional computing power which would be better invested in maintaining high data consumption rates. Histogramming was therefore left as a post-processing step for visualization and exporting to other analysis packages which required this format. The sparse format offered the best trade-off for storage and speed.

2.5.3 Language, Libraries and Platform

C++ was chosen as the language for the entire implementation of the control software. This language allowed for the development of very fast, multi-threaded design. Low level data handling code was abstracted away from GUI presentation logic, however, the open source Qt C++ API was used as the basis for GUI presentation. The first attempt at GUI implementation was performed using high level APIs in Java which were interfaced with low level C++ data structures using the Java Native Interface (JNI). This proved to be extremely cumbersome to use and even more difficult to maintain from a commercial standpoint. Qt provided a much simpler and more straightforward alternative. Histogramming was achieved using

the GNU Scientific Library (GSL) while the QCustomPlot Qt based plotting library was used to for displaying data. The pantheios logging library was used within the low level bus component. Pantheios employs an asynchronous file writing mechanism which results in very little overhead for logging output. However, verbose logging levels can result in a slow down in the system so this functionality was rarely used unless running tests or debugging issues. The target platform selected for the final software was windows since the HPTDC device only had windows drivers available at the time of the development. The relationship between these interfaces is further explained in the following section.

2.5.4 Design and Implementation

The architecture of the low-level data handling portion of the control software took a simple linear bus structure. Figure 2.5-1 shows the data flow and interdependencies

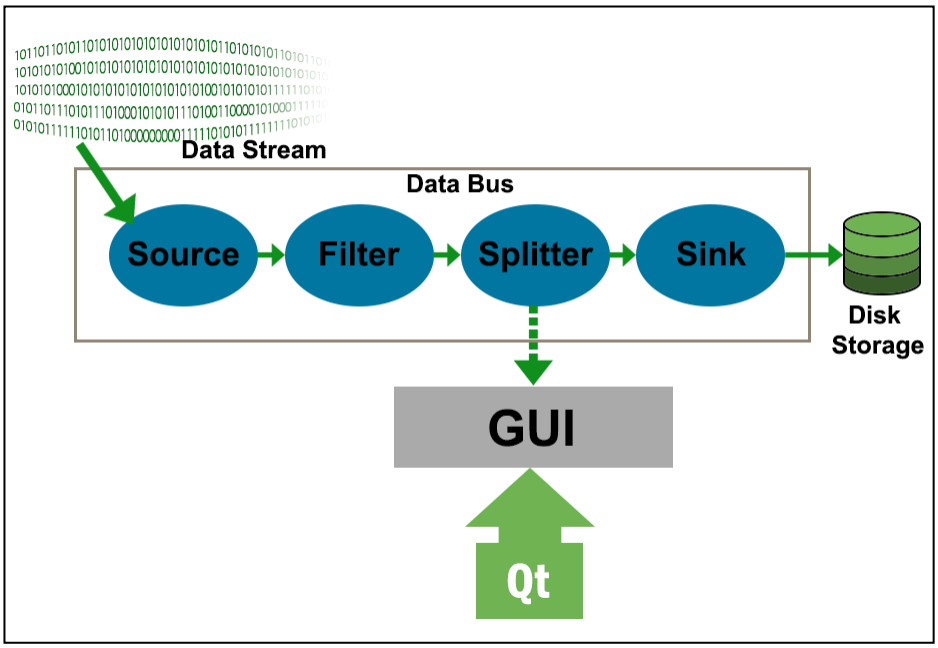

Figure 2.5-1 Basic structure of control software. Arrows indicate the movement of data. The bus acts as a listener to the HPTDC data stream and conveys data to each bus component. The source component reduces data to the final sparse position and time format, the filter removes unwanted events, the splitter conveys data to the sink which asynchronously writes data to disk in chunks. The GUI thread samples the splitter at regular intervals and displays a live update of photon events and detector diagnostics.

between all the parts which make up the software processing. This architecture allowed for the abstraction of GUI presentation logic out of low level data handling which improved debugging and maintainability. Changes could be made to the data-handling with minimal to no impact on GUI code. The simplicity of the bus architecture also facilitated speed optimisations without worrying about unnecessary code complexity. Bus architectures are also widely used for data streaming technologies and therefore allowed the use of existing ideas without re-inventing the wheel producing new code. The data is made up of four main portions: source, filter, splitter and sink. Each component implements a *BusComponent,* Figure 2.5-2, whose interface allows for the conveying data from one component to the next as well as some thread synchronisation handles. The over-arching *Bus* owns all bus

```
class BusComponent {
public:
	BusComponent()
	virtual ~BusComponent()
	virtual void receiveData(void *data)=0;
	virtual void *getProcessedData()=0;
	HANDLE GetEndEventHandle();
	HANDLE GetThreadHandle();
	HANDLE GetParentSignal();
	uint64_t getNumProcessed();
	void Terminate(bool input);
}
```

Figure 2.5-2 Interface for the *BusComponent* base class which implements common functionality for all data bus components in the software.

components and is responsible for conveying data to the source and setting up thread queuing between components. The bus also owns a handle to and manages the

```
class Bus{
public:
	Bus();
	virtual ~Bus();
	SourceComponent *source;/**< Source bus component*/
	Filter *filter;/**< Filter bus component*/
	Sink *sink;/**< Sink bus component*/
	Splitter *splitter;/**< Splitter bus component*/
	GUIAnalysisModule *imageAnalysis;/**< Image Analysis
Module*/

	/*Debugging/Diagnostic Methods*/
	HANDLE getBusThreadHandle();
	uint64_t debugGetBytesProcessed();
	bool debugIsIOTerminated();
	bool debugIsProcessingComplete();
	uint32_t debugGetPacketsIn();
	uint32_t debugGetPacketsOut();
	_declspec(dllexport) uint64_t getEventsProcessed();
	_declspec(dllexport) virtual void Start()=0;
	_declspec(dllexport) virtual void Stop()=0;
	_declspec(dllexport) void Pause();
	_declspec(dllexport) void Resume();
	_declspec(dllexport) virtual int32_t HPTDCConnect()=0;
	_declspec(dllexport) virtual int32_t HPTDCDisconnect()=0;
	_declspec(dllexport) virtual void ConfigureHPTDC(uint32_t
trigOffset, uint32_t matchWind)=0;
	_declspec(dllexport) virtual int32_t HPTDCInit(char *)=0;
	_declspec(dllexport) virtual string
printStatusRegister()=0;
	_declspec(dllexport) virtual void setDemoFilename(char
*filename)=0;
	_declspec(dllexport) bool isThisDemo();
	_declspec(dllexport) HANDLE getCompleteSignal();
	_declspec(dllexport) void setBufferSize(uint32_t size);
protected:
	virtual void BusController(void) = 0;
	static void busThread(Bus *_this);
	void resumeThreadSecure(HANDLE thread);
};
```

Figure 2.5-3 The *Bus* interface which controls the synchronization of data through each component as well as conveying data to the GUI. The bus also maintains a connection to the HPTDC device.

connection between the client code and the HPTDC device. The bus acts as a listener to the incoming TDC data stream and appends data to a dynamically resizing FIFO buffer. This buffer compensates for instances where processors may be overloaded and temporarily unable to cope with high data rates. In order to maintain high speed processing and make use of the multiprocessor architecture in

most computers, the data listener and all components each run in their own separate thread.

The source component has dual functionality. It optionally spools incoming raw data to disk asynchronously and converts incoming raw HPTDC packets to processed event data. The input raw data takes the form of a C-array and uses the structure shown in Figure 2.5-4. Raw data is processed in a similar way to that

```
typedef struct Raw{
      char *data; /**<Buffer which stores the raw data from the
HPTDC*/
      uint32_t size;/**<Size of data field*/
} RawData;
```

Figure 2.5-4 Structure of the raw data packets which are accepted by the source component for spooling to disk and reduction to position and timing data.

mentioned in 2.3.7 without the assumptions on the beginning of the data stream. The final solution makes use of a lookup table for fast pulse width to charge determination. The processed data packets which are passed downstream to other components of the data bus takes the form presented in Figure 2.5-5.

```
/** \struct CoordTime
\brief Stores the position and arrival time of a single photon
event
*/
typedef struct{
      uint16_t x;/**<Stores the calculated x coordinate for a
photon event.*/
      uint16_t y;/**<Stores the calculated y coordinate for a
photon event.*/
      uint32_t t;/**<Sores the calculated arrival time for a
photon event.*/
} CoordTime;

/** \struct XYTData
\brief Stores position and arrival times for all events within
the data packet received by a bus component
*/
typedef struct XYT{
      CoordTime *data;/**<Stores the position and arrival time
for all events within data packet accepted by bus component*/
      uint32_t size;/**<Number of events within data packet
accepted by bus component*/
      uint32_t triggers;/**<Number of elapsed tdc triggers
between the first and last set of events in this packet. Used
for exposure time calculations*/
} XYTData;
```

Figure 2.5-5 Reduced data format which stores position and time. This is calculated in the source component and passed along the bus for filtering, spooling to disk and display in the GUI.

Data passed on to the filter undergoes very minimal noise filtering within the filter component. Filtering for the most part deals with vetoing invalid events for position, for example a position outside the physical detector region. The filter also performs basic Brown-Conrady inverse distortion correction. The source component itself performs preliminary filtering removing incomplete events where all NINO channels do not produce timing information.

The splitter component provides an interface to the GUI where filtered data can be sampled at regular intervals. The splitter also conveys all data to the sink which is responsible for asynchronously writing data to disk. The default behaviour of the sink is to write all received data to disk. This component makes use of the

Microsoft asynchronous file writing library which maintains its own memory buffer for maintaining data integrity.

The basic structure of the GUI and the interplay with external libraries and low-level data handling is shown in Figure 2.5-6. This modular approach to design

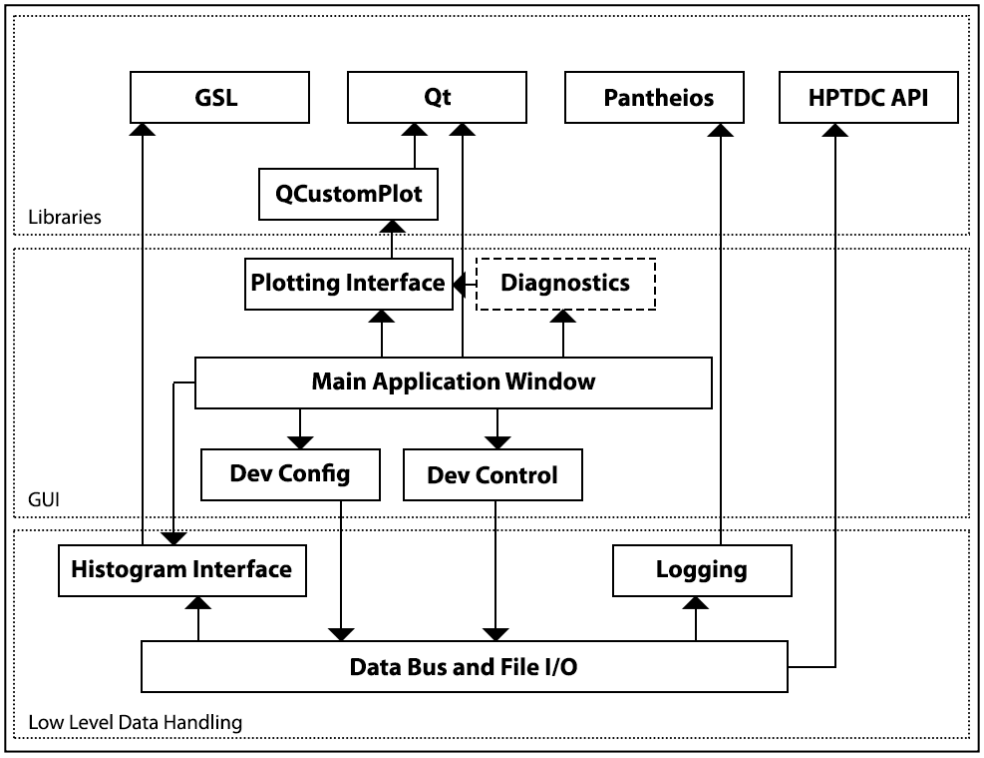

Figure 2.5-6 Basic GUI Structure. Arrows indicate dependencies between items. The diagnostics is optional and can be switched off. This module refers to detailed output of each channel in terms of charge and timing information which is only important for commissioning and testing. These should not be of interest to end users.

facilitated easier testing, design and maintainability as dependencies were not heavily coupled to the GUI or any other parts of the software. Figure 2.5-7 demonstrates our test data set loaded into the control software using our simulated HPTDC device. The image and timing data are both accurately reproduced.

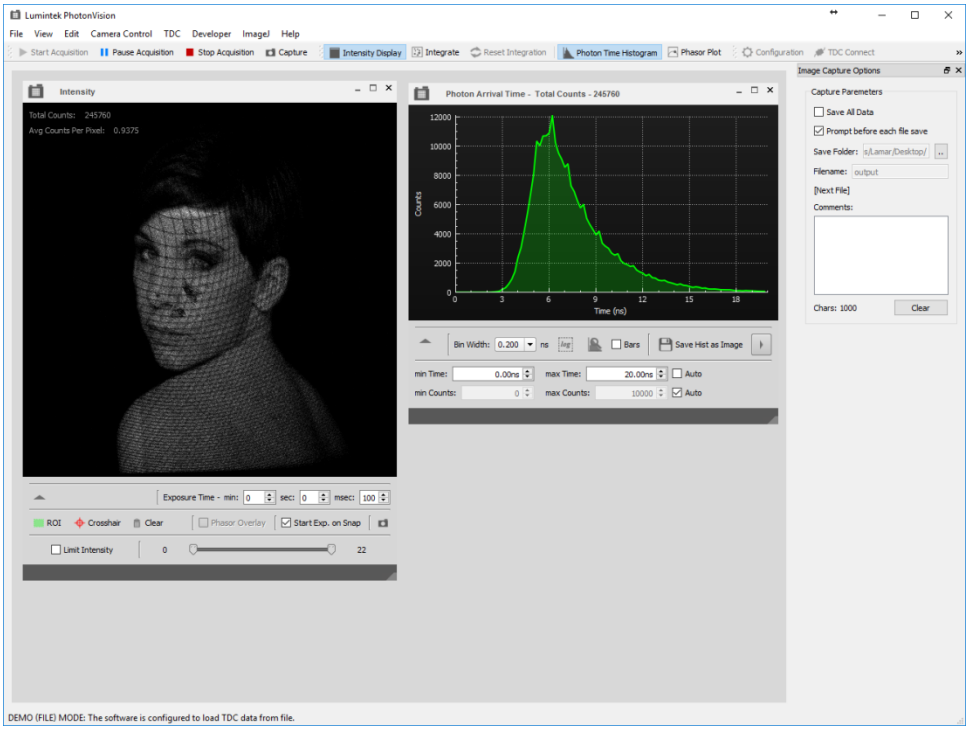

Figure 2.5-7 The final GUI using the HPTDCSim data.

2.5.5 Target Platform and Hardware Requirements

The computer hardware used for the development and testing of the HPTDC hardware simulation and the final control software was a Dell Latitude 8GB RAM, 2.4GHz core i5 with a 7200rpm 500GB HDD (SATA). Later tests made use of a Dell XPS 16GB RAM, 2.5GHz core i7 with a 256GB SSD (SATA). The target platform was Windows 7. The Dell Latitude configuration was initially considered the minimal hardware configuration since the software was guaranteed to process data at the USB limited rate in this situation. The laboratory system which was used to drive the experiments was a Windows XP 64-bit platform with a Pentium Core 2 Quad processor and 5400rpm HDD. Even with this significantly dated hardware configuration data acquisition at the maximum rate was achievable. This demonstrates the robustness of the software design. The effects of using spinning disk drives or slower CPU configurations were not investigated beyond this.

2.6 Third-party Fitting Software

Fitting libraries were time-consuming to embed into the existing data-reduction framework, therefore the option to use open-source, well tested and maintained third-party software seemed more attractive. The Mantidplot and TRI2 software packages were used for fitting exponentials to the timing data in one and two dimensions respectively. Mantidplot, developed at the ISIS spallation source, is data reduction software primarily designed for the reduction of neutronic data. However, it contains a general purpose fitting tool and a mechanism for loading ASCII files with no assumptions on the input units. The TRI2 software package, developed at Oxford University, is specifically for time-resolved fluorescence data analysis. The input data type (*.tri) is a volume where the first two dimensions represent image position and the third timing data. Making use of these packages required the development of external scripts which could be used to export the sparse XYT event format to the desired formats for analysis.

Figure 2.6-1 shows MantidPlot used to produce an exponential fit of our timing data from 2.3. The fluorescence lifetime of 2.6 is accurately recovered by fitting the data to the fluorescence model presented in equation 1.1-1.

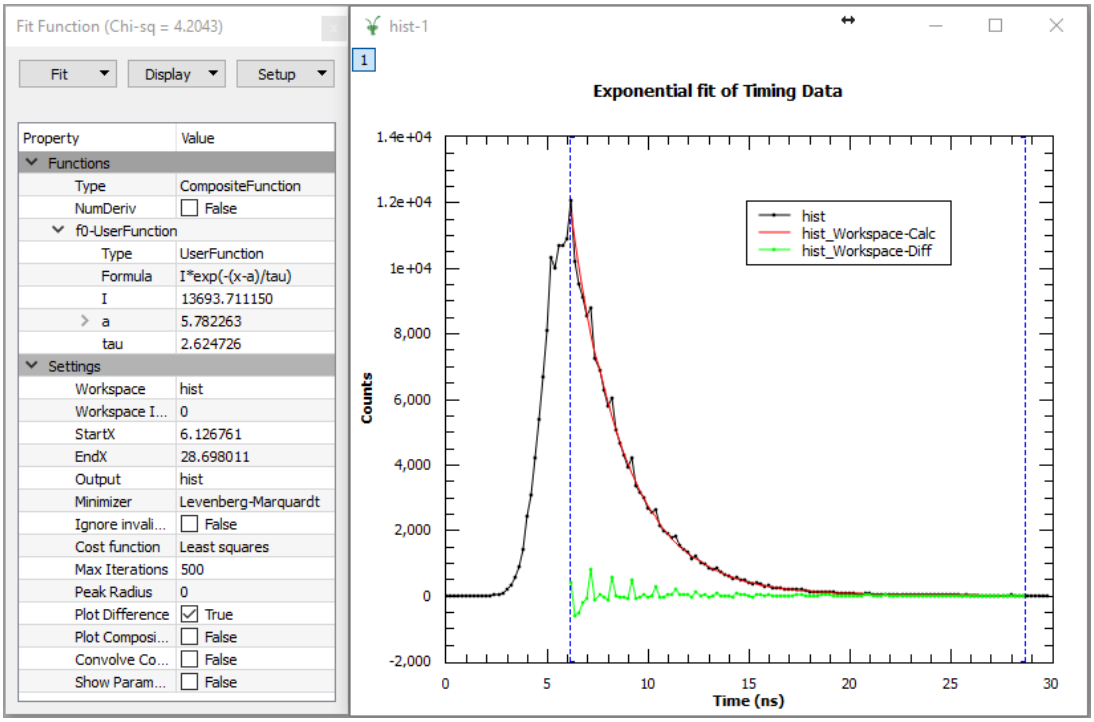

Figure 2.6-1 Exponential fit of timing data revealing accurate recovery of the lifetime 2.6ns.

2.6.1 A More Realistic Fitting model

The previous section describes using a tail fit of the fluorescence lifetime data. This essentially involves disregarding any contribution of the excitation pulse and analysing the trailing decay in isolation (see 2.3.2). For the purposes of simulated data this is sufficient since a noisy exponential decay pulse was used, however when fitting to an actual dataset this may yield incorrect results. Examining the physical setup of a fluorescence system might provide some insight as to why a tail fit may only be telling part of the story of the decay profile observed from a sample.

Fluorescence decays observed in nature are a result of a response to excitation. The excitation energy stimulates the fluorescent molecule which then non-deterministically returns to its ground state by emitting some of the excitation energy. In practice, lasers are used to stimulate a sample within a microscope system. The previous section indirectly assumed that the excitation energy was in

the form of a delta function, or in other words, the excitation pulse has zero width Figure 2.6-2. This ideal situation is useful for understanding the actual mechanism

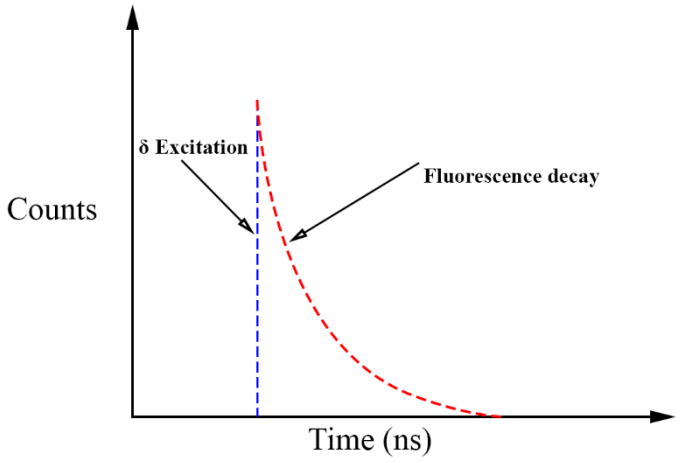

Figure 2.6-2 An idealised delta (δ) function excitation pulse which determines the initial amplitude of the fluorescence decay.

by which fluorescence decays occur. Figure 2.6-3 shows a more realistic scenario

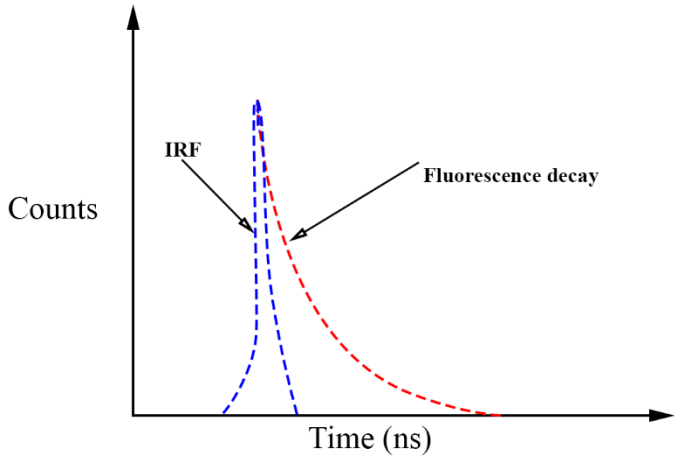

Figure 2.6-3 A more realistic example of fluorescence decay. The IRF is measured in the absence of a sample. The measured fluorescence decay is treated as the convolution between the IRF and the exponential decay of the fluorophore. Hence a more realistic model would take the IRF into account.

for the excitation of a fluorophore. Here, the instrument response function (IRF) replaces our idealised δ-function. The IRF represents the limiting resolution of our imaging system and is usually measured by replacing the sample with some sort of control (which could be an empty sample holder). In other words, it is a measure of

how our system responds to an impulse. In practice, laser pulses are sufficiently narrow in time to be treated as a delta function impulse for the system. The laser pulse width is usually on the order of tens of picoseconds. The impulse response or IRF is usually between hundreds of picoseconds to a few nanoseconds.

For time-domain analysis, the final measured fluorescence decay in TCSPC is treated as the convolution between this response and the exponential decay associated with the fluorophore

$$\boldsymbol{I(t) = L(t_2) \otimes F(t)} \qquad \textbf{2.6-1}$$

where $L(t)$ is the IRF and $F(t) = e^{-(t-t_2)/\tau}$ which is our familiar fluorescence decay [2]. These equations represent the basis of physical models used by software packages developed for analysing FLIM data.

2.7 Conclusions

Early software development in parallel with hardware testing allowed the removal of several bugs and continuous improvements to the final control software before any real data was collected. This inspired confidence in the stability and correctness of the data acquisition and early treatment of the data before analysis. The simulated data and HPTDC device also provided a platform to rigorously test performance requirements against the implementation. The results clearly demonstrate that the design is robust since the application is capable of storing and reducing data at the specified data rates as well as driving the graphical user interface without compromising the base level performance requirements.

2.7.1 C-DIR Software Product

The software managed to maintain stability and data integrity even at the maximum theoretical rate of 40MB/s. This was tested using a python script to generate a large fake data file which was then fed to the software at this rate using the hardware simulation in 2.4. Raw data outputs were compared with the original file. The software has since been adapted for commercial use with both the C-DIR system and a proprietary version of the XDL system at King's College University.

2.7.2 Improvements

The C-DIR control software was developed before the release of the C++11 standard. There are several additions to the standard which would greatly reduce complexity, readability and maintainability of the source code. Future improvements to the software could include the use of smart pointers to create clear data ownership schema as well as reducing error prone raw pointer handling, and more extensive use of STL containers and algorithms to aid compactness to name a few. There were also areas in the code where strict adherence to coding standards could have been improved.

3 Characterising the C-DIR Device

3.1 Introduction

This chapter outlines the development of a testing framework used to calibrate individual components of the C-DIR device and ultimately characterise the performance of the C-DIR anode with respect to other imaging, photon-counting devices. The criteria against which performance was measured included, timing resolution, spatial resolution and data acquisition rates. Each section seeks to explain and justify the experimental setups and tools required to measure each performance metric and how the C-DIR compares with, or stands on each count with respect to, other approaches to position-sensitive photon detection.

3.1.1 C-DIR Hardware

The final product, which will be hereafter referred to as the C-DIR Camera, consists of a Photek PMT225 25mm photomultiplier tube with 2 chevron-stacked microchannel plates and a resistive sea rear coupling anode, C-DIR anode with NINO ASIC which represents the position-sensitive charge readout, and finally the HPTDC which acts as the read-out electronics for the camera. The HPTDC is interfaced to a PC via USB 2.0 where the control software, developed in the previous chapter, reconstructs two-dimensional images from the four NINO output channels timing data. The C-DIR Camera is described in 1.5.

3.2 Time-Over-Threshold vs Charge Calibration

The ToT versus charge calibration described in Chapter 2 is the mechanism used for measuring anode charge and thus charge centroids. This section addresses how this information is obtained by describing the experimental setups which were

used to probe the NINO response to input charge and discussing the limitations of the approaches used.

3.2.1 Delay Generator Automation

A Stanford Research Systems DG645 delay generator was used as the charge and clock source for all attempts to obtain a pulse width vs charge calibration. Automatic synchronization of the charge selection and data collection presented a useful feature to reduce the amount of tediousness associated with collecting fine-grained response to charge for the NINO ASIC. Therefore, a calibration routine was added to the data acquisition software.

The DG645 device is shipped with a light-weight C interface which can be used to communicate with the device over TCP/IP protocol. This required a physical Ethernet connection between the DG645 and the controlling PC. Figure 3.2-1 shows

```
class DG645{
public:
     _declspec(dllexport)DG645(char *ip);
     _declspec(dllexport)~DG645();

     _declspec(dllexport) void sendCommand(char *command);
     _declspec(dllexport) void readCommand(char *buffer, unsigned num);
     _declspec(dllexport) void disconnect();
};
```

Figure 3.2-1 DG645 C++ Device public interface. The constructor initialises a connection to the supplied IP address after which public methods are used to send/receive commands or disconnect from the device.

the custom-made C++ around the DG645 interface. The device was connected to IP address 169.254.31.31 and controlled using the ***lamp n, v*** command. This command is responsible for adjusting the output voltage on each of the signal channels, *n* is the channel ID and *v* is a floating point (real) number corresponding to the voltage. The DG645 allowed a range of 0.5 to 5V in 0.01V increments.

The calibration routine code was embedded in the source component and enabled/disabled using a compile time switch. When enabled, this allowed acquisition of timing data to be synchronized with changes in the charge supplied by the delay generator. A small delay was introduced between each voltage change to allow the timing data to stabilize before it was collected and saved to disk.

3.2.2 ToT vs Voltage Data

Before discussing the actual mechanisms by which the calibration data was collected. It is useful to describe the data formats used for storing the data as well as how the actual look-up table was constructed. The calibration routine, described in the previous section, produced binary files which contained high stats for NINO lead time and pulse width at each voltage set point. The file naming convention was simply the voltage step where the times were recorded. If the calibration was configured to measure the pulse width response from 0.5-5V in steps of 0.02V, this produced 225 files for each of the NINO Channels. The number of data points collected was configurable, however the default was $4x10^5$ points. CPU intensive processing was abstracted away from the DG645 calibration routine to maximise data acquisition performance. The files were processed using a python routine making use of a host of mathematical and scientific tools. The mean of the pulse width values at each voltage point were recorded along with the voltage stored as 1-D arrays for processing by the SciPy fitting tools. The $scipy.interpolate.interp1d$ module for generation of the full look-up table. The $interp1d$ method produces an interpolation function from a set of fixed input data points and provides options for the order of the spline interpolation to be used. The third order (cubic) spline interpolation provided the best result for the pulse width vs charge data. Splines were chosen as opposed to polynomial fits since polynomials

tend to behave unpredictably outside of the fitting region, the idea was to extrapolate the spline beyond the measured data in addition to interpolating between data points. The look-up table was written out as a binary file for reading into the data reduction application.

Figure 3.2-2 provides an example of how closely the generated function can match

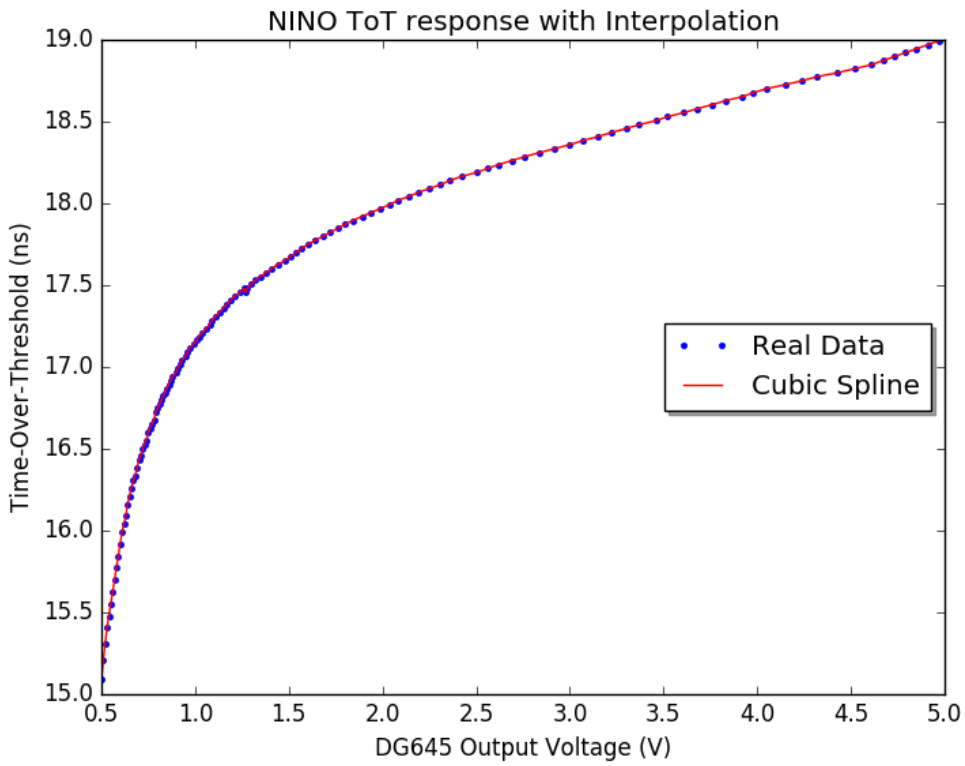

Figure 3.2-2 An example of using cubic spline interpolation on a set of sample data taken from the charge response of a single NINO channel. The cubic spline interpolation matches the data perfectly.

the real data. The code used to generate this plot is shown in Figure 3.2-3.

```
## importing necessary libraries

reader = csv.reader(open("C:/Users/Lamar/Desktop/pulseWidthCalib0.csv", "rb"),
delimiter=",")
x = list(reader)
result = numpy.array(x).astype("float")

chg = result[:,0]
pw = result[:,1]

pw = pw * (25.0/1024.0)

f = interp.interp1d(chg, pw, kind="cubic")

## plotting
```

Figure 3.2-3 Simple coding example for generating spline interpolation using SciPy.

The look-up table generated used voltage instead of charge. Since there is a linear relationship between voltage and charge shown in equation 3.2-1 knowledge of the exact charge was not critical for imaging. This can be proven by revisiting the C-DIR imaging equations1.5-1, 1.5-2 and 2.2-5 and substituting the charge law:

$$\boldsymbol{Q_i = C_i V_i} \qquad \textbf{3.2-1}$$

The assumption made here is that the capacitance on the NINO channels vary negligibly so that any differences can be ignored. If each capacitance is treated as the same, then:

$$\boldsymbol{C = C_A = C_B = C_C = C_D} \qquad \textbf{3.2-2}$$

so that:

$$\boldsymbol{\frac{Q}{C} = V_A + V_B + V_C + V_D} \qquad \textbf{3.2-3}$$

$$\mathbf{x = V_A + V_B / V} \qquad \textbf{3.2-4}$$

$$\boldsymbol{y = V_A + V_D / V} \qquad \textbf{3.2-5}$$

Therefore, we can ignore the actual charge and instead use the input voltage directly for imaging. This approximation seemed to work well for the generated images.

3.2.3 MCP Charge Injection

The first approach to creating the pulse width against charge calibration for the NINO involved the direct injection of a known charge into the PMT microchannel plate. The idea here was to test the full camera system in place to produce a calibration which would be as close to reality as possible. Figure 3.2-4 shows the initial setup for these measurements. The camera system was mounted in

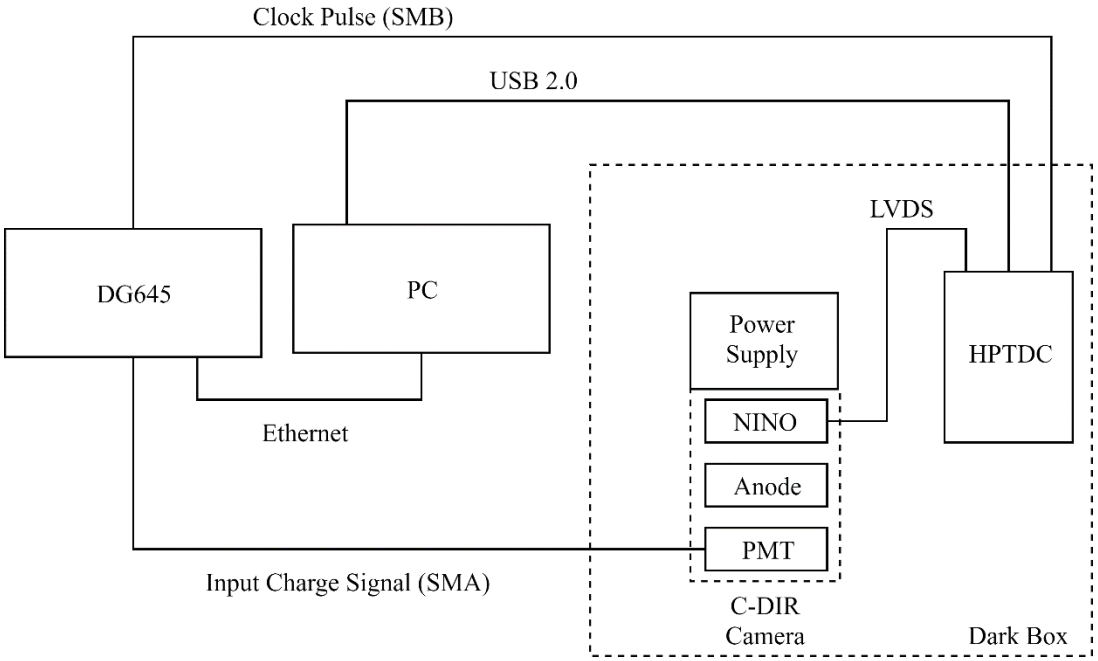

Figure 3.2-4 Initial setup for pulse width vs charge calibration using a DG645 delay generator to supply a known charge directly to the PMT.

a Photek DB2 Dark Box which contained SMA, SMB, USB 2.0 and mains power feed-throughs. This precaution was necessary since the PMT needed to be run at high voltage and thus high gain to create a measurable charge on the C-DIR anode. 20dB attenuators were used to limit the output of the delay generator as an extra precaution as well to reduce the point at which the NINO channels became saturated with charge during measurements. This attenuation also serves to maximise resolution within the linear region of the NINO response to input charge. Chapter 1

described this linear relationship for small input charge which is also shown in Figure 3.2-2.

3.2.4 Principle of Operation

A single channel on the delay generator was used to produce a stimulation pulse for the MCP. The DG645 output 40MHz clock was used as the input clock signal for

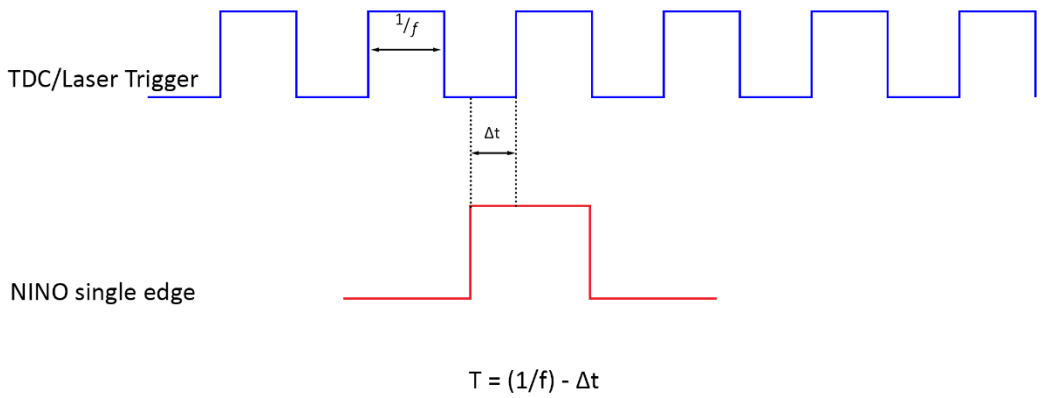

Figure 3.2-5 The timing mechanism of the TDC when triggered by the laser. The time interval between the NINO rising edge and the clock rising edge to follow, Δt, is subtracted from the trigger period $^{1}/_{f}$ to give the arrival time.

the HPTDC. The HPTDC timing mechanism is shown in Figure 3.2-5. Each edge signal arising from the NINO, leading or trailing, is measured with respect to the TDC clock in a similar scheme to that used in Figure 1.2-4. Since the TDC itself is triggered by the excitation source, the timing calculation is simplified. The time interval between the NINO pulse leading edge and the clock leading edge is subtracted from the trigger period to provide the pulse arrival time. This is performed for both leading and trailing edge outputs of the TOT discriminator for each NINO channel. The leading edge provides the TCSPC time histogram and the interval between leading and trailing gives pulse width which can be used to recover charge. The charge injection channel on the DG645 was set to 100KHz which was safely within the maximum theoretical count rate. With the tube high voltage power

supply set to an operating voltage of 1.98KV, corresponding to a gain of ~10^6, the control software was used to acquire the pulse width vs charge data as described above in the previous section.

3.2.5 Results

Due to the photomultiplier tube construction, direct charge injection into the MCP was the wrong method for generating the charge calibrations. This effect was due to a large, 1 kΩ resistance between the MCP input and ground which produced spurious charge events within the system in the form of ringing. The noise had a period of about 20KHz. This ultimately led to a heavily distorted, unexpected calibration. The effect became more noticeable as the voltage was increased as.

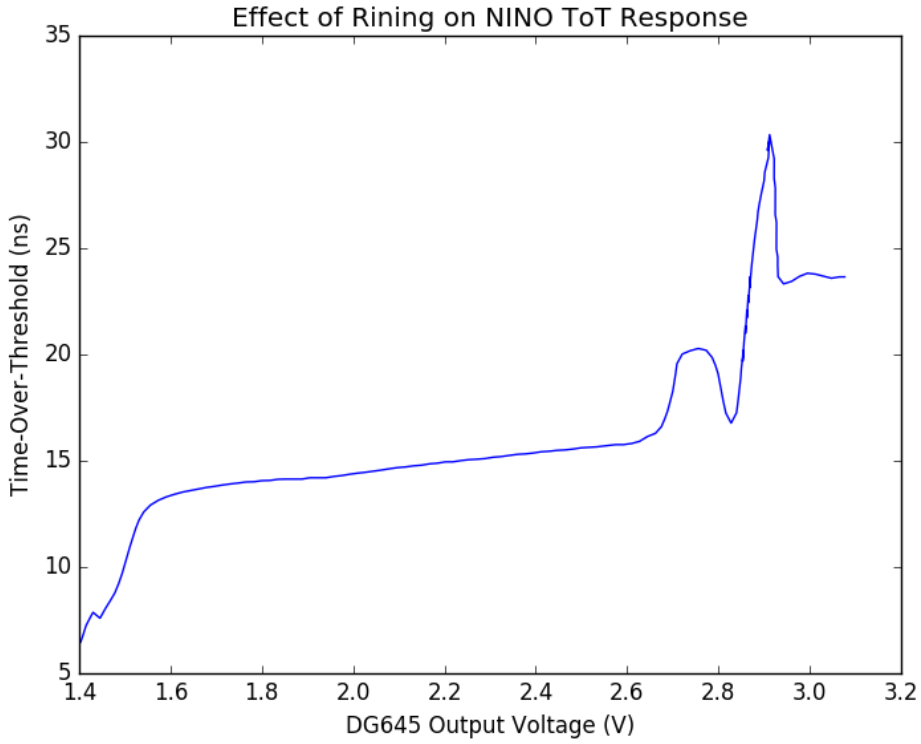

Figure 3.2-6 Effect of MCP charge injection on NINO response. As the voltage/charge increases, the effect of the ringing becomes more pronounced until the calibration is overcome by noise.

shown in Figure 3.2-6. The method used to stimulate the NINO was re-designed to avoid the effects of this feedback loop.

3.3 Issues with the ToT Calibration

3.3.1 Threshold Configuration and Drift

One of the unfortunate features of the NINO discriminator is the turn-pot mechanism for setting the threshold level. The threshold level was configurable to be between ~69mV-270mV and the availability of read-out pins on the ASIC facilitated using a standard digital multi-meter for measuring the set threshold level. However, this threshold was subject to drift by about 5mV over a 24-hour period. Configuring the threshold was somewhat of a black art because there is a trade-off between sensitivity and noise which required careful and thoughtful exploitation. Lower threshold values increased sensitivity, therefore the photomultiplier could be operated at lower gain. However, this increased overall noise sensitivity, particularly the PMT dark noise. Increasing the threshold meant the PMT could be operated at higher gain and whilst reducing susceptibility to noise, but this resulted in the loss of valid lower energy photon events. These considerations coupled with a drifting threshold meant that every experimental phase required a re-calibration of the charge response since changing the threshold effectively invalidated the pulse-width vs charge measurement (Figure 3.3-1).

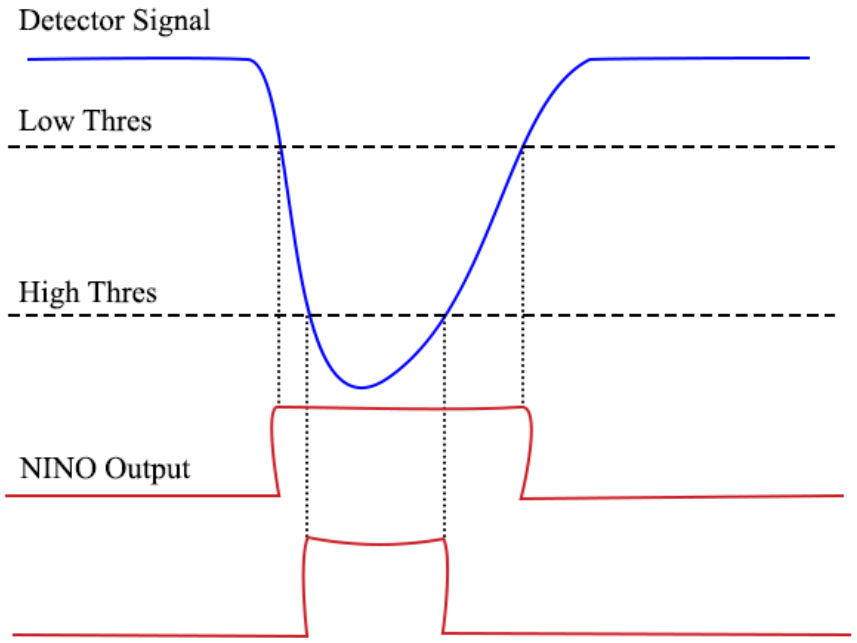

Figure 3.3-1 The effect of modifying the NINO threshold on pulse-width measurement. Increasing or decreasing threshold will require a new calibration for ToT vs Charge.

3.3.2 DG645 Dynamic Range

While collecting the ToT vs Charge calibration data, it was noted that different levels of attenuation shifted areas of the NINO response being sampled. This is illustrated in Figure 3.3-2. This pointed to a limitation in the DG645, specifically,

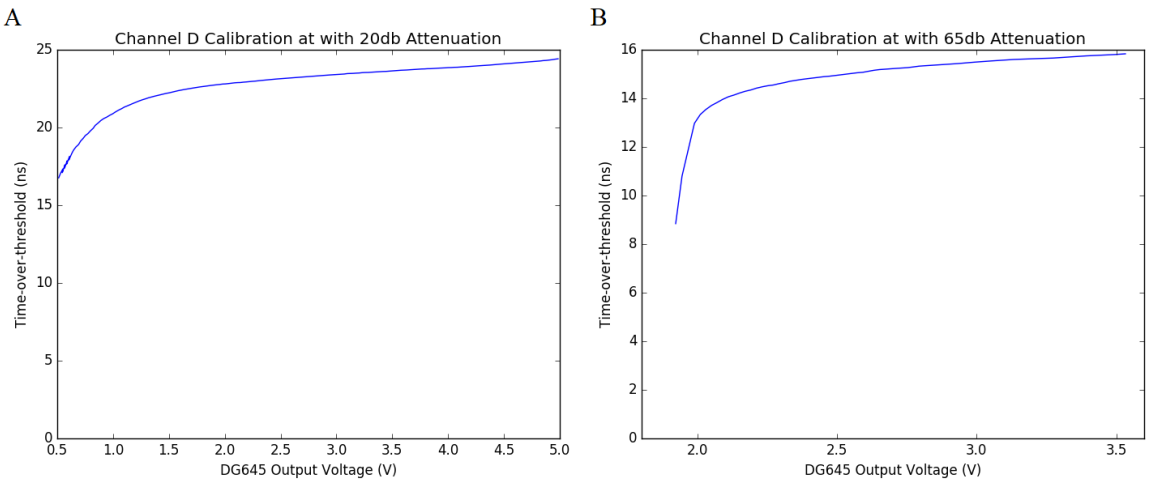

Figure 3.3-2 Shows the different areas of the NINO response sampled at A) 20db and B) 65db input signal attenuation.

the charge supplied by the DG645 was not broad enough to cover the full dynamic range of the NINO response. In addition to this, the voltage steps were not fine-grained enough to fully exploit the linear portion of the response. Efforts to combine various attenuated datasets resulted in rubbish calibrations as shown in Figure 3.3-3

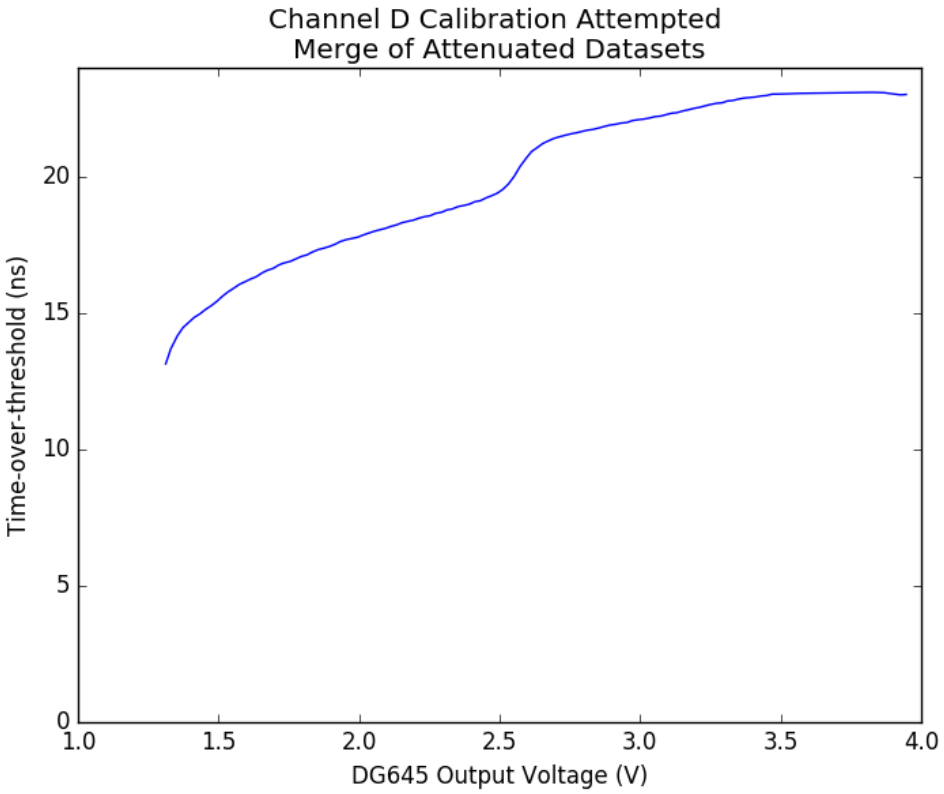

Figure 3.3-3 Attempt to combine various attenuated datasets result in warped impracticable calibrations.

Since there was no other hardware available for generating charges, this was a limitation which was accepted. All calibrations were taken with a single attenuation value of 30db with respect to the DG645 output signal.

3.3.3 Noise

Section 3.2.3 briefly discussed the effect of noise on the NINO calibration. The section to follow will discuss how noise on the NINO channels affects image

distortion. The effect of high-voltage noise on the system, however, was discovered before any attempt at imaging using the C-DIR. The initial experimental set-up for the C-DIR did not contain any high-voltage shielding between the PMT, PMT power-supply, the supply cables and the NINO which resulted in noisy data.

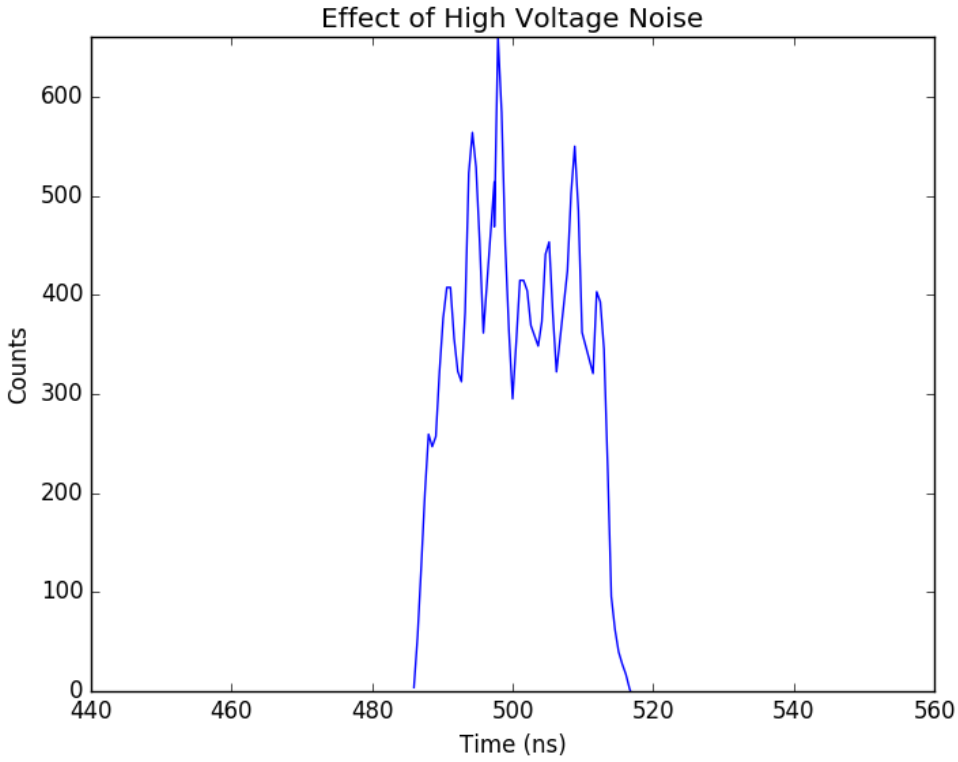

Figure 3.3-4 Effect of high-voltage noise on timing data for a single NINO Channel. Data was collected using a laser pulse generator (LPG) with 40ps width at 650nm. Notice the breadth of the timing response ~30ns. (Arbitrary t_0)

Figure 3.3-4 shows the effect of high-voltage noise on the timing data for a single NINO channel. This data was collected without the presence of high-voltage shielding and shows a very broad timing response, on the order of tens of nanoseconds, for an input laser pulse with a width of 40ps. This represents an extremely poor timing resolution. The high-voltage noise being responsible for the broadening of the time response.

The simplest approach to reducing high voltage noise was to isolate the high-voltage power supply from the C-DIR camera using shield enclosures. Off-the-shelf aluminium alloy enclosures (RS IP5 Diecast) were chosen due to their rated resistance to electro-magnetic/radio-frequency (EMI/RFI) interference. The enclosures were provided in varying sizes which allowed matching of sizes of the system components without large amounts of dead-space. In addition to using EMI/RFI resistant shielding, high-voltage interfaces were machined through the housing to make use of shielded cabling for conveying the power supply charge. Figure 3.3-5 shows the basic design of the C-DIR camera and power supply

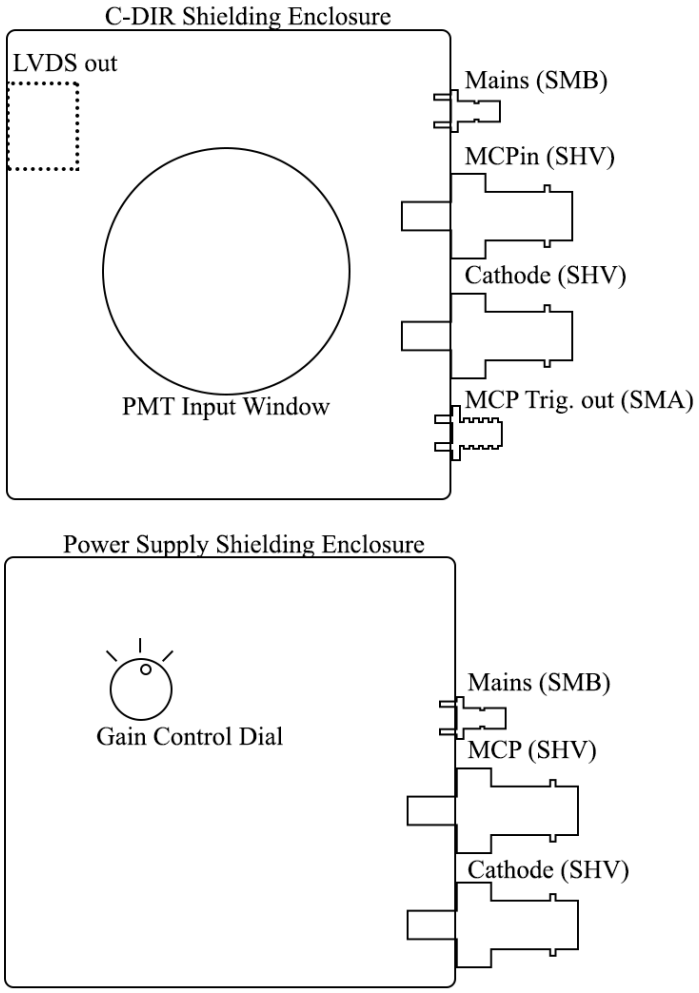

Figure 3.3-5 Basic design of the C-DIR and corresponding power supply shielding boxes. Input low voltage mains charge is conveyed using BNC connectors while high voltage charge is conveyed using SHV.

Enclosures. SHV (safe high voltage) connecters and cabling are used to transport the large cathode and MCP voltages (you may need to describe operating voltages). SHV was chosen since they were designed for use in high voltage application up to 5Kv and 5amps which exceeds the MCP and cathode potential required to operate the PMT at high gain. The SMB (SubMiniature version B) connectors are used for conveying smaller input voltage from the 12V mains power supply. The SMA connector is used to transmit the MCP trigger signal to the TDC device for TCSPC as described in 3.2.4. Introducing this simple design for shielding the camera from the effects of high-

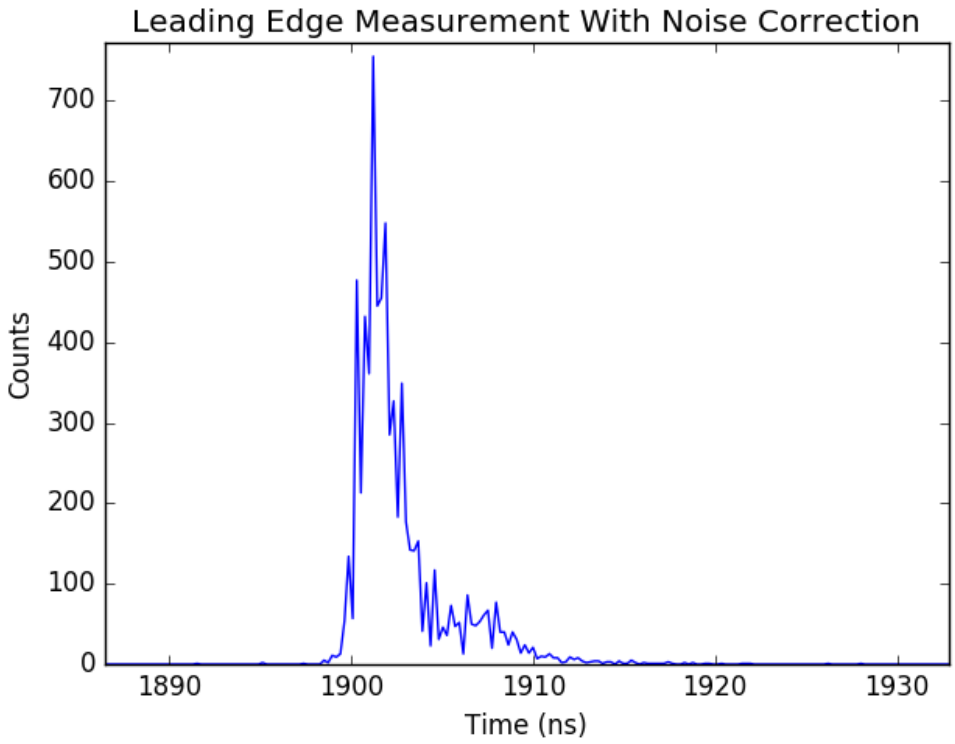

Figure 3.3-6 After noise correction the laser pulse shape becomes more prominent. The FWHM of the peak is ~180ps which is better than an order of magnitude improvement.

voltage noise yielded dramatic improvements in timing performance as shown in Figure 3.3-6. Features in the input laser pulse became more apparent as timing performance increased by approximately an order of magnitude.

3.3.4 NINO Direct Charge Injection

This section described work carried out with the help of Thomas Conneely aided in the development of a series of prototype PCBs which were interfaced with the NINO for direct charge injection in an attempt to address the shortcomings identified in the previous section. This was necessary since specialist knowledge/training on the use of PCB design tools, CNC machines and chemicals involved in PCB development was required. Figure 3.3-7 shows the design of the charge injection board. There are 8 conductive pads, 4 on each side, while the

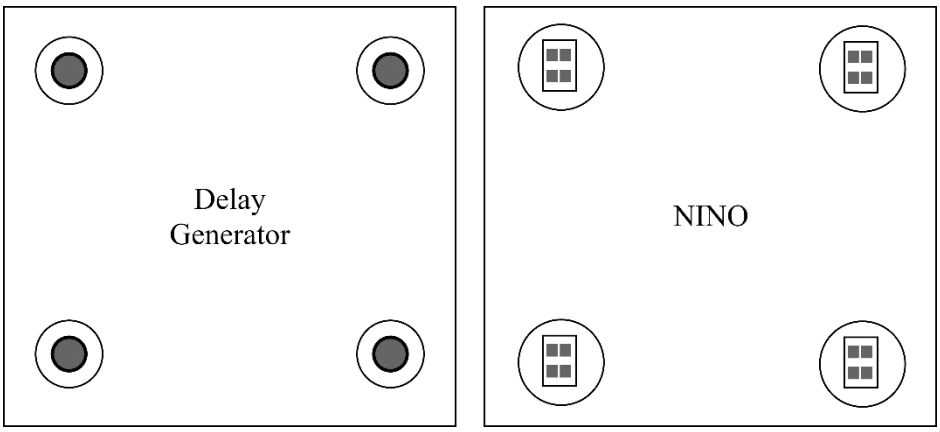

Figure 3.3-7 Either side of the charge injection board. Most of the board is bare except for the 8 conducting interface pads which allow charge to be transferred capacitively through the PCB. The top side contains 4 SMA female pins which interface with the DG645 to accept the charge signal. The underside contains four female connectors which match the NINO acceptance male pins.

remainder of the board surface is non-conducting. Charge is transferred from one side of the board to the next capacitively. The top side of the board contains 4 SMA connectors which interface with the DG645 to deliver charge to the board. The underside contains 4 special female connectors which interface to the NINO board. Therefore, the PMT and capacitive division anode were completely bypassed. Several iterations of the board were developed varying the pad sizes on the side which interfaces with the DG645 to obtain an optimal capacitive coupling between the input charge from the DG645 and the NINO. This was more convenient than

attempting to solder several surface mount capacitors which would be prone to error and potential damage to the PCB. Figure 3.3-8 shows the modified setup which no

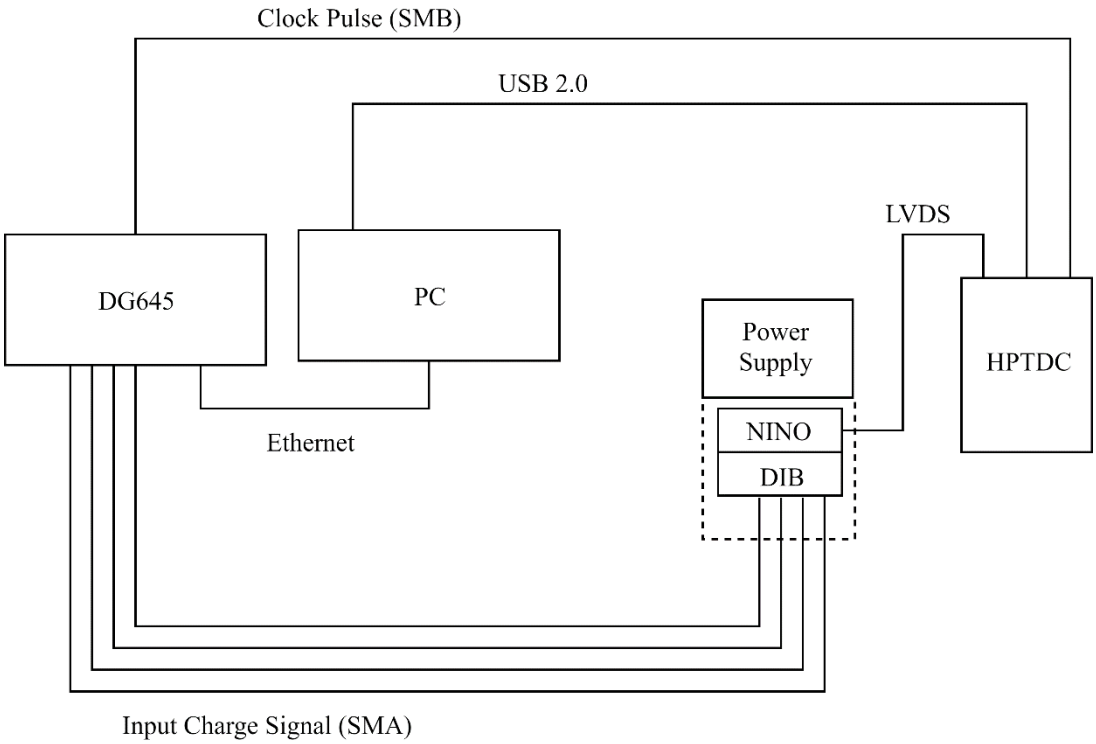

Figure 3.3-8 Experimental setup using the direct injection board (DIB in the diagram). Since the PMT/Anode combination were no longer in use, the setup was removed from the dark box.

longer required a dark box. This new setup also allowed each channel of the NINO to be controlled independently reducing cross-talk between channels when measuring the charge response. The result of this is shown in Figure 3.3-9.

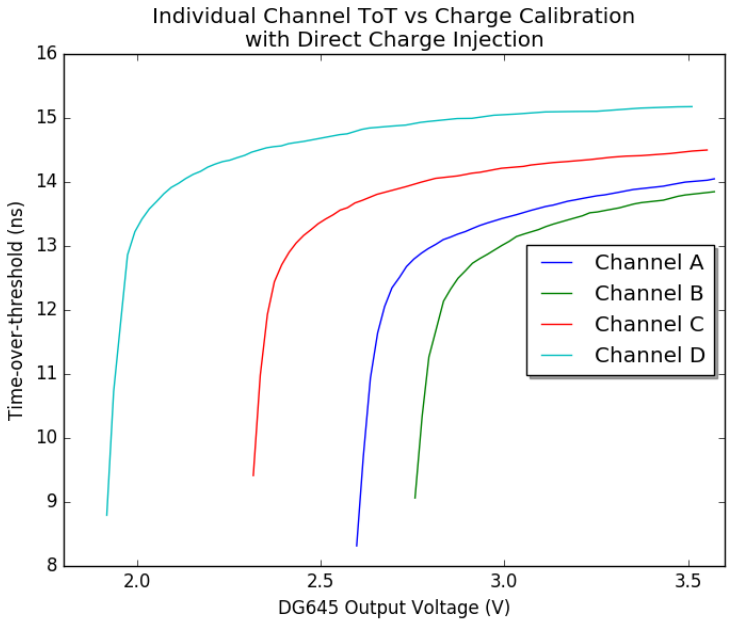

Figure 3.3-9 Resulting calibration when each NINO channel is probed separately. This calibration was not used since it did not represent real operating conditions.

However, it was felt that this was unrealistic since the C-DIR anode would be outputting charge on all four anodes simultaneously so any calibrations should be as close to reality as possible. The NINO response observed was more consistent with what was expected based on the literature. Figure 3.3-10 below shows the

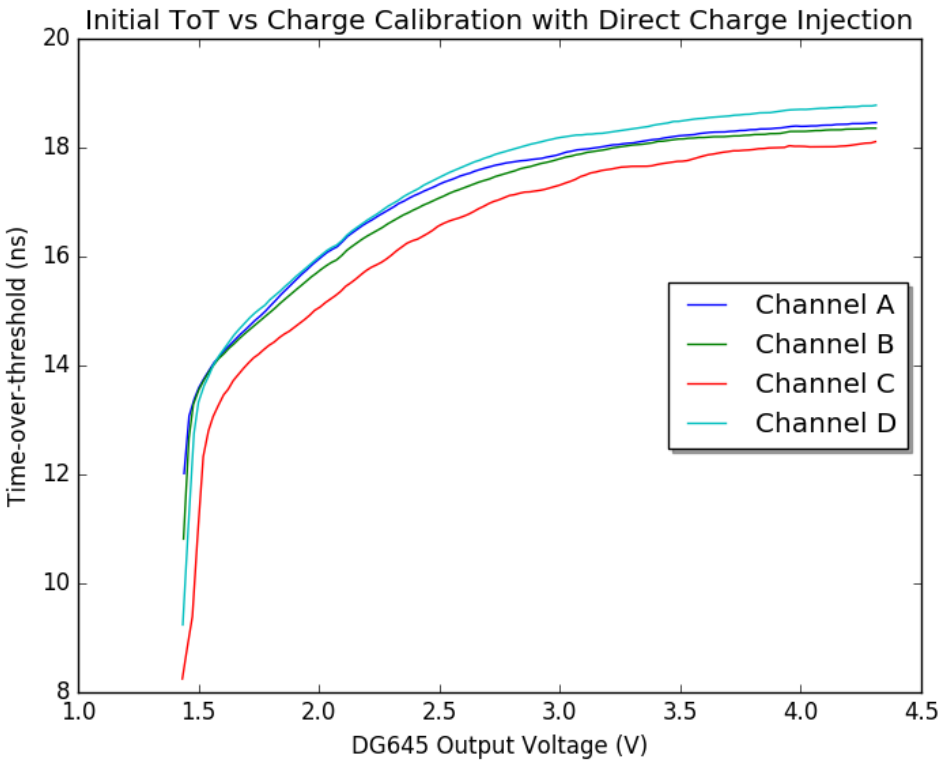

Figure 3.3-10 Initial Tot calibration with charge injection board shows marked improvement in noise compared to the MCP injection approach.

improvement in NINO response. This calibration was the first of many taken using this approach.

3.4 Imaging and Distortion Correction

3.4.1 Preliminary Imaging

The basic set-up for imaging is as shown in Figure 3.4-1. This initial set-up was

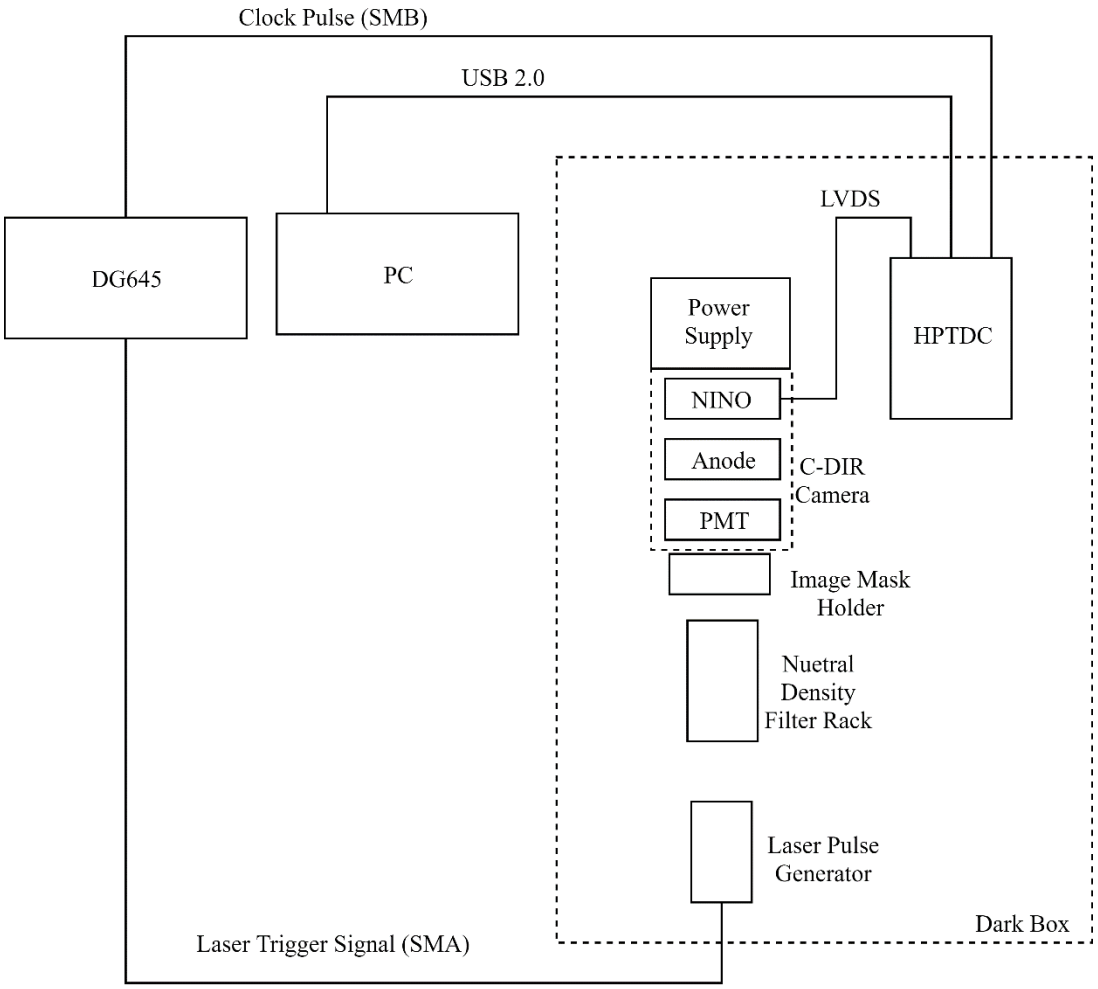

Figure 3.4-1 Setup for basic imaging using masks. A laser pulse generator is used as the collimated light source controlled by a DG645 delay generator. The mask is directly coupled to the input window of the PMT using an optical mount to hold it in place. ND filters are used to attenuate laser power and act as a precaution to protect the highly sensitive PMT.

used to provide a qualitative view of the images produced by various ToT/Charge calibrations. Figure 3.4-2 shows the initial pinhole mask used to investigate potential imaging non-linearity in the C-DIR camera. At this stage, there was clearly a large amount of distortion present in the system which appeared to be a mixture of pin-cushion and barrel distortion. Several theories

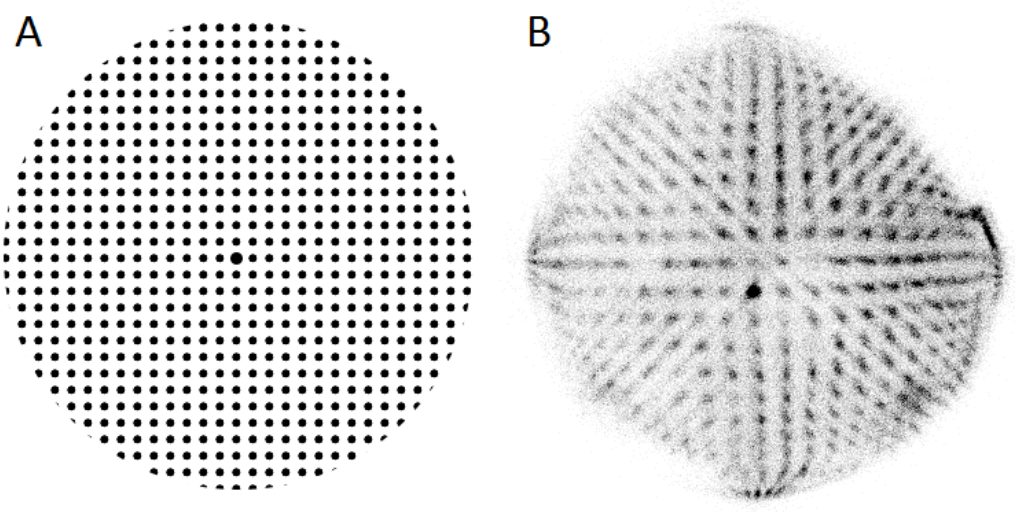

Figure 3.4-2 A) Illustration of pinhole mask used to determine the imaging non-linearity of the CDIR. The mask contained 5µm pinholes on a 25mm diameter grid. The centre pinhole is 10µm in diameter. of B) Resulting image produced imaging system showing pin-cushion distortion.

were proposed to describe the origin of this distortion. The first hypothesis was noise on the NINO channels. However, after developing the shielding enclosures, described in 3.3.3, calibrations stabilized at fixed thresholds. The only other sensible explanation to explain the distortion was irregularities in the physical anode capacitive pads. There was no scope, or budget, for optimising the anode geometry therefore multiple solutions were developed to correct the distortion in software.

3.4.2 Distortion Correction using Geometric Transformations

The basic idea of this approach was to scan a point source over the surface of the detector sweeping in X for fixed positions of Y and then sweeping in Y for fixed positions in X. Known positions in space would be compared to those measured by the C-DIR anode and a 2-D geometric transformation would be created which transforms from measured positions to the expected scan position. To achieve this, the C-DIR camera was mounted on an XY motorised translation stage with the point source aligned to the centre of the photomultiplier input window Figure 3.4-3. This

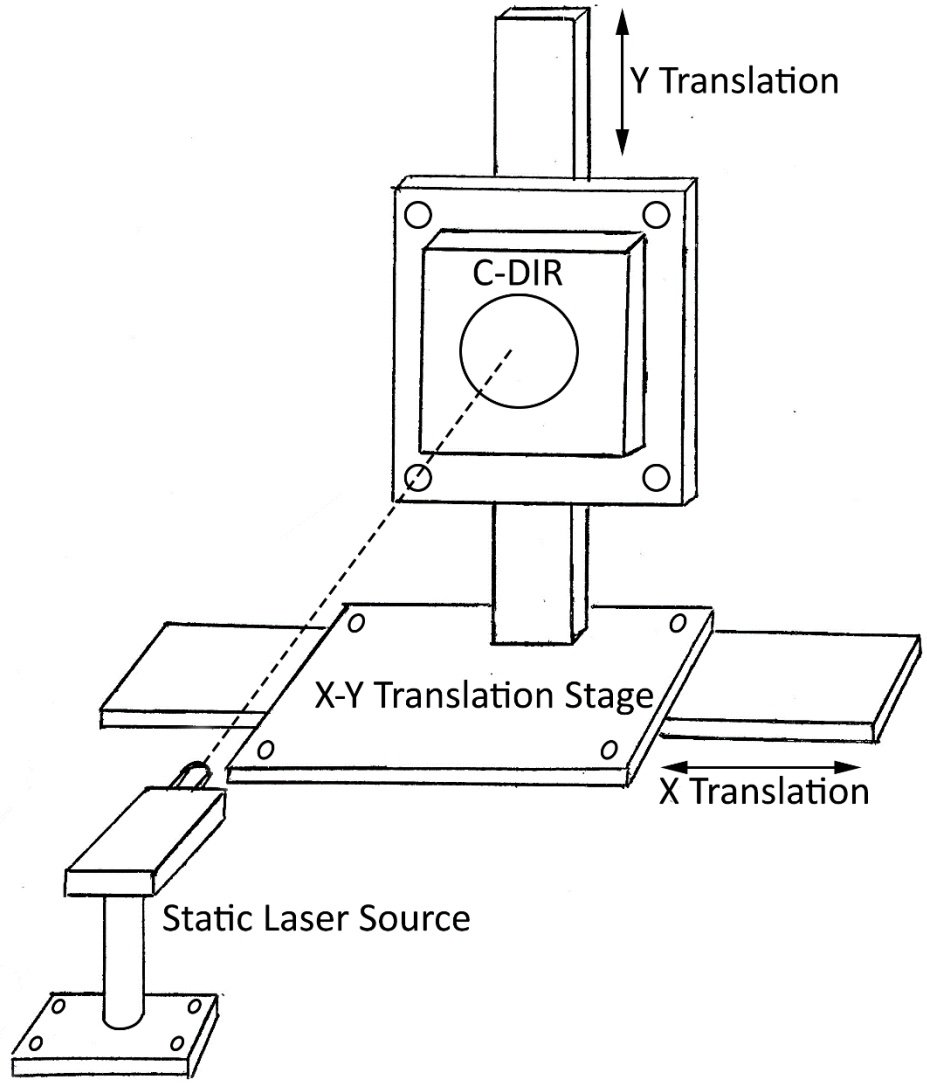

Figure 3.4-3 X-Y translation stage set-up for 2-D distortion correction. The laser point source is fixed and the C-DIR is scanned using the stage. Measured positions are compared to stage positions with (0,0) being the centre of the laser scan.

centre position is treated as the origin $(0, 0)$ and is the frame of reference for all subsequent measurements. A C++ library was written to automate the process of the scan and synchronise this with the C-DIR data collection for each point in the sweep. The program output the positions of the translation stage into a csv file while each point measured by the C-DIR was saved as a separate image. This was the preferred method since it facilitated calculation of the centre of mass of the spot more easily if all spots are separated. Figure 3.4-4 shows an example of a

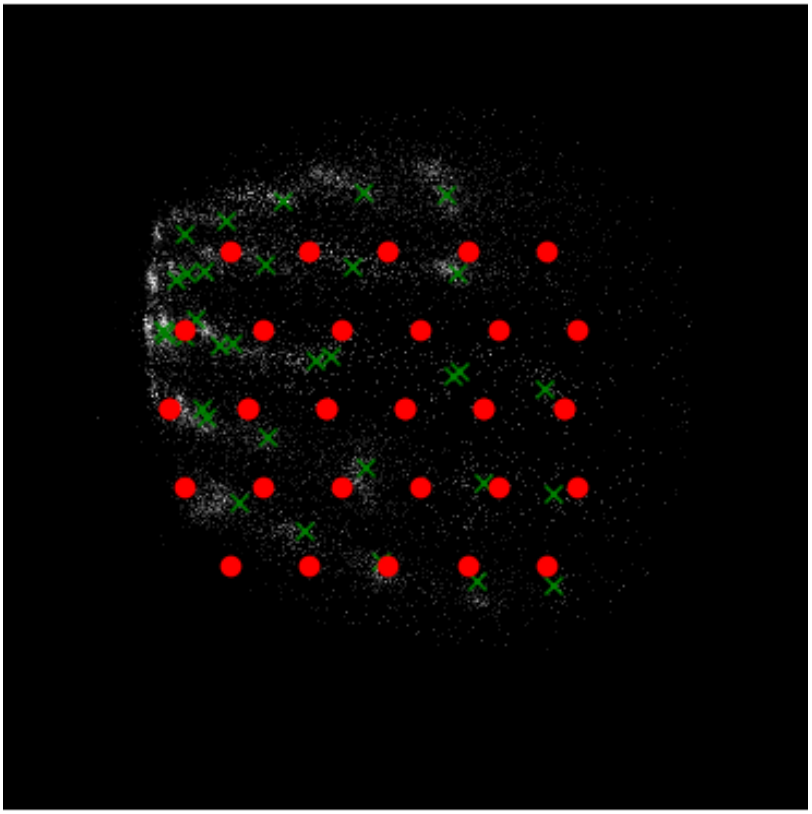

Figure 3.4-4 Stage scan of the detector with 28 discrete points. The green cross overlay represents the centre of mass calculation for each point which the red circle overlays show the actual stage positions. These were used as the basis for the 2d distortion correction.

composite of the surface scan of the C-DIR. The red dots overlaid onto the composite show the positions recorded by the translation stage. The green cross overlays show the centre of mass of each of the scanned points. A python script was developed in order to analyse the data scans and generate the 2D transformation. The high-level action of the script can be broken down into the following steps:

1. Load and store stage positions in a list.
2. Load each C-DIR position measurement and calculate the centre of mass of the spots. Using the scipy library.
3. Store the positions of the centre of mass in a list.
4. For the X sweeps. Generate a fit of (interpolate) X measurements x_m against stage positions (expected positions) x_e for each Y step and store coefficients.

5. Generate a fit for each coefficient with respect to Y steps so to have a continuous range of coefficients through Y and store these new coefficients.
6. Repeat steps 4 and 5 for Y sweeps.
7. Use the coefficients generated in 5 and 6 to correct a distorted image.

There were two approached to interpolating the relationship between measured and expected positions. The first attempt involved using a polynomial fit where:

$$x_e = c_0 + c_1 x_m + c_2 {x_m}^2 \ldots + c_n {x_m}^n$$

where x_e is our expected or corrected position, x_m is our measured position, c_i are our coefficients and n is the degree of our polynomial. The $numpy$ library in python provided a convenient method, via the $numpy.polyfit$ module, of performing a least-squares polynomial fit. Figure 3.4-5 shows the result of the polynomial fit

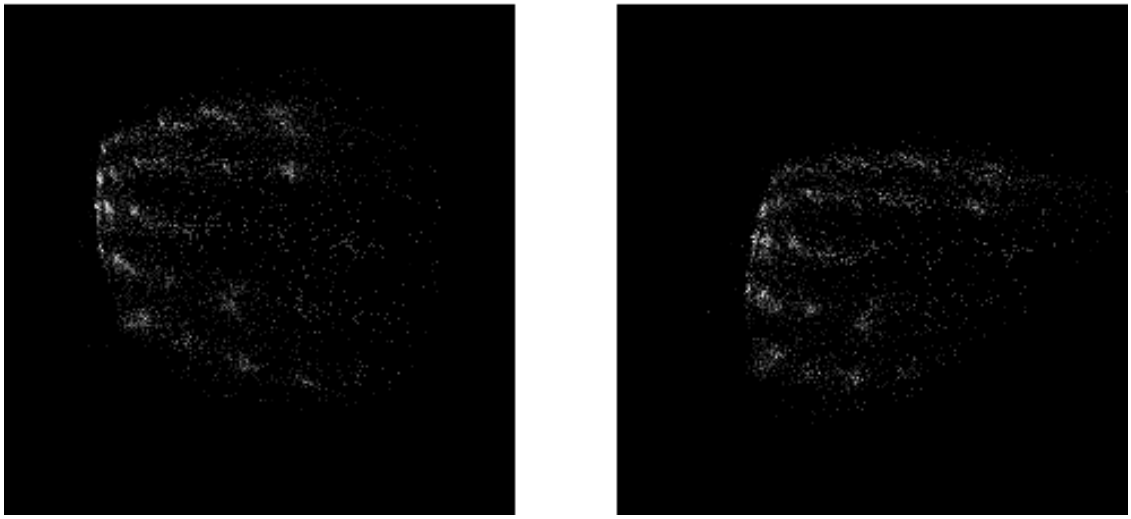

Figure 3.4-5 The image on the left shows the original scan of the detector surface. The image on the right shows the correction using a polynomial fit. Since the degree of the polynomial used for the correction $n = 1$, this was essentially a linear fit. Higher degrees resulted in large amounts of artefacts.

correction. The degree of the polynomial was chosen as $n = 1$ which obtained the best result. This degree was also used for interpolating the coefficients as well. Using higher values of n resulted in worsening of the distortion. This occurred since

the polynomial fit only works well within the fitting region. Outside this region the polynomials tend to behave unpredictably.

The limitations of the polynomial approach to fitting led to the use b-spline interpolation. This was available in the python $scipy$ module. The $scipy.splrep$ function finds a b-spline approximation of a 1-D curve, $x_m \; vs \; x_e$, and returns a tuple representing the b-spline. This can be used in the $scipy.splev$ function to evaluate the spline for a given input, which in our case was our X measurements. These methods were convenient because they allowed the use of the same steps for interpolating the spline coefficients in the same was as the polynomial coefficients. The resulting correction is shown in Figure 3.4-6. Once again, the degree of the

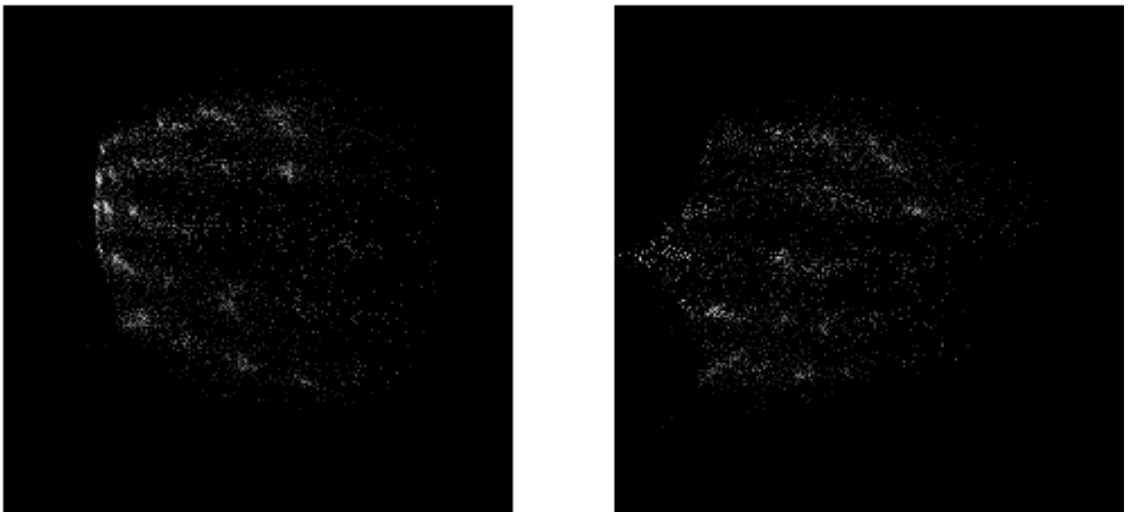

Figure 3.4-6 The image on the left shows the original scan of the detector surface. The image on the right shows the correction using a spline fit. The degree of the spline $n = 1$ for this correction. The horizontal correction shows some artefacts while the vertical correction appeared to be better than the polynomial correction.

spline was chosen to be $n = 1$ which seemed to produce the best fit, especially horizontally, with the least number of artefacts. One may notice that the correction was performed on the original scan as opposed to a distorted image collected using the C-DIR. This is done for two reasons. Firstly, it is easy to see how the spots measured by the C-DIR are warped into a reasonably straight configuration as would

be suggested by the translation stage scan positions as seen in Figure 3.4-4. Secondly, this approach was abandoned shortly after developing this correction mechanism in favour of the Brown-Conrady approach which is described in the proceeding section. This was due, at the time, to drifting ToT vs charge calibrations which resulted in unpredictable image distortion. Therefore, this method would have to be employed before every experiment to correctly remove image distortion. This did not seem like a workable solution. Also, the evaluation of the b-spline and correction of the measured position was on the order of 10s of seconds and minutes in some cases. This was not suitable for live data collection which made this method impracticable. A compromise between speed and distortion reduction was required and this was met using the Brown-Conrady approach.

3.4.3 Brown-Conrady Distortion Correction

After several attempts to stabilise the ToT vs charge calibration as well as intrinsic image distortion, we were able to achieve imaging which appeared to suffer mostly from pin-cushion distortion as outlined in 3.3. This meant the C-DIR was now a good candidate for a simpler means of distortion correction, namely, the Brown-Conrady approach which was described in 2.3.5. A distortion mask for the C-DIR was created by engineering a 2-D pinhole mask on PCB with a CNC machine. Figure 3.4-7 shows how the original pinhole arrangement is altered by distortion

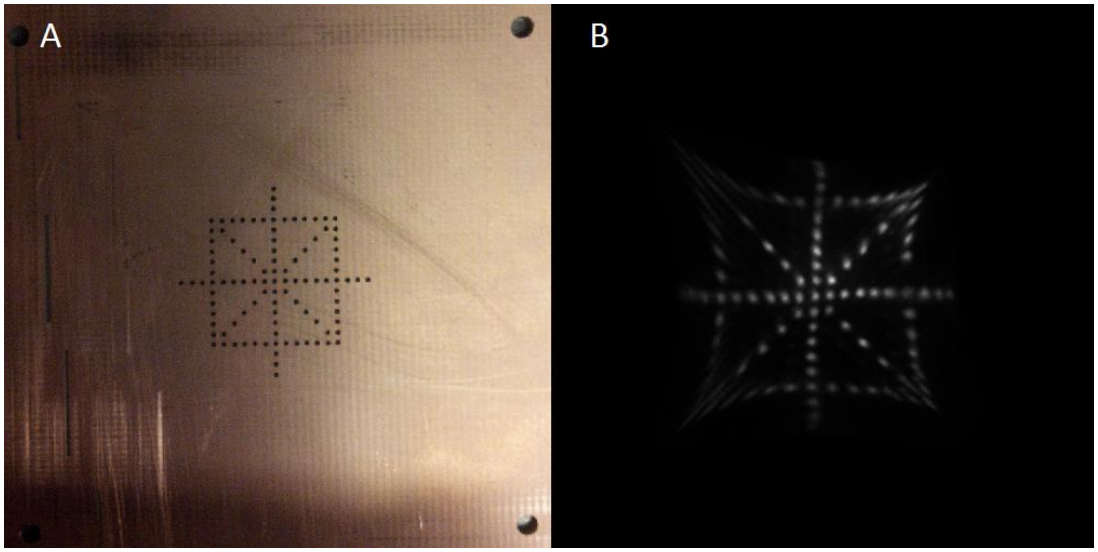

Figure 3.4-7 A) Pinhole cross-hair mask engineered using PCB in a CNC Machine. B) Resulting distortion image produced by the C-DIR.

in the C-DIR. Once, this distortion image was obtained, the software correction which was previously described in equations 2.3-2 to 2.3-4 was applied. Reducing these polynomials to two terms, i.e. K_i where $i \in (1,2)$, ignoring any tangential distortion contribution (P_i) and setting $K_1 = -1^{-5},\ K_2 = 3^{-11}$ yields the correction shown in Figure 3.4-8. Even with a very crude estimate for these components,

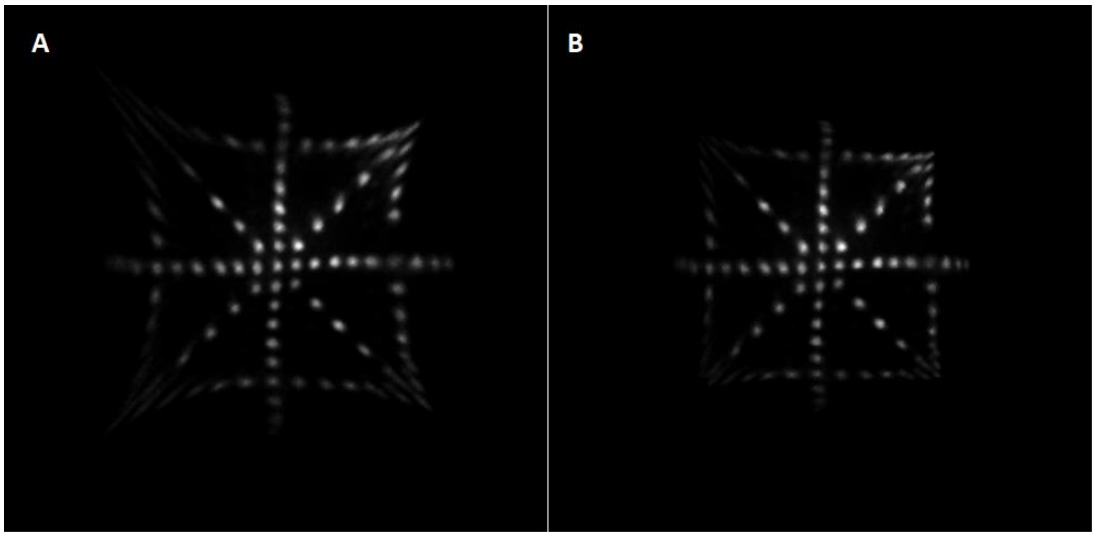

Figure 3.4-8 Example of moderate software correction using the Brown-Conrady distortion model. Here the radial distortion coefficients were adjusted to produce the best result with $K_1 = -1^{-5}, K_2 = 3^{-11}$. Tangential distortion contributions were ignored.

virtually all of the pin cushion distortion was removed. This distortion correction was on the order of tens of milliseconds which made it an attractive option for introducing as part of the live data collection process.

3.4.4 Resolution

The resolving capacity of the C-DIR camera was measured using a standard USAF resolution chart measurement in line-pairs per millimetre. The mask was projected onto the PMT input window using our laser source. Figure 3.4-9 shows the test

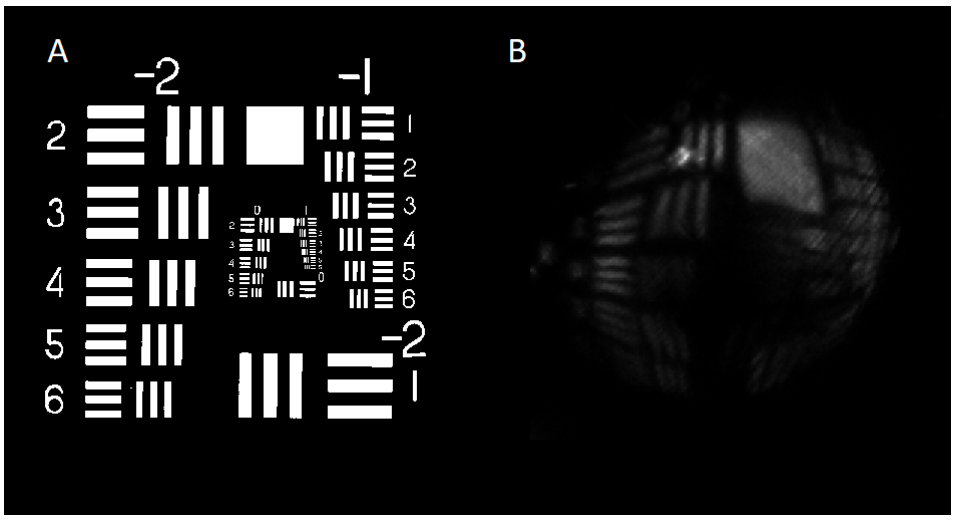

Figure 3.4-9 A) USAF Resolution test chart. Explanation of measurement in Table 3.4-1. B) Test chart image produced by the C-DIR. Here mostly larger groups are visible therefore resolution performance is poor.

chart image produced by the C-DIR vs a representation of the mask used to produce the image. This method of resolution measurement employs a simple reference table which can be used to determine the resolution of the imaging system, Table 3.4-1.

Table 3.4-1 USAF Resolution test chart measurement table. The element which is visible within a particular group has an associated resolution in line pairs per millimetre which is read directly from the table.

Group Number												
Element	-2	-1	0	1	2	3	4	5	6	7	8	9
1	0.250	0.500	1.00	2.00	4.00	8.00	16.0	32.0	64.0	128.0	256.0	512.0
2	0.281	0.561	1.12	2.24	4.49	8.98	17.96	35.9	71.8	143.7	287.4	574.7
3	0.315	0.630	1.26	2.52	5.04	10.08	20.16	40.3	80.6	161.3	322.5	645.1
4	0.354	0.707	1.41	2.83	5.66	11.31	22.63	45.3	90.5	181.0	362.0	724.1
5	0.397	0.794	1.69	3.17	6.35	12.70	25.40	50.8	101.6	203.2	406.4	812.7
6	0.445	0.891	1.78	3.56	7.13	14.25	28.51	57.0	114.0	228.1	456.1	912.3

The largest bar which cannot be differentiated by the C-DIR, group -1 element 1, determines the limiting resolution of 0.5 line pairs per millimetre (LP/mm).

3.4.5 NINO Input Impedance

The NINO ASIC contained a second turn-pot which allowed for tuning the input impedance. There were no read-out pins which facilitated an impedance measurement, however, the effect on imaging was qualified nonetheless.

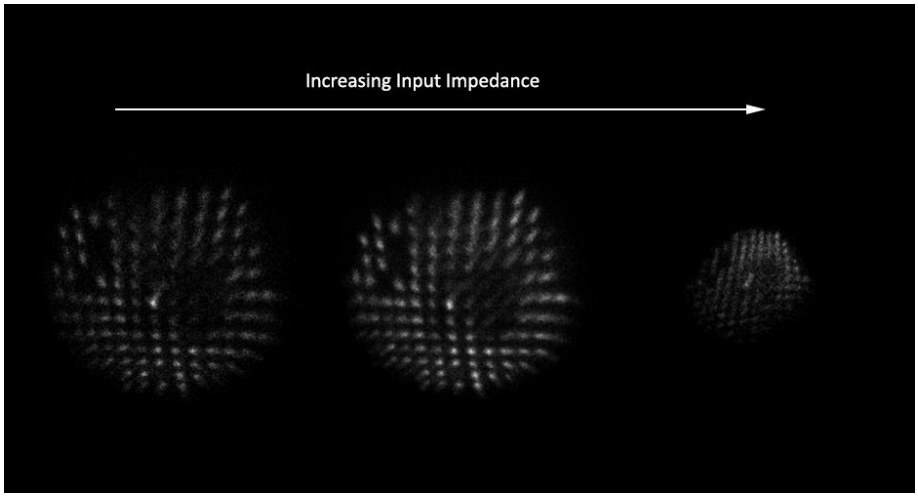

Figure 3.4-10 Shows the effects of increasing impedance on the output image. Since this attribute was not measurable, the midpoint of the impedance was set and remained unaltered for the remaining experiments.

3.5 Time-walk Correction and Timing Resolution

Although the ToT is useful in the context of imaging, this phenomenon has an adverse effect on timing accuracy. This is obvious since, the measured arrival time of a photon event is sensitive to the position of the threshold and the magnitude of the charge, even though the rise time of the detector pulses remain constant as shown in the previous chapter Figure 2.1-1. The time walk correction was designed to establish a linear relationship between the leading edge measurement and the corresponding ToT as seen in the literature [80]. This would allow for a convenient correction method of the form

$$\boldsymbol{t_{corr} = t_{meas} - f(ToT)} \quad \textbf{3.5-1}$$

where t_{corr} is the corrected time, t_{meas} is the original leading edge measurment and

$$\boldsymbol{f(ToT) = m \times ToT + c} \quad \textbf{3.5-2}$$

where ToT is the NINO pulse width which corresponds to the time measurement, and m and c represent linear correction factors which are obtained by creating a linear fit between the leading edge vs TOT relationship. Figure 3.5-1 A and B shows a sample dataset used to demonstrate how the time walk correction was obtained.

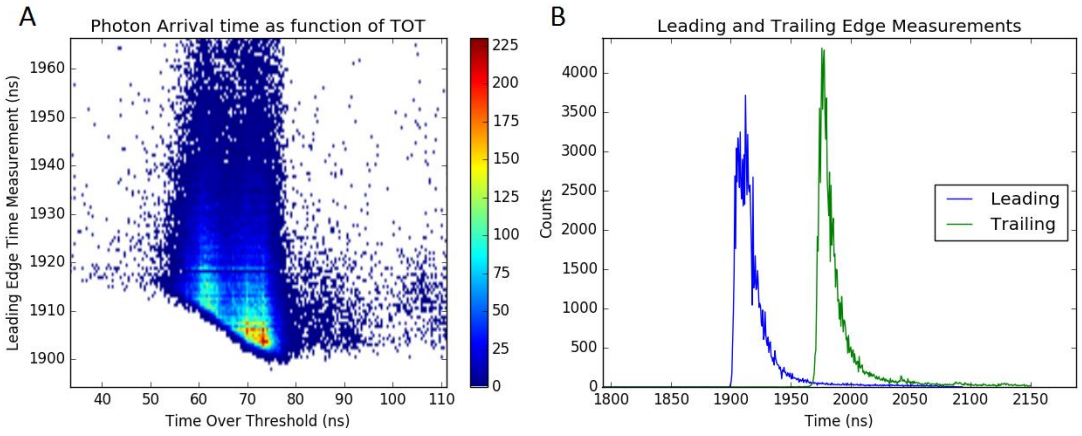

Figure 3.5-1 Timing data for a single NINO channel containing approximately 100K counts. A) 2D histogram of leading edge vs ToT. The ToT values are obtained by subtracting the leading-edge data from the trailing-edge data. B) Leading and trailing edge measurements which produce the relationship in A.

The above data was was collected using a drosophila (fruit fly) sample stained with green fluorescent protein (GFP). This dataset was chosen since it produced a wide distribution of leading-edge time versus ToT and contains ~100K counts.

Principal component analysis (PCA) was the approach used to establish a linear relationship between the leading edge measurement and ToT. This was chosen since it is a simple, yet powerful, method for finding linear relationships within data. This technique is normally used to reduce datasets with high dimensionality into much lower dimensions while preserving information [81]. In two dimensions, the technique can be used to find the axis along which there is most variation between our two variables pulse width and ToT. The NumPy and SciPy libraries once again provided useful tools for automating the treatment of collected timing data. Without going into the full mathematical basis of PCA, the following steps outline how the process of PCA can be broken down:

1. Standardisation of the data.
2. Calculation of the covariance matrix.

3. Calculation of the eigenvalues/eigenvectors from the covariance matrix.
4. Select the eigenvector corresponding to greater variance.
5. Transform the eigenvector by re-centering within the data.

The python script used to accomplished the linearisation is shown in Figure 3.5-2.

```
def PCA_linearise(x, y):
    x_std = standardise(x)
    y_std = standardise(y)
    data = numpy.array([x_std, y_std])
    cov = numpy.cov(data, rowvar=True)
    eigval, eigvec = eigh(cov)

    #select eigenvector which represents greatest variation along axis
    voi = eigvec[eigval.argmax()]
    voi[0] = (voi[0] * numpy.std(x)) + numpy.mean(x)
    voi[1] = (voi[1] * numpy.std(y)) + numpy.mean(y)
    gradient = (voi[1] - numpy.mean(y)) / (voi[0] - numpy.mean(x))
    y_intercept = voi[1] - (gradient * voi[0])
    return gradient, y_intercept
```

Figure 3.5-2 Python script which linearizes 2D data using PCA and returns a linear relationship based on the calculated eigenvectors.

The `standardise()` method subtracts the mean from the dataset and divides by the standard deviation thus producing data with zero mean and unity variance. The python NumPy module is then used to calculate the covariance matrix, while the SciPy linear algebra module is used to calculate the eigenvalues and eigenvectors. For a 2D dataset, two eigen values and eigen vectors are produced. The eigenvector, or principal component, which corresponds to the larger eigenvalue has more information about the distribution of the data and is therefore selected as the principal component to represent the linear relationship between the leading-edge measurement and the ToT. It is useful to note that the origin of the eigenvectors will be at $(0,0)$ after standardization, therefore we can use the mean of the datasets as (x_2, y_2) in the standard equation $m = y_2 - y_1/x_2 - x_1$. The selected eigenvector is

re-centered to the data using the initial mean and standard deviation. The gradient and y-intercept of this line are used as constants for correcting the data set as shown in equation 3.5-2. The resulting correction applied to the sample data is shown in

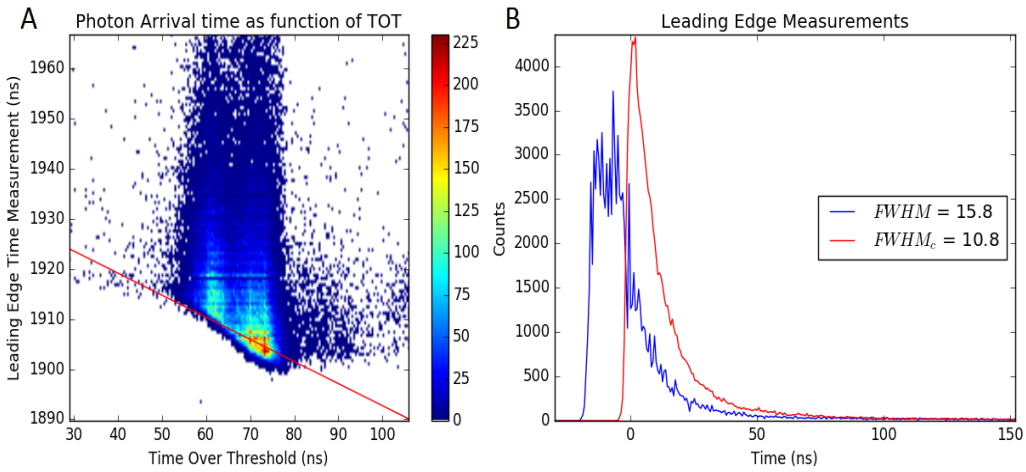

Figure 3.5-3 A) The data with the principal component (red line) which linearizes the relationship between the leading-edge measurement and ToT. The gradient and y-intercept of this line are used to correct the data. B) Time walk correction applied to the leading edge of our sample dataset from Figure 3.5-1. We see an improvement of ~30% in the timing resolution.

Figure 3.5-3 A and B. The time-walk correction has reduced the FWHM of the lead time measurement by 30% from 15.8ns to 10.8ns which represents a significant improvement to the timing resolution of the system. In practice, this technique is used to improve the timing resolution of the C-DIR by correcting the TTS and IRF which improved the perceived timing resolution limits of the system.

3.6 C-DIR Performance Evaluation

3.6.1 Timing Resolution

The C-DIR timing resolution is stated in terms of its impulse response or transit time spread (TTS). The transit time of a photo-electron is the time taken between conversion of the photon at the photocathode and its detection at the rear anode of a PMT. This timing is dependent on the trajectory taken through the PMT. A photo-electron which originates in one region of the photocathode may have several

trajectories through the PMT which will result in an uncertainty, or spread, around its arrival time. The TTS therefore represents the error in our measurement of the arrival time of photoelectrons and is the limiting factor on the timing resolution of the system.

The C-DIR detector makes use of a PMT with two chevron-stacked, microchannel plates which reduces the variation in this transit time based on its geometric configuration. Therefore, the C-DIR natively has a very low transit time spread and thus good timing resolution.

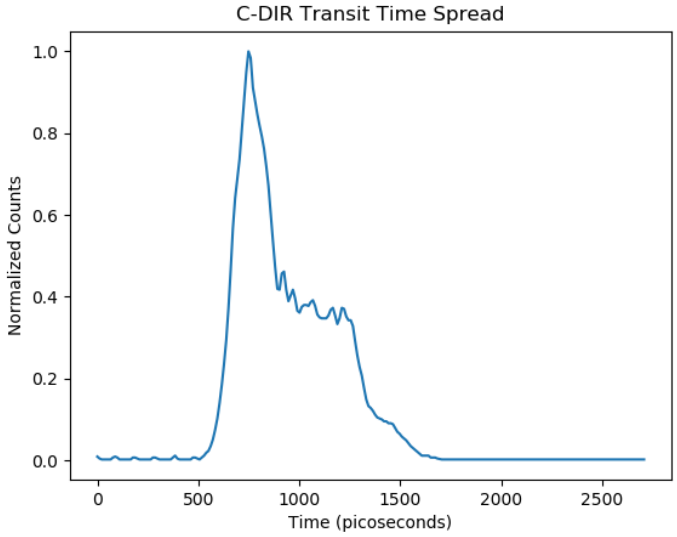

Figure 3.6-1 C-DIR Transit Time Spread for MCP PMT. This peak is 209 ps FWHM.

Figure 3.6-1 shows the TTS measurement taken for the system. This measurement was obtained using a Photek Laser Pulse Generator (LPG) which produces a pulse with wavelength 650nm (red) at a pulse width of 40ps. These lasers are developed to test the timing response of Photek photomultiplier tubes. Figure 3.6-2 shows the

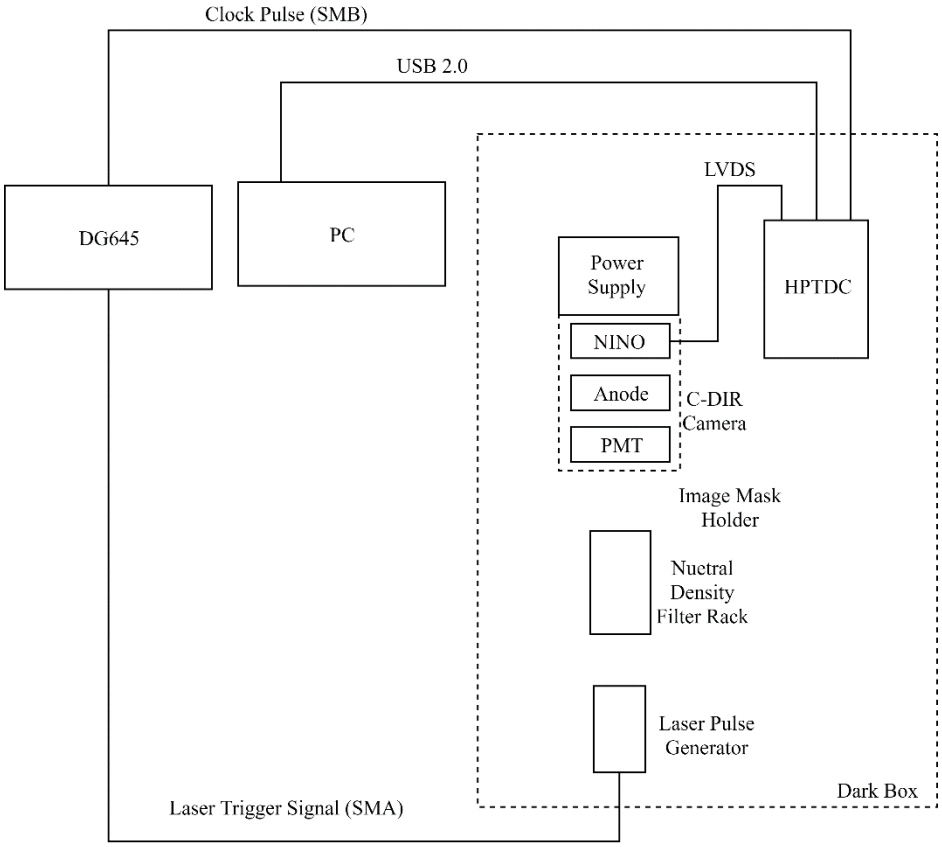

Figure 3.6-2 Experimental setup for transit time spread measurement of C-DIR. The Laser Pulse Generator was triggered with a DG645 delay generator. The pulse was attenuated using an ND filter rack down to $1/384\,th$ the incident signal intensity to protect the PMT from over-exposure and ensure photon counting conditions.

experimental setup for obtaining the TTS measurement. The LPG was heavily attenuated using a series of neutral density filters (ND8, ND6, ND4, ND2) to reduce the laser signal intensity to $^{1}/_{385}\,th$ its initial intensity. This ensured the PMT was protected from over-exposure to light and also acted to ensure photon counting levels, less than one detected photon per laser pulse. The TTS measured was 209 ps FWHM using this approach. This is about 50% worse timing performance than the cross-delay line H33D detector [35]. However, these two systems utilise differing PMT technology and the 209ps timing performance is consistent with the datasheet of the PMT 225 (2 microchannel plates at a 25mm diameter) supplied by Photek Limited.

3.6.2 Count Rate Limitations

Section 1.5.8 provided a very optimistic estimate for global count rate for the C-DIR of about 1MHz by factoring the dead-time of the constituent detector components. However, the main limiting factor which was discovered during testing was the data transfer rates between the HPTDC and the computer. The current implementation of the HPTDC electronics makes use of USB 2.0 technology. USB 2.0 has an absolute maximum theoretical bandwidth of 40MB/s when ignoring controller bandwidths. Encoding a single event with the C-DIR requires ten words or 40 bytes of data. A simple calculation shows that this corresponds to about 1MHz. Therefore, this limits the maximum global count rate for the system to be < 1MHz if no counts are going to be lost in buffer overflows in the HPTDC memory. This could obviously be improved by extending the hardware implementation to use the USB 3.0 standard which would allow data transfer rates exceeding 500MB/s this allowing at least an order of magnitude greater event counts i.e. 12.5MHz which is closer to our theoretical maximum calculated in 1.5.8.

3.6.3 Spatial Resolution

The spatial resolution of the device was taken using the USAF resolution chart approach in 3.4.4. The spatial resolution of the C-DIR was measured at 0.5 line pairs per millimetre.

3.7 Conclusions

This chapter sought to characterize the C-DIR in the context of a photon-counting system for FLIM applications. Important metrics under investigation included timing resolution, spatial resolution and global count rates. These investigations revealed even more of the properties of the C-DIR including noise, stability and

distortion. We were able to successfully measure and control several characteristics of the system. Hardware tweaks lead to the isolation and elimination of high voltage cross-talk. While software modifications to the base implementation outlined in Chapter 2 significantly reduced spatial distortion. The overview of the system performance metrics gathered as the major part of this work provided confidence for moving on to the next stage of real world testing of the device.

The amount of distortion present in the C-DIR camera leaves a lot of room for improvement in the anode design. Perhaps investigations into how anode geometries, capacitance between nodes, edge capacitance and overall uniformity of the capacitances influence image linearity require deeper investigation and are outside of the scope of this research project. Optimising the anode board design could not only assist in solving problems related to distortion but also image resolution. It may also be worthwhile testing the existing anode geometry with more stable readout electronics, for example, constant fraction discriminators which do not suffer from the drawbacks of time over threshold discriminators, however this would require a new technique for determining the charge centroid since the ToT vs charge calibration would be absent. These types of electronics were not available during this project and therefore this route could not be further explored and remains conjecture. The current prototype C-DIR board suffers from low spatial resolution compared to devices like the cross-delay line and cross-strip based detectors. However, these anodes are typically used in conjunction with CFDs so a direct comparison is not really possible or fair. However, in its current state, this low spatial resolution reduces its reach as far as applications for biological fluorescence, particularly super-resolution microscopy where the resolving power of the camera system is at the heart of the matter. Despite these shortcomings one cannot

completely rule out this device. The C-DIR could be useful in situations where high spatial resolution is not required.

The timing resolution of the C-DIR is such that it can measure relatively fast fluorescence lifetimes. The impulse response (or TTS) of 221ps will allow for measurements of many fluorescent probes with lifetime values >> 1.0ns [2] with reasonable accuracy. Although systems like the H33D report 2x more timing resolution, the limiting factor of the measurements come when coupled to microscope systems. It is reasonable to expect an IRF > 200ps when coupled with a microscope system [35] therefore this result is far from discouraging.

Characterising and documenting the C-DIR performance provided confidence for moving onto the next stage of conducting field trials. The chapter to follow further describes the C-DIR performance in real experimental conditions where results can be compared to those within the literature.

4 Field Trial: Calcium Imaging in Live Tissues using Capacitive Division FLIM

4.1 Introduction

This chapter describes two field tests designed to exercise the C-DIR as a fluorescence lifetime imager. The first test investigates the timing accuracy of the C-DIR device and assesses its ability to recover fluorescence lifetimes for well documented samples. The C-DIR was used in a single pixel mode as a fluorescence lifetime spectrogram as opposed to an imager to focus on the timing. The second test records 2-D fluorescence lifetime data in a live sample to observe expected fluctuations in lifetime based on biochemical processes which are occurring in the sample. The device was coupled to a single plane illumination microscope (SPIM) developed by Dr Phil Birch and Dr Roger Phillips of the University of Sussex [82].

4.2 Global Experimental Setup

4.2.1 Microscope and Imaging Setup

The C-DIR camera was coupled to a detection arm of a novel single plane illumination microscope (SPIM), alternatively termed light sheet microscope, developed at the University of Sussex Figure 4.2-1 called FLI-SPIM. Figure 4.2-2 shows the physical lab setup of the FLI-SPIM system. The FLI-SPIM

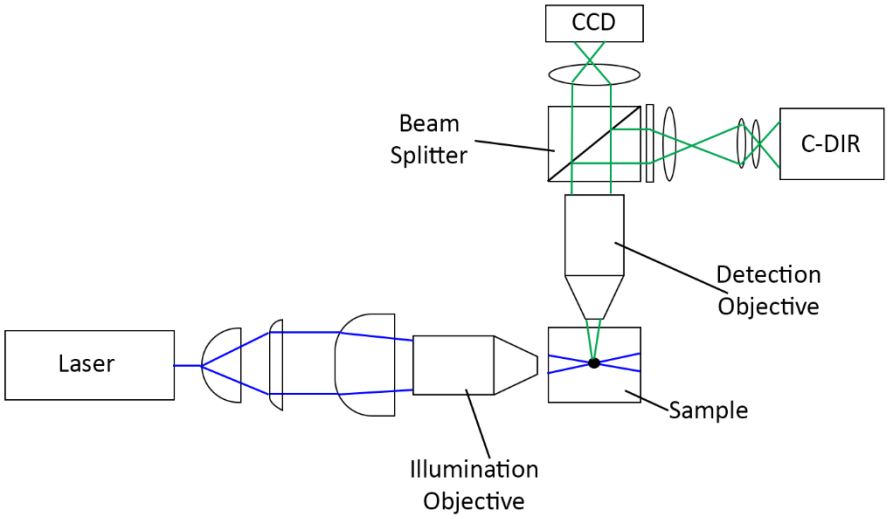

Figure 4.2-1 FLI-SPIM System developed by Dr Phil Birch at the University of Sussex. This is a single plane illumination microscope (SPIM) which contains two detection arms one for a conventional CCD camera and the other for the C-DIR device.

microscope consists of a commercial 470nm pulsed laser diode head driven by a PicoQuant PDL 800-D with a repetition rate of 40MHz and pulse width of 55ps

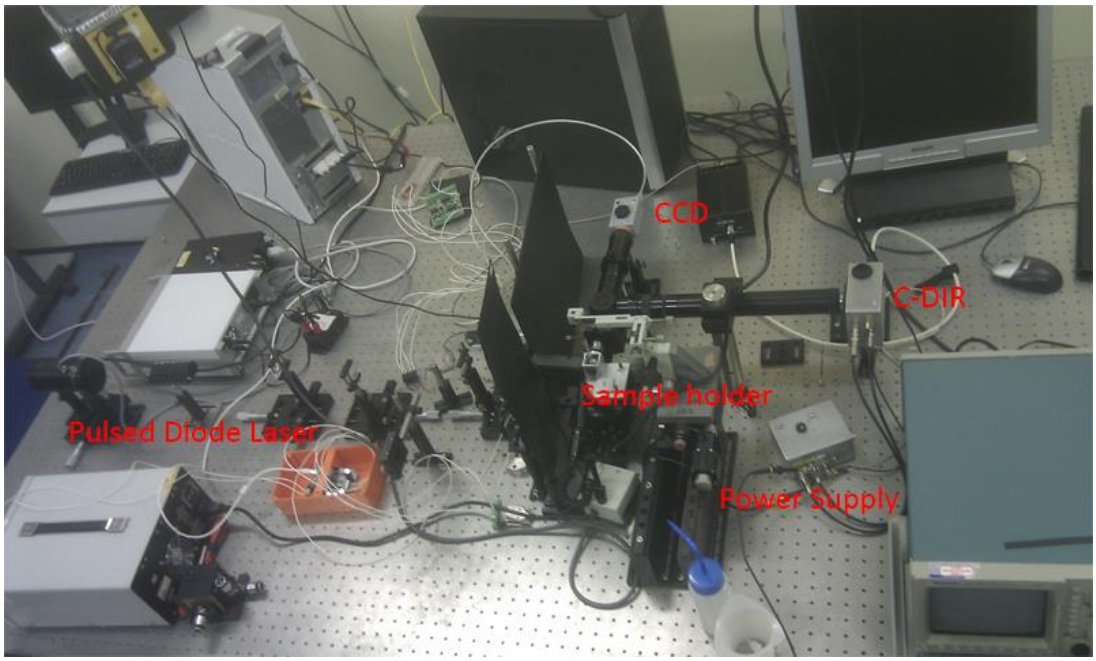

Figure 4.2-2 FLI-SPIM laboratory set-up.

FWHM. The light sheet is achieved by using two cylindrical lenses which expand the bream horizontally while maintaining the vertical width. The third and final

cylindrical lens focuses the vertical axis of the beam while the horizontal axis filled the back focal plane of a 10x infinitely-corrected objective thus forming a thin vertical light sheet at the objective focus. The detection arm was orthogonal to the illumination axis as shown in the diagram. A 20x water immersion objective NA o.8 lens collected and focused the signal towards a beam splitter which channels 10% of the signal to the C-DIR and 90% to an EMCCD Camera. The EMCCD camera was used to locate areas of the sample for investigation. It was also used to verify the image produced by the C-DIR. The FLI-SPIM microscope was selected for the field trials since it allowed testing of C-DIR as a wide-field fluorescence lifetime camera. The bonus of the optical sectioning inherent in the light sheet generation meant that there would be less measurement noise coming from parts of the sample which were not under investigation. Figure 4.2-3 shows an image of the empty sample holder and capilliary tube, used for inserting samples into the holder, taken by the EMCCD

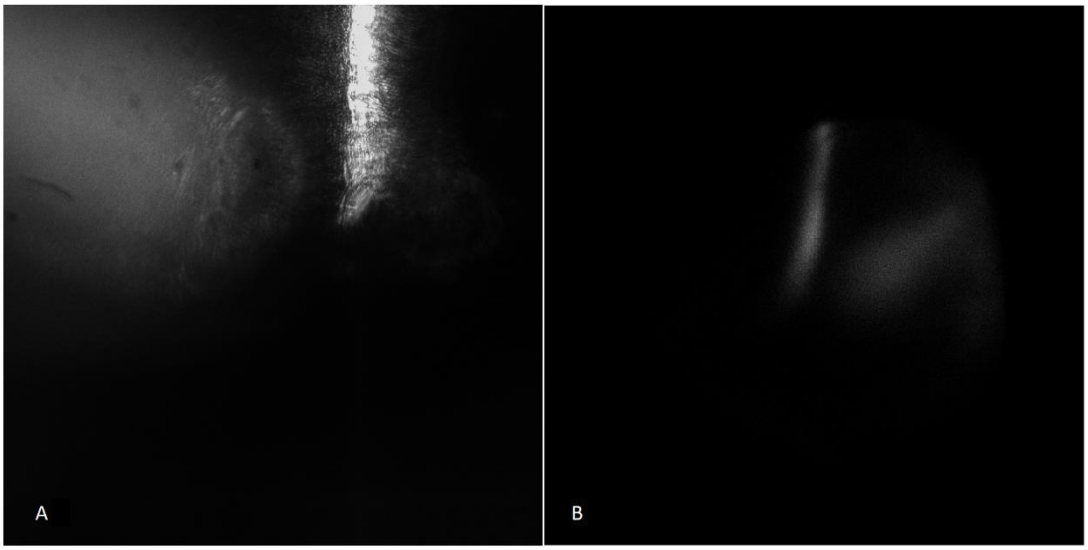

Figure 4.2-3 A) Image taken with the EMCCD of the inside of the empty sample holder with capilliary tube. B) The same image as detected by the C-DIR. The inversion is easily corrected in software but the low resolution is caused not only by the inherently low resolution of the image but also due to an issue with the coupling of the detection arm to the C-DIR. The image is produced outside of the focal plane of the C-DIR which was not trivial to correct.

and the C-DIR (B). The most two obvious issues with B is the poor resolution compared to the EMCCD and the difference in size and orientation. The EMCCD contains a 2/3 inch (~17mm) sensor versus the 25mm active diameter of the photomultiplier tube. The initial design for the C-DIR arm was based on the C-mount specification where the flange focal distance is 17.526mm. However, the C-DIR camera prototype focal distance was slightly further due to some physical offsets between the camera shielding described in 3.3.3 and the PMT photocathode. This resulted in very defocussed images as shown in Figure 4.2-4. Focusing and magnification were subsequently achieved by inserting a camera lens into the focusing arm. The field of view of the EMCCD was consequently ~4 times that

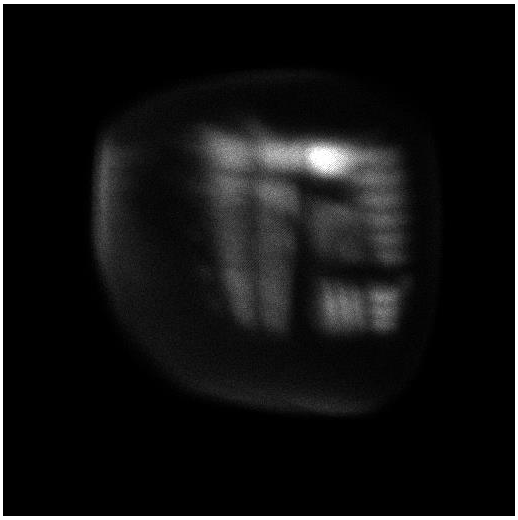

Figure 4.2-4 Attempt to measure resolution of C-DIR in initial coupling to the FLI-SPIM system. Spatial resolution degraded significantly due to errors in the coupling between the C-DIR system and the microscope arm.

of the C-DIR with minor improvements to the image sharpness (focussing) due to the inroduction of lens in the detection arm. This 4x field of view wa by design, the EMCCD camera was used to locate interesting features, the C-DIR was then used for the fluorescence lifetime measurements as the C-DIR did not have a “live view” mode. The difference in fields of view is demonstrated in Figure 4.2-5.

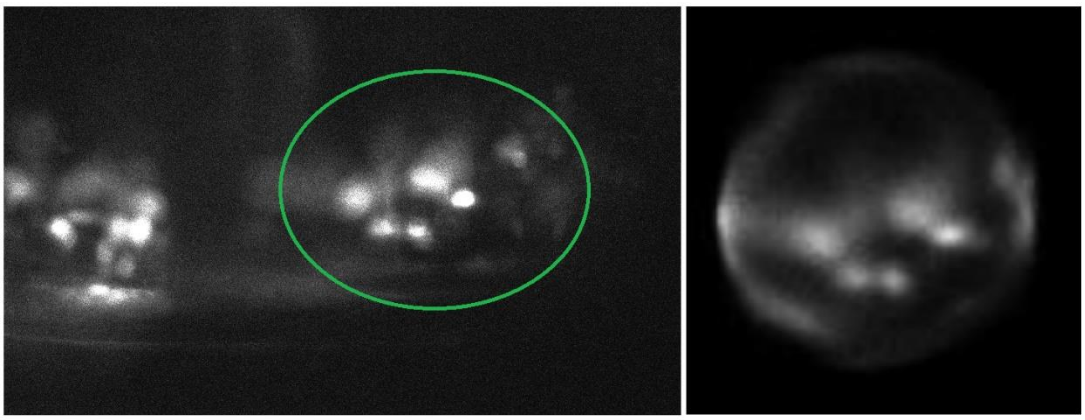

Figure 4.2-5 Image of haemocytes in Drosophila prepupae. The left was taken with the EMCCD. Circled is the corresponding field of view of the C-DIR which shows the image taken on the right. This was taken after improvements to the coupling with the C-DIR. The C-DIR magnification was roughly 4x that of the EMCCD and spatial resolution was improved to the original 0.5lppm with the focusing of the camera lens.

4.2.2 Instrument Response Function

The IRF of the system was measured with the experimental setup shown in Figure 4.2-1. The sample holder was left in place with no sample and reflections were imaged from the inside edge of the sample holder onto the C-DIR. This was done to match the conditions for acquiring the TTS in 3.6. Figure 4.2-6 shows the measured

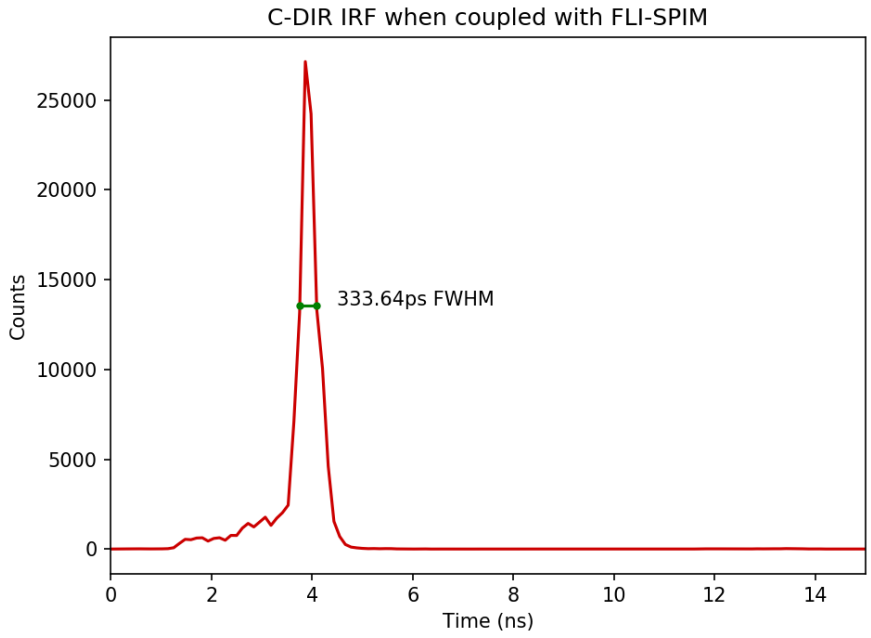

Figure 4.2-6 Instrument response of C-DIR when coupled with FLI-SPIM. This width of the pulse was measured at ~334 picoseconds FWHM.

impulse response which was 333.64 picoseconds FWHM for the FLI-SPIM system.

4.3 Calcium Calibration of the C-DIR System

4.3.1 Oregon Green Bapta-1

Studies have shown the calcium sensitivity of Oregon green dyes [83] [84] which makes them a useful marker for observing chemical processes within living cells. Fluorescence imaging of calcium sensitive dyes can provide insight into the electro-chemical states within living cells as calcium is a ubiquitous, crucial component of many functions within live organisms [34] [84]. Oregon Green Bapta-1, OGB-1, is known to have two exponential components [2] [34] [84]. The long component, $\tau_{long} \simeq 4ns$, represents bound Ca^{2+} while the short component, $\tau_{short} \simeq 0.5ns$ represents free Ca^{2+} ions. Agronskaia et al have designed an experiment which allows the quantification of calcium concentrations within a sample using fluorescence lifetime. Here the average fluorescence lifetime of the bi-exponential OGB-1 fluorescence provides a direct measure of the ion concentration within a sample. Instead of using live cells, the quantification was achieved using a series of calcium buffers with known free Ca^{2+} ion concentrations. These buffers are used as a calibration of the measurement system. The average lifetime information obtained from the buffers could then be used in a live situation for quantitative calcium imaging within cells.

OGB-1 has an absorption maximum at 494nm and emission around 520nm [84] [2] [85]. The FLI-SPIM system produces excitation at 470nm which falls within the excitation range for OGB-1. The PMT component of the C-DIR makes use of an S20 photocathode which has peak efficiency in the visible spectrum, including 520nm, and a fused silica input window which has above 90%

transmission in the visible spectrum [86]. The literate shows a biexponential property associated with a fast decaying lifetime component between 0.25-0.53ns and a longer decay component of ~4ns.

4.3.2 Objectives

This experiment provided a good basis for testing the C-DIR device. Firstly, the lifetimes recovered by the C-DIR for OGB-1 can be compared with the literature to validate the accuracy of the measurement system. Furthermore, calcium buffer measurements could provide some insight into the uniformity of the fluorescence lifetime measurement over the full active area of the detector. Finally, calibrating the C-DIR using the calcium buffer series tests the capability to measure and discriminate expected fluorescence lifetimes at varying calcium concentrations.

4.3.3 Sample Preparation

The samples used in this experiment were prepared and stored by Roger Phillips and Xaiofei Li of the School of Life Sciences, University of Sussex. There were ten samples prepared with varying concentrations of Ca^{2+} ranging from 0-38.9µM. Samples were injected using a syringe into the capillary sample holder.

4.3.4 Results and Discussion

Figure 4.3-1 shows the combined instrument response and calcium buffer data decay

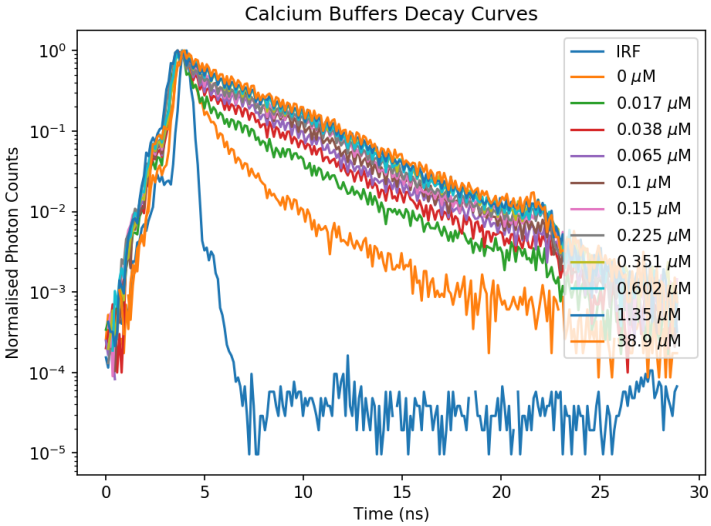

Figure 4.3-1 Decay curves of OGB-1 calcium buffer series measured by the C-DIR.

curves. This data was captured using the C++ based analysis software developed in 2.5. A small script was developed to convert the C-DIR data to a format readable by the TRI2 software which was used for 2-D fluorescence lifetime fitting. The data was binned to satisfy width and height of 256x256 pixels where each pixel contained 256 time-channels. This helped to increase the statistics for the fit. The IRF, previously obtained and in 4.2.2, was used as the excitation or prompt for the fitting software.

Figure 4.3-2 shows a resulting exponential fit using our 10µM Ca^{2+} OGB-1 sample. Even a preliminary estimate shows good agreement with what is expected

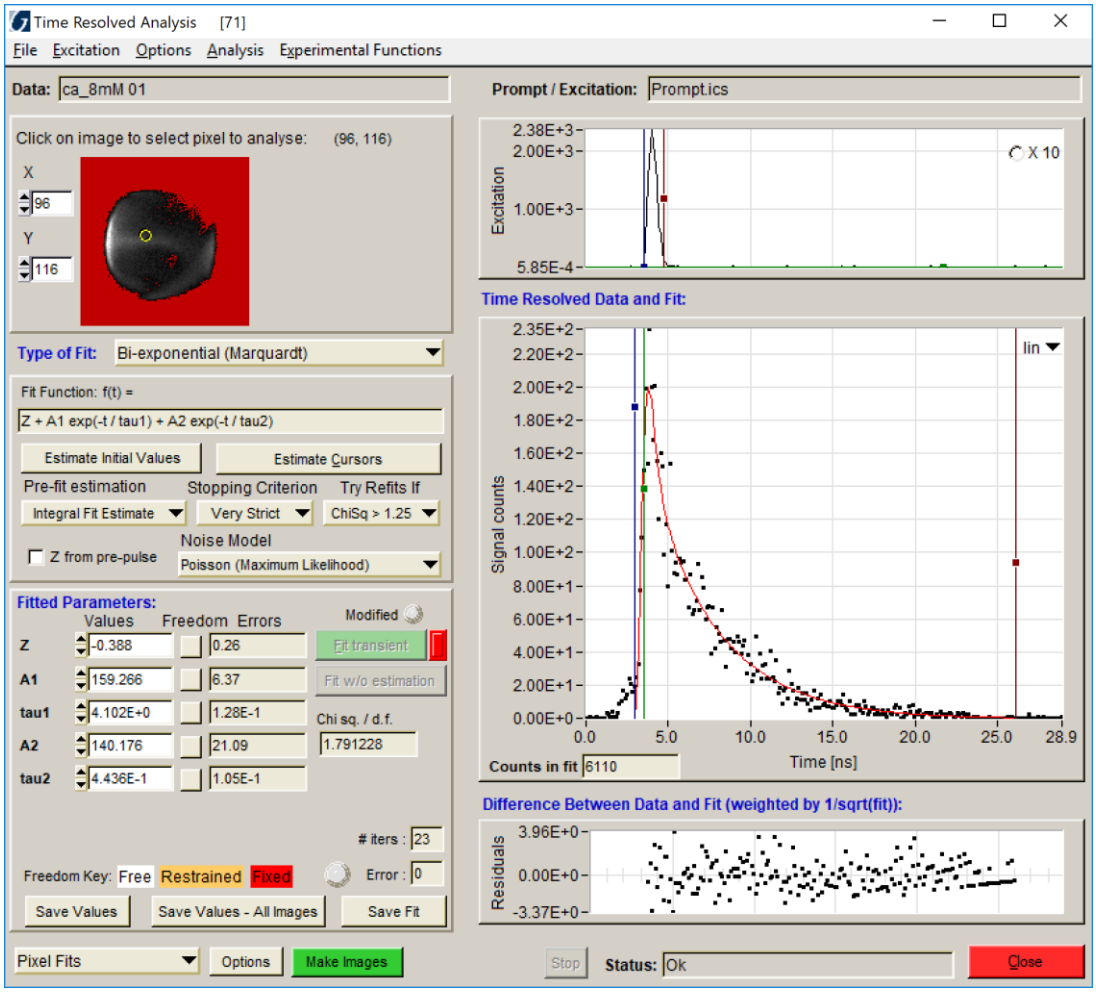

Figure 4.3-2 Setting up the exponential fit for an OGB-1 sample 10 with 0.602µM of free Ca^{2+}. This initial set-up and location of initial parameters is required before doing an entire fit in 2D. Even with the basic setup we have good agreement with the literature.

from the literature. After setting up the initial fit, a 2D fit was performed over the entire surface of the C-DIR production the outputs in Figure 4.3-3 Fit result for the 0.603µM sample over the surface of the C-DIR. From left to right we have the intensity image, long lifetime component, short lifetime component, relative intensity of the short component and finally the relative intensity of the short component.. The fitting model selected yielded good results for the long and short component lifetimes of OGB-1 where were $\tau_{long} \simeq 4 \pm 0.113ns$ and $\tau_{short} \simeq 0.54 \pm 0.17ns$ for the 38.9µM sample which is supported by the literature. At this concentration, the long component dominates the fluorescence signal. The second

image from the right in Figure 4.3-3 Fit result for the 0.603µM sample over the surface of the C-DIR. From left to right we have the intensity image, long lifetime component, short lifetime component, relative intensity of the short component and finally the relative intensity of the short component. demonstrates the uniformity of the long component measurement over the surface of the C-DIR Detector. The fit was obtained for good values of χ_ν^2 ranging between 0.98 and 2.40.

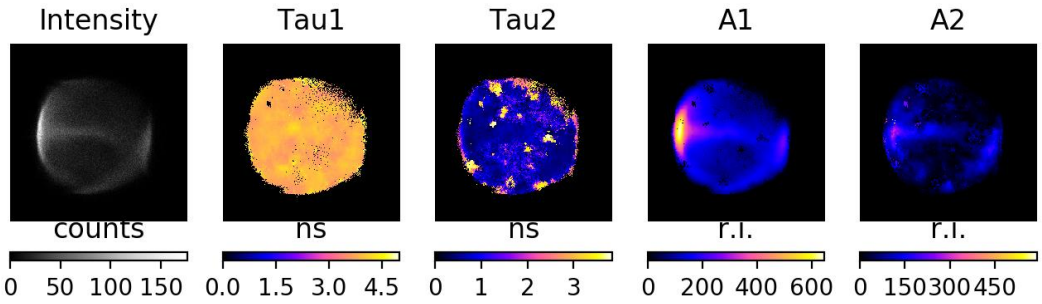

Figure 4.3-3 Fit result for the 0.603µM sample over the surface of the C-DIR. From left to right we have the intensity image, long lifetime component, short lifetime component, relative intensity of the short component and finally the relative intensity of the short component.

Table 4.3-1 shows the fitting result for each of the ten calcium buffers. The expected trend of increasing relative intensity of the long component with increasing concentration is observed by comparing the first and last columns. This table represents the calibration of the C-DIR for quantitative Ca^{2+} measurements and will be used in a further experiment for calcium imaging in live tissue.

Table 4.3-1 C-DIR fluorescence lifetime for the long and short components of OGB-1 at varying concentrations of Ca^{2+}. Notice the increase in relative intensity of the long component as the free Ca^{2+} concentration increases. The percentage amplitude of the short component is $100 - A_{long}$.

Concentration of free Ca^{2+} (μM)	τ_{long} (ns)	τ_{short} (ns)	A_{long}(%)
0	2.5	0.59	11
0.017	3.4	0.47	22
0.038	3.3	0.28	24
0.065	3.3	0.27	38
0.1	3.5	0.30	45
0.15	4.0	0.35	48
0.225	3.9	0.45	56
0.351	3.9	0.41	63
0.602	3.8	0.40	70
1.35	3.9	0.29	100
38.9	3.7	0.29	100

$$R = \frac{A_{short}}{A_{long}+A_{short}} \qquad \textbf{4.3-1}$$

The ratio *R* of fluorescence lifetime is given by the relationship between the free calcium concentration and *R*, along with the how the contribution of the long component varies with concentration is shown in Figure 4.3-4. This relationship can be used directly to quantify the concentration

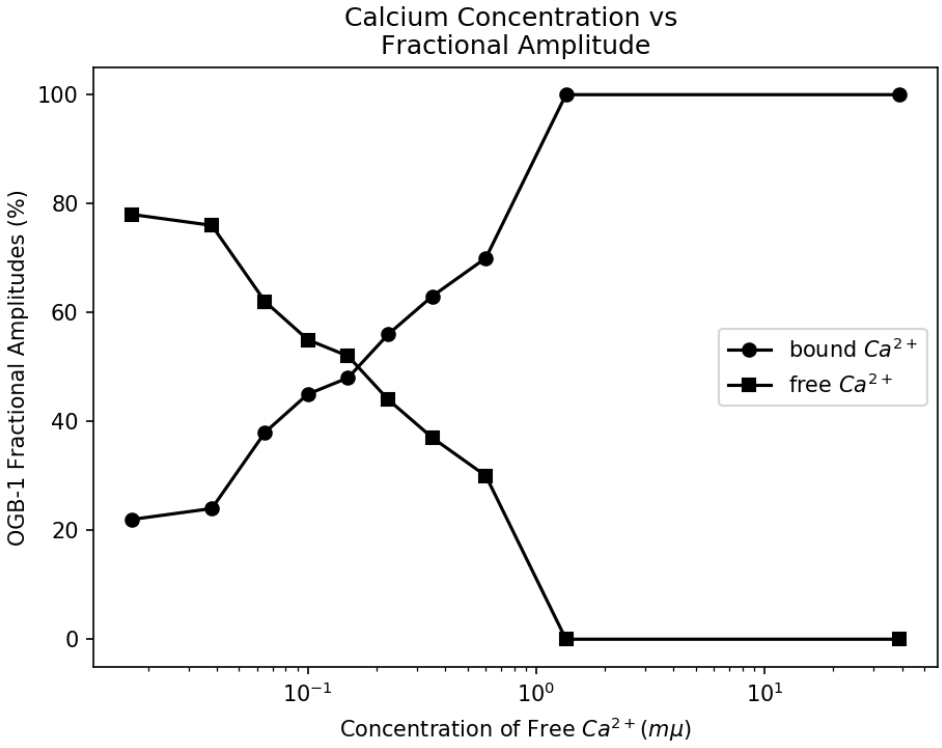

Figure 4.3-4 Relationship between the concentration of free Ca^{2+} and fractional amplitude (intensity) of the long and short lifetime contributions which correspond to the bound and free states of OGB-1 respectively.

of free Ca^{2+} in tissue samples.

4.4 Quantitative Calcium Imaging using C-DIR

4.4.1 Calcium Imaging using OGB-1 in Living Tissue

The experiment presented in 4.3 provides a basis for the quantification of calcium concentrations within living tissue. Here we will use the calibrated C-DIR system to test the relative concentration of free and bound Ca^{2+} in live tissue. Figure 4.4-1

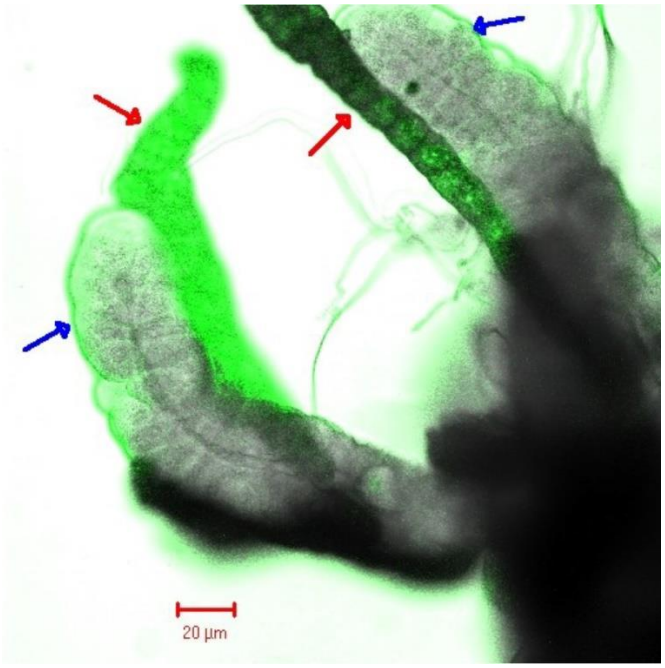

Figure 4.4-1 Composite epifluorescence (green) and brightfield (white) image of Drosophila larval tissue, incubated with OGB-1, imaged using the CCD arm of the FLI-SPIM system. Blue arrows indicate giant polytene salivary gland cells which show lower fluorescence intensity than adherent fat body cells (red arrows).

shows a tissue sample which was dissected from Drosophila larvae. The sample preparation was once again performed by members of the school of Life Sciences at the University of Sussex. The larva was incubated with OGB-1 Acetoxymethyl (AM). Epifluorescence images show higher intensity in adherent fat body regions than in the actual salivary duct. The fluorescence calibration of the C-DIR will allow for a quantitative measure of Ca^{2+} bound and unbound in the drosophila salivary glands and fat body to perform a ratio-metric comparison and determine which area of the tissue has the higher calcium concentration.

4.4.2 Results and Discussion

The results of the calcium imaging in the fat body and salivary gland comparisons

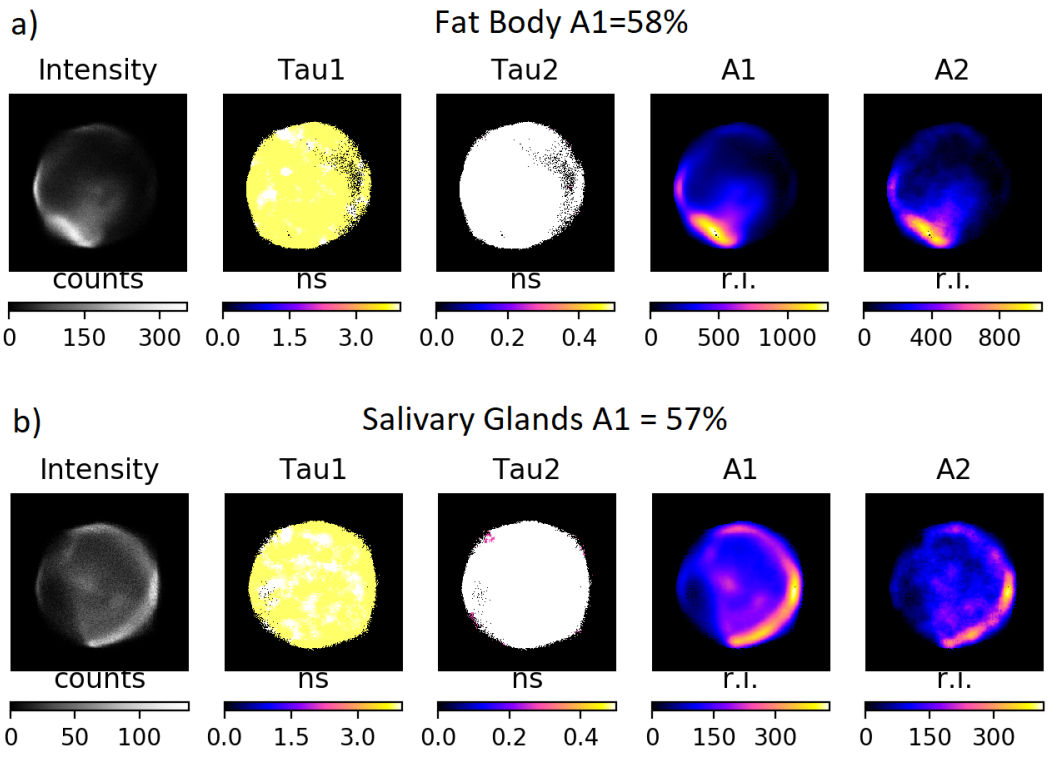

Figure 4.4-2 The top series of images a) show the result of the 2D bi-exponential fit for the fat body cells and the bottom series b) the result for the salivary glands. Fitting parameters varied within the confines of those lifetime values recorded in 4.3.4. Visually, we see comparable intensities between A1 and A2 in both series which indicates similar concentrations of free and bound calcium in both cases. The A1 (long lifetime component) was ~58% contribution in both the salivary gland and the fat body.

are shown in Figure 4.4-2. Without the need to determine the actual value of the concentrations of calcium within the samples we can clearly see that there is a slightly higher percentage of bound Ca^{2+} in each sample given the higher contribution of the long lifetime component in both cases. This result shows that despite the almost 3x average brighter intensity signal in the adherent fat body, there is a very similar concentration ratio between Ca^{2+} in the bound and free states.

4.5 Conclusions

The preceding experiments demonstrated the accuracy of the C-DIR for recording fluorescence lifetimes by reproducing lifetime values for OGB-1 consistent with published results [2] [34] [84]. The χ_v^2 variation for the model employed was in an

acceptable region very close to 1 (0.8-2.5) for all fits as is consistent with the tolerance for reduced chi-squared used by Agronskaia et al[34]. Higher chi-squared values could be resulting from systematic errors in the fit for lower concentrations of Ca^{2+}. The lifetime of ~0.5ns is very short compared to the ~334ps FWHM IRF therefore we were very close to our limiting time resolution for the fitting. Despite this, the C-DIR was still able to successfully record the full calcium calibration over the range of buffers provided. The trend of fractional contributions of free and bound Ca^{2+} were also consistent with the literature as was demonstrated in Figure 4.3-4. The calibration was then used to discriminate calcium levels between the salivary duct cells and adherent fat body of a Drosophila sample. The C-DIR was able to show that, despite much higher fluorescence intensities in the fat body, the fractional fluorescence amplitudes were very similar in both the fat body and the salivary duct. Therefore, although dye uptake in the fat cells are higher, calcium levels were the same.

5 Discussion and Conclusion

5.1 Summary and Final Conclusions

The objective of this research was to present a solution for wide-field time-resolved fluorescence imaging using the capacitive division technique. The C-DIR promised MCP-limited photon-counting rates exceeding those of other detector systems in its class. This promise created the first challenge of developing a software system which could cope with these rates. Chapter 2 addressed this issue by using knowledge of the HPTDC raw output data format, the maximum theoretical USB 2.0 data rates, and predicted system behaviours to come up with a simulated data set which could then be tested using an incrementally developed data reduction platform. The data reduction software was mostly developed before the final manufacture of the C-DIR components thanks to the generation of a large simulated dataset. Further optimizations which made use of current threading technologies on modern CPUs enabled the development of a commercially viable, high speed software package which adequately handled full USB data rates reliably. This required the use of strict software engineering principles for design and quality assurance.

In Chapter 3, we attempted to characterize the C-DIR in the context of a FLIM measurement system. During this process, several short-comings of the C-DIR and associated electronics were identified which affected the maximum realisable spatial and temporal resolution and therefore required modifications to the system design to reduce noise, correct distortion and improve timing response. The performance of the C-DIR was also evaluated in these respects. The reduction in noise was a challenging process. Settling on the decision to use aluminium housings and cabling

with high levels of shielding resulted from several investigations into possible sources of noise. Once the major contributor, high voltage noise, was isolated a marked improvement in performance was observed throughout the entire system. Since the NINO ASIC was responsible for charge sensing, and therefore imaging, as well as timing performance, isolating and reducing noise at this interface was critical for maximizing the performance of the entire system. After isolating noise contributions, the mathematical approach of PCA to reduce the effects of discriminator time walk was highly beneficial in achieving optimal timing resolution. Distortion in the system was mostly predictable within the centre region of the detector and easily corrected in software. Attempts to use a physical 2-D distortion correction was an overkill, in hindsight, since the correction was not significantly better than the Brown-Conrady distortion. Fortunately, the decision was made to investigate the Brown-Conrady distortion algorithm as an alternative to the far more complex 2D physical correction.

Best efforts to control noise and distortion yielded a device with timing resolution of 209ps FWHM and spatial resolution of 0.5lppm. Despite using a different metric from other devices in measuring spatial resolution, it was clear from qualitative observations that the non-linear ToT vs charge calibration was not the best solution for imaging, especially considering the volatility of the threshold. In terms of count rates, the C-DIR was limited by the USB 2.0 data bandwidth which corresponded to a global count rate of ~1MHz. In practice, the C-DIR was not pushed beyond a global detection count rate of just above 800KHz. This was better than the H33D system but could be pushed even further by supporting USB 3.0.

Chapter 4 concluded the C-DIR evaluation with an acid test in real-world experimental conditions. The challenge was not only to accurately reproduce the

fluorescence lifetime of OGB-1, but if successful, fully calibrate the C-DIR for quantitative calcium imaging. The C-DIR met expectations by being able to recover the fluorescence lifetime of OGB-1 as well as demonstrate the calcium dependence of the fluorescence lifetime of OGB-1 bound and free states as a function of calcium concentration. With absolute confidence in the C-DIR based on this successful calcium calibration, supported by previous findings in the literature, a real quantification of calcium in the fat body cells and the salivary duct of a Drosophila sample was performed. The C-DIR was able to successfully reveal that levels of free OGB-1 were similar in fat body cells and salivary glands despite vast differences in fluorescence intensity.

To date, the C-DIR is the most performant photomultiplier-based detector system in terms of global count-rates as compared to other similar devices in its class, see Table 1.5-1. The closest rival, H33D detector system, has a read-out electronics limited count rate of 500KHz which is below the C-DIR theoretical maximum and below the current realisable maximum of 1MHz due to USB 2.0 limitations. Solid-state techniques like that described by Li et al. offer faster lifetime determination due to pixel-level timing electronics for lifetime calculation [49]. In this approach, the local detection rate of each SPAD pixel is independent or neighbouring SPADs and not limited by MCP dead-time or saturation effects [49]. Despite these clear advantages, the system still suffers low quantum efficiency due to the smaller active pixel area, which is taken up by timing electronics and a small pixel count which limits its ability for imaging [49]. The moderate spatial resolution provided by the C-DIR exceeds the 32x32 and 32x16 resolution offered by the solid-state alternative with higher global count-rates. Improvements in anode architecture and interfaces between anode, NINO and TDC could improve noise performance and significantly

improve timing resolution beyond the ~200ps FWHM obtained. In terms of image distortion and resolution, the C-DIR is slightly behind other imaging photon detectors at present. However, improvements to the design of the prototype board possibly optimizing surface capacitance using anode geometry, as was already demonstrated by Lapington et. al for space applications [1], could result in improvements to image distortion. Decoupling timing read-out from position centroiding and avoiding the non-linear ToT mechanism for charge centroid calculation may improve the spatial resolution. General suggestions for improving the system are presented in 5.2.

5.2 Future System Development

The characterization of the C-DIR in Chapter 3 highlighted issues which ultimately affect the temporal and spatial resolution of the detector. Moving forward, this situation could possibly see marked improvement by either reducing the noise on the charge sensing from the anode or utilizing a mechanism for decoupling the timing and position centroiding.

5.2.1 Conceptual System Improvement

The current C-DIR system makes use of the NINO ASIC for fast sensing of input charge. The speed benefit of using a ToT discriminator compared to perhaps CFDs did not seem worthwhile. The susceptibility of ToT discriminators to noise and threshold drift meant that it was difficult to reduce noise levels and distortion in the final image without resorting to software corrections, the effect of noise may have also adversely affected image resolution. Avoiding the ToT mechanism for imaging may be implemented by recording the MCP-out timing and comparing this with arrival times at each of the corner anodes. Although the version of the MCP-PMT

used in this study provided a compatible interface for the MCP out signal, the NINO chip itself only contained 4 input channels. There are however 8-channel versions of

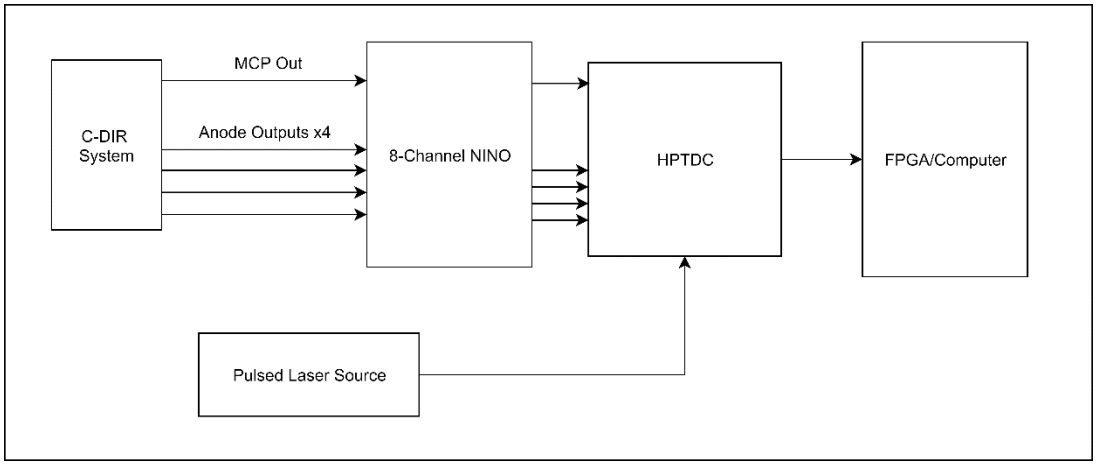

Figure 5.2-1 Proposed improvement to C-DIR system architecture which makes use of an 8-channel NINO. The MCP out signal could be used in conjunction with the anode arrival times to centroid the position of the incident charge in a similar manner to the XDL anode. This would completely bypass the non-linear ToT mechanism as it is currently used for position centroiding.

the NINO like the one used for the ALICE time-of-flight instrument at CERN [76]. The system would then take on the design shown in Figure 5.2-1. Since the ToT mechanism is no longer needed for imaging, it may be more useful to employ fast discrete CFDs or some fast multi-channel CFD implementation like those produced by CAEN as they are less prone to amplitude walk effects. An outline of the

proposed system changes is shown in Figure 5.2-2.

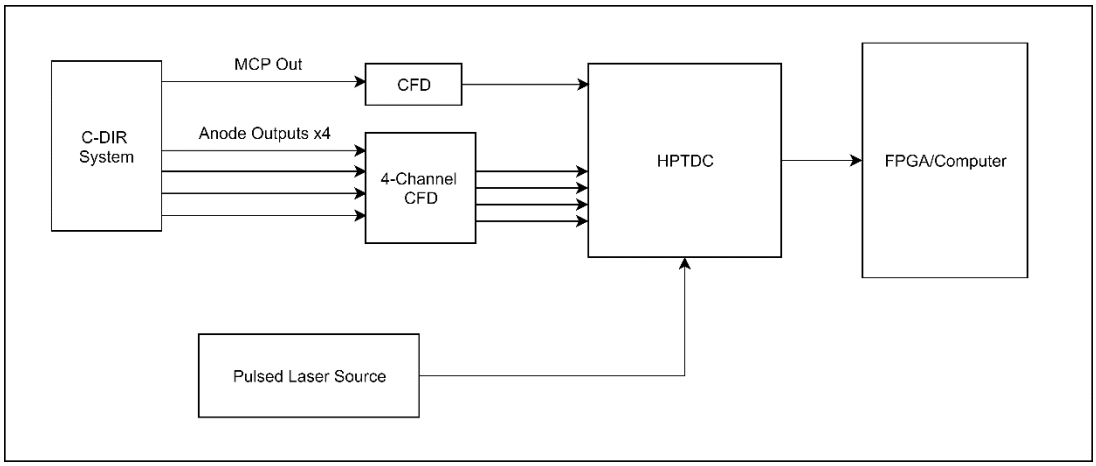

Figure 5.2-2 TCSPC set-up for the conceptual improvements to the C-DIR measuring system. The CFD array replaces the NINO and changes the way charge centroiding is achieved.

If the time difference between the MCP arrival time and the time at a channel is given by $t_{i_{diff}} = t_i - t_{mcp} \quad i \in \{A, B, C, D\}$ then the charge centroid can be calculated using:

$$x = \frac{t_{A_{diff}} + t_{B_{diff}}}{t_{A_{diff}} + t_{B_{diff}} + t_{C_{diff}} + t_{D_{diff}}} \text{ and } y = \frac{t_{C_{diff}} + t_{D_{diff}}}{t_{A_{diff}} + t_{B_{diff}} + t_{C_{diff}} + t_{D_{diff}}}$$

This is a similar centroiding algorithm to the one currently used by the C-DIR, however knowledge of the incident charge magnitude is no longer necessary, thus becoming similar conceptually to the delay line time difference in the H33D XDL system. This measurement is of course limited by the timing resolution of the CFDs. In order to maintain our theoretical rates, one would need CFDs able to operate at rates approaching those of the NINO channels.

The modifications to the C-DIR system mentioned in the previous section would not come without drawbacks. The first issue which could be encountered is system bulk. The current format of the C-DIR is compact with the PMT, anode and NINO existing in a single housing which were about 100x100x50mm. The associated

power supply unit which powered the entire camera was placed in a housing with identical dimensions. CFDs typically have volumes exceeding those of the C-DIR camera housing. Associated power supplies may also be complex to use and likewise bulky. Although the C-DIR was never designed for portability, its compactness and ease of use were beneficial. There is now an increased cognitive burden on users to properly configure power for the C-DIR and the CFDs separately compared to the CDIR which uses a single power supply for all components. Additionally, the CFDs need to be situated on the outside of the enclosed PMT housing which requires design of a new interface between the main camera and the CFDs to minimize light leaks.

5.2.2 Future Software Improvements

The software developed as part of this project was mainly focused on the acquisition, reduction, visualisation and fast streaming to disk of the fluorescence signal from the C-DIR. There is a lot of scope for further developing this software to allow fast FLIM at video rates either by using very fast time-domain fitting techniques [87] or by using the phasor approach which transforms the time-of-flight data into frequency space using Fourier techniques [55] [88]. This could provide direct, real-time FLIM imaging. If used in conjunction with a USB 3.0 implementation of the TDC or some higher bandwidth interface, further optimizations or high-performance computing techniques like the message passing interface, MPI, would be required to cope with these higher data rates.

5.3 Further Experiments

5.3.1 Biosensors for FLIM-FRET

In chapter 4, we examined the action of a single fluorescence molecule, OGB-1, as a biosensor for the calcium concentration Drosophila larval cells. Other biosensors like blue fluorescent protein, BFP, and yellow fluorescent protein, YFP are known to interact as a FRET pairs [89]. FRET pairs are used to measure distances between molecules as well as bound/un-bound states of interacting molecules [89] [90]. YFP quenches the fluorescence of BFP by absorbing energy through non-radiative pathways. This shortens the lifetime of BFP. As binding between BFP and YFP molecules increase, the fluorescence lifetime of the BFP will show a measurable decrease. The C-DIR could be used in an experiment of this type to determine intermolecular distances within biological samples or interactions between molecules at the sub-cellular level.

5.3.2 3-D FLIM

So far, we have used the FLI-SPIM microscope to image static optical sections through our samples. The FLI-SPIM does not yet have the capabilities to synchronise the scanning of samples through the light-sheet with data acquisition. Further developments of the FLI-SPIM system in conjunction with resolution improvements for the C-DIR would facilitate time-resolved 3-D reconstructions of structures with fluorescence lifetime information. The result would be 5-Dimensions of data, 3-D structure, fluorescence lifetime and experiment time (duration).

5.4 Potential Applications

The resolution of the C-DIR in its current state would not allow for highly spatially resolved fluorescence imaging. However, this system could be used in a crude

scanning microscope set-up to scan restricted 2-D sections in a wide-field mode. This would allow maximising the area of the C-DIR with the least distortion to build up a larger 2-D FLIM image. This has the advantage of immediately providing more information that a point-scanning confocal system for example. Combining 2-D images would require sophisticated software stitching techniques but could, in principle, result in faster data acquisition that point-scanning.

If the proposed system improvements mentioned in 5.2 were to be realised, this would make the C-DIR a good candidate for wide-field high-resolution FLIM. The C-DIR could either be used in its current set-up with the SPIM microscope to image highly spatially resolved thin sections through large biological samples, or in conjunction with fast laser scanning, confocal, techniques to produce super-resolution FLIM images of cells or even single-molecules.

5.5 Closing Remarks

Investing in improving the C-DIR could result in an extremely competitive system for time-resolved fluorescence microscopy. We are yet to see its full potential in terms of count rates and imaging resolution. Improvements in HPTDC design, using new techniques for charge centroiding, or investigating different read-out electronics combinations could form the basis of new research projects which could push the future of this technology and potentially the field of fluorescence lifetime imaging.

6 References

[1] J. S. Lapington, "High speed imaging using a capacitive division technique," *Nuclear Instruments and Methods in Physics Research Section A: Accelerators, Spectrometers, Detectors and Associated Equipment*, vol. 695, no. 1, pp. 410-414, December 2012.

[2] J. Lakowicz, *Principles of Fluorescence Spectroscopy*, 3rd ed. New York: Springer, 2010.

[3] G. C. Holst and T. S. Lomheim, *CMOS/CCD Sensors and Camera Systems*. Winter Park/Washington USA: JCD Publishing/SPIE Press, 2007.

[4] J. Délèze, B. Delage, O. Hentati-Ksibi, F. Verrecchia, and J. C. Hervé, "Fluorescence Recovery After Photobleaching," in *Connexin Methods and Protocols*. New York: Springer-Verlag, 2010, pp. 313-327.

[5] K. Staras, D. Mikulincer, and D. Gitler, "Monitoring and quantifying dynamic physiological processes in live neurons using fluorescence recovery after photobleaching," *Journal of Neurochemistry*, 2013.

[6] G W Gordon, G Berry, X H Liang, B Levine, and B Herman, "Quantitative fluorescence resonance energy transfer measurements using fluorescence microscopy," *Biophysical Journal*, vol. 74, no. 5, pp. 2702–2713, 1998.

[7] A. H. A. Clayton, N. Klonis, S. H. Cody, and E. C. Nice, "Dual-channel photobleaching FRET microscopy for improved resolution of protein association states in living cells," *European Biophysics Journal*, vol. 34, no. 1, pp. 82-90, 2005.

[8] J. G. White, W. B. Amos, and M. Fordham, "An evaluation of confocal versus conventional imaging of biological structures by fluorescence light microscopy," *The Journal of Cell Biology*, vol. 105, no. 1, pp. 41-48, 1987.

[9] W. R. Zipfel, R. M. Williams, and W. W. Webb, "Nonlinear magic: multiphoton microscopy in the biosciences," *Nature Biotechnology*, vol. 21, no. 11, pp. 1369–1377, 2003.

[10] P. P. Provenzano, K. W. Eliceiri, and P. J. Keely, "Multiphoton microscopy and fluorescence lifetime imaging microscopy (FLIM) to monitor metastasis and the tumor microenvironment," *Clinical & Experimental Metastasis*, vol. 26, no. 4, pp. 357-370, 2009.

[11] M. Weber and J. Huisken, "Light sheet microscopy for real-time developmental biology," *Current Opinion in Genetics & Development*, vol. 21, no. 5, pp. 566-572, 2011.

[12] J. Huisken, J. Swoger, F. Del Bene, J. Wittbrodt, and E. H. K. Stelzer, "Optical Sectioning Deep Inside Live Embryos by Selective Plane Illumination Microscopy," *Science*, vol. 305, no. 5686, pp. 1007-1009, August 2004.

[13] M. Weber, M. Mickoleit, and J. Huisken, "Light Sheet Microscopy," in *Quantitative Imaging in Cell Biology*, Jennifer C. Waters and Torsten Wittman, Eds.: Academic Press, 2014, vol. 123, ch. 11, pp. 193-215.

[14] P. G. Pitrone et al., "OpenSPIM: an open-access light-sheet microscopy platform," *Nature Methods*, vol. 10, pp. 598-599, June 2013.

[15] P. J. Keller, A. D. Schmidt, J. Wittbrodt, and E. H. K. Stelzer, "Reconstruction of Zebrafish Early Embryonic Development by Scanned

Light Sheet Microscopy," *Science*, vol. 322, no. 5904, pp. 1065-1069, November 2008.

[16] M. B. Ahrens, M. B. Orger, D. M. Robson, J. M. Li, and P. J. Keller, "Whole-brain functional imaging at cellular resolution using light-sheet microscopy," *Nature Methods*, vol. 10, pp. 413-420, March 2013.

[17] F. Arginelli et al., "High resolution diagnosis of common nevi by multiphoton laser tomography and fluorescence lifetime imaging," *Skin Research and Technology*, vol. 19, no. 2, pp. 194-204, 2013.

[18] E. Dimitrow et al., "Sensitivity and Specificity of Multiphoton Laser Tomography for In Vivo and Ex Vivo Diagnosis of Malignant Melanoma," *Journal of Investigative Dermatology*, vol. 129, no. 7, pp. 1752-1758, 2009.

[19] K. König et al., "Applications of multiphoton tomographs and femtosecond laser nanoprocessing microscopes in drug delivery research," *Advanced Drug Delivery Reviews*, vol. 63, no. 4-5, pp. 388-404, 2011.

[20] X. Gao, Y. Cui, R. M. Levenson, L. W. K. Chung, and S. Nie, "In vivo cancer targeting and imaging with semiconductor quantum dots," *Nature Biotechnology*, vol. 22, no. 8, pp. 969-976, 2004.

[21] S. W. Perry, R. M. Burke, and E. B. Brown, "Two-Photon and Second Harmonic Microscopy in Clinical and Translational Cancer Research," *Annals of Biomedical Engineering*, vol. 40, no. 2, pp. 277-291, 2012.

[22] J. R. Lakowicz, H. Szmacinski, K. Nowaczyk, K. W. Berndt, and M. Johnson, "Fluorescence lifetime imaging," *Analytical Biochemistry*, vol. 202, no. 2, pp. 316-330, 1992.

[23] Becker W. (2010) The bh TCSPC Handbook.

[24] W. Becker et al., "Fluorescence Lifetime Imaging by Time-Correlated Single-Photon Counting," *Microscopy Research and Technique*, vol. 63, no. 1, pp. 58-66, 2004.

[25] W. Becker, A. Bergmann, G. L. Biscott, and A. Rueck, "Advanced time-correlated single photon counting technique for spectroscopy and imaging in biomedical systems," in *SPIE Proceedings*, 2004.

[26] C-W. Chang, D. Sud, and M-A. Mycek, "Fluorescence Lifetime Imaging Microscopy," in *Digital Microscopy*.: Academic Press, 2007, pp. 495 - 524.

[27] Hamamatsu, "MCP-PMT," in *PMT Handbook*., 2007, pp. 182-208.

[28] G. W. Fraser, "X- and γ-ray imaging using microchannel plates," *Nuclear Instruments and Methods in Physics Research*, vol. 221, no. 1, pp. 115-130, 1984.

[29] J. S. Lapington, J. R. Howorth, and J. S. Milnes, "A reconfigurable image tube using an external electronic image readout.," in *SPIE 5881, Infrared and Photoelectronic Imagers and Detector Devices*, San Diego, CA, 2005, pp. 588109-588109-10.

[30] P. Buzhan et al., "An Advanced Study of Silicon Photomultiplier," *ICFA Instrumentation Bulletin*, vol. 23, 2001.

[31] P. Buzhan et al., "Silicon photomultiplier and its possible applications," *Nuclear Instruments & Methods In Physics Research*, vol. 504, pp. 48-52, 2003.

[32] L-Q. Li and L. M. Davis, "Singple photon avalanche diode for single molecule detection," *Review of Scientific Instruments*, vol. 64, no. 6, pp. 1524-1529, June 1993.

[33] Q. Yuan, B. Zhang, J. Wu, and M. E. Zaghloul, "A high resolution time-to-digital converter on FPGA for Time-Correlated Single Photon Counting," in *IEEE 55th International Midwest Symposium on Circuits and Systems (MWSCAS)*, Boise, 2012, pp. 900-903.

[34] A. V. Agronskaia, L. Tertoolen, and H. C. Gerritsen, "Fast fluorescence lifetime imaging of calcium in living cells," *Journal of Biomedical Optics*, vol. 9, no. 6, pp. 1230-1237, 2004.

[35] X. Michalet et al., "Photon-Counting H33D Detector for Biological Fluorescence," *Nuclear Instruments and Methods in Physics Research Section A*, vol. 567, no. 1, pp. 133-136, 2006.

[36] M. Eibl et al., "Single pulse two photon fluorescence lifetime imaging (SP-FLIM) with MHz pixel rate," *Biomedical Optics Express*, vol. 8, no. 7, pp. 3132-3142, Jul 2017.

[37] P. Tinnefeld, V. Buschmann, D-P. Herten, K-T. Han, and M. Sauer, "Confocal Fluorescence Lifetime Imaging Microscopy (FLIM) at the Single Molecule Level," *Single Molecules*, vol. 1, no. 3, pp. 215-223, September 2000.

[38] Z. Li et al., "A Time-Resolved CMOS Image Sensor With Draining-Only Modulation Pixels for Fluorescence Lifetime Imaging," *IEEE Transactions on Electronic Devices*, vol. 59, no. 10, pp. 2715-2722, October 2012.

[39] S. David, M. Daniel, P. Lucio, and G. Lorenzo, "Single-Photon Avalanche Diode CMOS Sensor for Time-Resolved Fluorescence Measurements," *IEEE Sensors Journal*, vol. 9, no. 9, pp. 1084-1090, September 2009.

[40] T. M. Conneely, J. S. Lapington, and J. Milnes, "Detector and electronics R&D for picosecond resolution," *Nuclear Instruments and Methods in*

Physics Research Section A: Accelerators, Spectrometers, Detectors and Associated Equipment, vol. 639, no. 1, pp. 151-154, May 2011.

[41] O. Jagutzki, V. Dangendorf, R. Lauck, A. Czasch, and J. Milnes, "A position- and time-sensitive photon-counting detector with delay-line read-out," in *Proceedings of SPIE*, Prague, 2007.

[42] O Siegmund, J Vallerga, P Jelinsky, X Michalet, and S Weiss, "Cross delay line detectors for high time resolution astronomical polarimetry and biological fluorescence imaging," *Nuclear Science Symposium Conference Record*, vol. 1, pp. 448-452, 2005.

[43] J. Jenkins, S. M. Borisov, D. B. Papkovsky, and R. I. Dmitriev, "Sulforhodamine Nanothermometer for Multiparametric Fluorescence Lifetime Imaging Microscopy," *Analytical Chemistry*, vol. 88, no. 21, pp. 10566-10572, October 2016.

[44] S. Das and P. Purkayastha, "A Fluorescence Lifetime Imaging Microscopy Supported Investigation on Temperature-Dependent Penetration of Dopamine in a 1,2-Ditetradecanoyl-sn-glycero-3-phospho-(1'-rac-glycerol) Lipid Bilayer," *Langmuir*, vol. 33, no. 29, pp. 7281-7287, June 2017.

[45] T. Robinson et al., "Analysis of DNA Binding and Nucleotide Flipping Kinetrics Using Two-Color Two-Photon Fluorescence Lifetime Imaging Microscopy," *Analytical Chemistry*, vol. 86, no. 21, pp. 10732-10740, September 2014.

[46] T. French et al., "Two-photon fluorescence lifetime imaging microscopy ofmacrophage-mediated antigen processing," *Journal of Microscopy*, vol. 185, no. 3, pp. 339-353, April 1996.

[47] S. P. Poland et al., "A high speed multifocal multiphoton fluorescence lifetime imaging microscope for live-cell FRET imaging," *Biomedical Optics Express*, vol. 6, no. 2, pp. 277-296, February 2015.

[48] J. Requejo-Isidro et al., "High-speed wide-field time-gated endoscopic fluorescence-lifetime imaging," *Optics Letters*, vol. 29, no. 19, pp. 2249-2251, October 2004.

[49] D-U. Li et al., "Real-time fluorescence lifetime imaging system with a 32 × 32 0.13μm CMOS low dark-count single-photon avalanche diode array," *Optics Express*, vol. 18, no. 10, pp. 10257-10269, March 2010.

[50] O. H. W. Siegmund et al., "Delay-line detectors for the UVCS and SUMER instruments on the SOHO Satellite," in *SPIE Proceedings*, San Diego, 1994.

[51] H. Chen and E. Gratton, "A practical implementation of multifrequency widefield frequency-domain fluorescence lifetime imaging microscopy," *Microscopy Research and Technique*, vol. 76, no. 3, pp. 282-289, 2013.

[52] Image Engineering. (2013, June) Image Engineering | camera test equipment made in Germany. [Online]. http://image-engineering.de/index.php?option=com_content&view=article&id=483

[53] O.H.W. Siegmund, A. Tremsin, J.V. Vallerga, and J. Hull, "Cross Strip Anode Imaging Readouts for Microchannel Plate Detectors," in *Nuclear Science Symposium Conference Record*, Lyon, 2000, pp. 7/71-7/75.

[54] G. D. Boreman, *Modulation Transfer Function in Optical and Electro-Optical Systems*. Washington, United States of America: SPIE, 2001.

[55] R. A. Coyler et al., "Phasor imaging with a widefield photon-counting detector," *Journal of Biomedical Optics*, vol. 17, no. 1, pp. 016008-1 - 016008-12, 2012.

[56] M. Lampton and F. Paresce, "The Ranicon: A resistive anode image converter," *Review of Scientific Instruments*, vol. 45, no. 9, pp. 1098-1105, September 1974.

[57] T. Ohnuki, X. Michalet, A. Tripathi, S. Weiss, and K. Arisaka, "Development of an ultrafast single photon counting imager for single molecule imaging," in *Proc. SPIE 6092, Ultrasensitive and Single-Molecule Detection Technologies*, San Jose, CA, 2006, pp. 60920P-1 - 60920P-9.

[58] P. Downie, D. Litchfield, R. Parsons, D. J. Reynolds, and I. Powis, "High-resolution position-sensing resistive anode microchannel plate detector systems suitable for megahertz count-rates," *Measurement Science and Technology*, vol. 4, no. 11, pp. 1293-1296, November 1993.

[59] J. S. Milnes, M. Page, M. Ingle, J. S. Lapington, and J. Howorth, "Improved electronic readout system for an imaging photon detector," *Nuclear Instruments and Methods in Physics Research Section A: Accelerators, Spectrometers, Detectors and Associated Equipment*, vol. 513, no. 1-2, pp. 163-166, November 2003.

[60] C. Martin, P. Jelinsky, M. Lampton, R.F. Malina, and H.O. Anger, "Wedge-and-strip anodes for centroid-finding position-sensitive photon and particle detectors," *Review of Scientific Instruments*, vol. 52, no. 7, pp. 1067 - 1074, July 1981.

[61] Johann Wolfgang Geothe-Universität Frankfurt. (2013, June) Atomic Physics: Experimental Atomic Physics at the Geothe-Universität Frankfurt. [Online]. http://www.atom.uni-frankfurt.de/research/coltrims/mcp/

[62] A. Smith, R. Kessel, J. S. Lapington, and D. M. Walton, "Modulation effects in wedge and strip anodes," *Review of Scientific Instruments*, vol. 60, no. 11, pp. 3509-3518, July 1989.

[63] A. Czasch et al., "Position and time sensitive photon counting detector with image charge delay-line readout," in *SPIE Proceedings Advanced Photon Counting Techniques II*, Boston, MA, 2007.

[64] O. H W Siegmund, A.S. Tremsin, and J.V. Vallerga, "High performance cross-strip detector technologies for space astrophysics," in *Nuclear Science Symposium Conference Record*, Honolulu, 2007, pp. 2246 - 2251.

[65] L.C. Stonehill et al., "Cross-strip anodes for high-rate single-photon imaging," in *Nuclear Science Symposium Conference Record (NSS/MIC)*, Orlando FL, 2009, pp. 1417-1421.

[66] S. Diebold et al., "UV MCP Detectors for WSO-UV: Cross Strip Anode and Readout Electronics," *IEEE Transactions on Nuclear Science*, vol. 60, no. 2, pp. 918-922, April 2013.

[67] A. S. Tremsin, O. H. W. Siegmund, J. V. Vallerga, J. S. Hull, and R. Abiad, "Cross-strip readouts for photon counting detectors with high spatial and temporal resolution," *IEEE TRANSACTIONS ON NUCLEAR SCIENCE*, vol. 51, no. 4, pp. 1707-1711, August 2004.

[68] O. H. W. Siegmund et al., "Cross strip microchannel plate imaging photon counters with high time resolution," in *Proc. SPIE 7681, Advanced Photon Counting Techniques IV*, Orlando, 2010, pp. 768109-1 - 768109-11.

[69] J. S. Lapington, B. Sanderson, L.B.C. Worth, and J.A. Tandy, "Imaging achievements with the Vernier readout," *Nuclear Instruments and Methods in Physics Research Section A: Accelerators, Spectrometers, Detectors and Associated Equipment*, vol. 447, no. 1-3, pp. 250-255, January 2002.

[70] J. S. Lapington et al., "A multi-channel high time resolution detector for high content imaging," *Nuclear Instruments and Methods in Physics Research A*, vol. 610, no. 1, pp. 123-127, October 2009.

[71] J.S. Lapington, T.J.R. Ashton, D. Ross, and T. Conneely, "Progress towards a 256 channel multi-anode microchannel plate photomultiplier system with picosecond timing," *Nuclear Inst. and Methods in Physics Research, A*, vol. 695, no. 1, pp. 78-82, December 2011.

[72] M. Lampton and R.F. Malina, "Quadrant anode image sensor," *Review of Scientific Instruments*, vol. 47, no. 11, pp. 1360-1362, November 1976.

[73] S. Stepanov, S. Bakhlanov, E. Drobchenko, H-J. Eckert, and K. Kemnitz, "Widefield TSCSPC-systems with large-area-detectors: application in simultaneous multi-channel-FLIM," in *Proc. SPIE 7376, Laser Applications in Life Sciences*, Oulu, 2010, pp. 1-20.

[74] Z. Petrášek, H-J. Eckert, and K. Kemnitz, "Wide-field photon counting fluorescence lifetime imaging microscopy: application to photosynthesizing systems," *Photosynthesis Research*, vol. 102, no. 2-3, pp. 157-168, November 2009.

[75] V. Emiliani et al., "Low-intensity two-dimensional imaging of fluorescence lifetimes in living cells," *Applied Physics Letters*, vol. 83, no. 12, pp. 2471-2473, September 2003.

[76] F. Anghinolfi et al., "NINO: an ultra-fast and low-power front-end amplifier/discriminator ASIC designed for the multigap resistive plate chamber," *Nuclear Instruments and Methods in Physics Research Section A: Accelerators, Spectrometers, Detectors and Associated Equipment*, vol. 533, no. 1-2, pp. 183-187, November 2004.

[77] J. Christiansen, *HPTDC Manual*, 22nd ed.: CERN/EP - MIC, 2004.

[78] T. M. Conneely, "Development of a 25 picosecond resolution imaging detector," University of Leicester, Leicester, 2010.

[79] J. L. Wiza, "Microchannel Plate Detectors," *Nuclear Instruments and Methods*, vol. 162, pp. 587-601, Match 1979.

[80] M. Cardinali et al., "Fast Frontend Electronics for high luminosity particle detectors," *physics.ins-det*, no. arXiv:1502.04937, 2015.

[81] I. T. Jolliffe, *Principal Component Analysis*, 2nd ed.: Springer, 2002.

[82] P. Birch et al., "A wide field fluorescence lifetime imaging system using a light sheet microscope," in *Proceedings of SPIE 2016 on Biophotonics: Photonic Solutions for Better Health Care*, Brussels, 2016.

[83] R. Y. Tsein, "New Calcium Indicators and Buffers with High Selectivity against Magnesium and Protons: Design, Synthesis, and Properties of Prototype Structures," *Journal of Biochemistry*, vol. 19, pp. 2396-2404, 1980.

[84] K. Sagolla, H-G. Löhmannsröben, and C. Hille, "Analytical and Bioanalytical Chemistry," *Time-resolved fluorescence microscopy for quantitative Ca2+ imaging in living cells*, vol. 405, no. 26, pp. 8525–8537, 2013.

[85] R. M. Paredes, J. C. Etzler, L. T. Watts, W. Zheng, and J. D. Lechleiter, "Chemical calcium indicators," *Methods*, vol. 46, no. 3, pp. 143-151, 2008.

[86] Photek Limited. (2010, August) DataSheet: Photomultipliers and Photodiodes. [Online]. http://www.photek.com/pdf/datasheets/detectors/DS006_Photomultipliers.pdf

[87] S. Pelet , M. J. R. Previte, L. H. Laiho, and P. T. C. So, "A Fast Global Fitting Algorithm for Fluorescence Lifetime Imaging Microscopy Based on Image Segmentation," *Biophysical Journal*, vol. 87, no. 4, pp. 2801-2817, October 2004.

[88] M. A. Digman, V. R. Caiolfa, M. Zamai, and E. Gratton, "The Phasor Approach to Fluorescence Lifetime Imaging Analysis," *Biophysical Journal: Biophysical Letters*, pp. L14 - L16, 2007.

[89] B. T. Bajar, E. S. Wang, S. Zhang, M. Z. Lin, and J. Chu, "A Guide to Fluorescent Protein FRET Pairs," *Sensors (Basel)*, vol. 16, no. 9, pp. 1488-1512, September 2016.

[90] W. Zeng et al., "Resonance Energy Transfer between Green Fluorescent Protein Variants: Complexities Revealed with Myosin Fusion Proteins," *Biochemistry*, vol. 45, no. 35, pp. 10482–10491, August 2006.

[91] J.S. Lapington, A.A. Breeveld, M.L. Edgar, and M.W. Trow, "A novel imaging readout with improved speed and resolution," *Nuclear Instruments and Methods in Physics Research Section A: Accelerators, Spectrometers, Detectors and Associated Equipment*, vol. 310, no. 1-2, pp. 299-304, December 1991.

[92] S. R. P. Pavani et al., "Three-dimensional, single-molecule fluorescence imaging beyond the diffraction limit by using a double-helix point spread function," *Proceedings of the National Academy of Sciences*, vol. 106, no. 9, pp. 2995-2999, 2009.

[93] T. Ha et al., "Probing the interaction between two single molecules: fluorescence resonance energy transfer between a single donor and a single acceptor.," *PNAS*, vol. 93, no. 13, pp. 6264–6268, 1996.

[94] F. Fereidouni, A. Esposito, G. A. Blab, and H. C. Gerritsen, "A modified phasor approach for analyzing time-gated fluorescence lifetime images," *Journal of Microscopy*, vol. 244, no. 3, pp. 248-258, 2011.

[95] D. S. Elson et al., "Real-time time-domain fluorescence lifetime imaging including single-shot acquisition with a segmented optical image intensifier," *New Journal of Physics*, vol. 6, pp. 1-13, 2004.

[96] D. W. Piston and G-J. Kremers, "Fluorescent protein FRET: the good, the bad and the ugly," *TRENDS in Biochemical Sciences*, vol. 32, no. 9, pp. 407-414, 2007.

[97] H. Yang, B. Zhao, Q. Yan, Y. Lui, and H. Hu, "Decoding algorithms of single photon counting imager based on two-dimensional Vernier anodes," *Science China Physics, Mechanics and Astronomy*, vol. 54, no. 11, pp. 1943-1947, November 2011.

[98] Q. Yan et al., "Two-dimensional photon counting imaging detector based on a Vernier position sensitive anode readout," *Chinese Physics C*, vol. 35, no. 4, pp. 368-373, April 2011.

[99] F. S. Wouters and A. Esposito, "Quantitative analysis of fluorescence lifetime imaging made easy," *HFSP Journal*, vol. 2, no. 1, pp. 7-11, 2008.